UNIVERSITY OF CALIFORNIA SAN DIEGO

Magnetization dynamics and spin-phonon coupling in $MnBi_2Te_4$

A dissertation submitted in partial satisfaction of the
requirements for the degree
Doctor of Philosophy

in

Physics

by

Maxwell Poore

Committee in charge:

Professor Richard Averitt, Chair
Professor Eric Fullerton
Professor John McGreevy
Professor Oleg Shpyrko
Professor Wei Xiong

2024

The dissertation of Maxwell Poore is approved, and it is acceptable in quality and form for publication on microfilm and electronically.

University of California San Diego

2024

DEDICATION

To my family.

EPIGRAPH

This is high-school algebra

—Hans Paar

TABLE OF CONTENTS

LIST OF FIGURES

LIST OF TABLES

ACKNOWLEDGEMENTS

Coming in to grad school I was nervous and constantly doubting myself when it came to classes, TAing, and research. I felt dread whenever I thought about actually writing and defending my thesis. However, the people in my life, and the ones I met through this process have made these past 6 years better than I could have imagined. First and foremost I'd like to thank my advisor, Richard Averitt. I first met Rick as a sophomore in undergrad when he was teaching optics, and I distinctly remember his office hours where he would simply and clearly explain things which seemed out of reach only minutes prior. He was always approachable and his genuine love for physics made me want to join his group. As an advisor he gave me the autonomy to do what I wanted and the guidance to make sure I knew how to do it. Most of all I am thankful to Rick for showing me how to go about research. Now more than ever it's common for researchers to stretch the truth of their data and to make claims that are perhaps a reach at times. But Rick is always focused on what the data is telling us and his old adage of "the data's the data" are words to live by. It's been a privilege to have worked in the Averitt lab.

I owe a large amount of gratitude to the people who make up the Averitt lab. Thank you to the older grad students: Kevin, Dylan, Gufeng, and Jacob for helping me when I was just a bumbling first year and for showing me what a productive senior grad student looks like. A special thanks goes out to Peter Kissin, who taught me most of what I know when it comes to hands on optics skills and taking data. I've been lucky to share my time in lab with Kelson, Mustafa, Yuan, and Varun who on top of being skilled physicists are excellent lunch buddies. My experience in grad school would have not been half as pleasant without Peter Kim. The wealth of laboratory and physics knowledge you imparted on me was invaluable, but it is your friendship I most treasure.

Physics to me is a team sport, and is practiced best in a group where you can think freely, try new ideas out, and learn from each other. I'm extremely appreciative

of my first year cohort, and all of the long nights spent doing stat mech homework until 11:59 and cramming for E&M exams that we knew were going to crush us. My first year experience was one I'll hold dear forever. From undergrad I want to thank Tanvi, Wan Jin, Noah, and Alex for their friendship, support, and all that they taught me.

Outside of UCSD many collaborators have been instrumental to my research and growth as a physicist. Hari, Vlad, and Venkat at Penn state (Hari is now a postdoc at Harvard) came to us four years ago looking to do a 'quick' measurement on MBT, which turned out to be a years long data taking campaign which has spawned multiple paper. In particular collaborating with Hari was an amazing experience, and so much was learned and achieved on this project I feel very lucky to have been a part of it. I'm indebted to our growers Zhiqiang Mao and Seng Huat Lee at Penn State, for supplying the samples of MBT without which none of this work would be possible. I'm grateful to Eric Fullerton, whose conversation and discussion on my spin precession work was enlightening. To the theorists, Greg, Martin, and Swati, thanks for having the patience to explain things to an experimentalist like myself, and for all their work on the spin precession project. I'd like to give a special shoutout to Swati, for the countless zoom meetings we've had over the years and all your help furthering my understanding of the data.

What makes the UCSD Physics department so great are the professors, and I've been lucky enough to have learned from the best of them these past 10 years. Thank you to Hans Paar, Jorge Hirsch, Dan Dubin, Sunil Sinha, Jeremy Palacci, Michael Fogler, Tarun Grover, Nigel Goldenfeld, Yi-Zhuang You, David Kleinfeld, Henry Abarbanel, Leonid Butov, John McGreevy, and Tom Murphy.

A special thank you to my girlfriend Kyara, whose constant love, support, and humor made me smile on even the roughest of days. To my grandfather Frank Murgolo, thank you for always believing in me, I miss you dearly. Finally, thanks to my family, Marie, Michael, and Maddie. I wouldn't be where I am today without

your unconditional love and support.

Chapter 4, in full, is a reprint of the material as it appears in Nature Communications 2022. Hari Padmanabhan, Maxwell Poore, Peter K. Kim, Nathan Z. Koocher, Vladimir A. Stoica, Danilo Puggioni, Huaiyu (Hugo) Wang, Xiaozhe Shen, Alexander H. Reid, Mingqiang Gu, Maxwell Wetherington, Seng Huat Lee, Richard D. Schaller, Zhiqiang Mao, Aaron M. Lindenberg, Xijie Wang, James M. Rondinelli, Richard D. Averitt, and Venkatraman Gopalan. The dissertation author shared the role of primary investigator and author with Hari Padmanabhan and Peter K. Kim.

Chapter 5, in part, is currently being prepared for submission for publication. Maxwell Poore, Swati Chaudhary, Peter K. Kim, Martin Rodriguez-Vega, Hari Padmanabhan, Seng Huat Lee, Zhiqiang Mao, Venkatraman Gopalan, Gregory A Fiete, and Richard D. Averitt. The dissertation author was the primary investigator and author of this material.

VITA

2018	B. S. in Physics, University of California San Diego
2018-2024	Graduate Teaching Assistant, University of California San Diego
2024	Ph. D. in Physics, University of California San Diego

PUBLICATIONS

Maxwell Poore, Hari Padmanabhan, Peter K. Kim, Nathan Z. Koocher, Vladimir A. Stoica, Danilo Puggioni, Huaiyu (Hugo) Wang, Xiaozhe Shen, Alexander H. Reid, Mingqiang Gu, Maxwell Wetherington, Seng Huat Lee, Richard D. Schaller, Zhiqiang Mao, Aaron M. Lindenberg, Xijie Wang, James M. Rondinelli, Richard D. Averitt, and Venkatraman Gopalan. *Interlayer magnetophononic coupling in $MnBi_2Te_4$.* Nature Communications, 13(1) (2022).

Maxwell Poore, Swati Chaudhary, Peter K. Kim, Martin Rodriguez-Vega, Hari Padmanabhan, Seng Huat Lee, Zhiqiang Mao, Venkatraman Gopalan, Gregory A Fiete, and Richard D. Averitt. *Spin precession and magnetization dynamics in bulk $MnBi_2Te_4$*, (in preparation)

Hari Padmanabhan, Vladimir A. Stoica, Peter K. Kim, **Maxwell Poore**, Tiannan Yang, Xiaozhe Shen, Alexander H. Reid, Ming-Fu Lin, Suji Park, Jie Yang, Huaiyu Wang, Nathan Z. Koocher, Danilo Puggioni, Alexandru B. Georgescu, Lujin Min, Seng Huat Lee, Zhiqiang Mao, James M. Rondinelli, Aaron M. Lindenberg, Long-Qing Chen, Xijie Wang, Richard D. Averitt, John W. Freeland, and Venkatraman Gopalan. *Large exchange coupling between localized spins and topological bands in $MnBi_2Te_4$.* Advanced Materials, 34(49) (2022).

Dylan Lovinger, Eli Zoghlin, Peter Kissin, Gihyeon Ahn, Kaveh Ahadi, Peter Kim, **Maxwell Poore**, Susanne Stemmer, Soonjae Moon, Stephen D. Wilson, and Richard D. Averitt. *Magnetoelastic coupling to coherent acoustic phonon modes in the ferrimagnetic insulator $GdTiO_3$.* Physical Review B **102**, 085138 (2020).

Peter K. Kim, Alejandro Ruiz, Peter Kissin, **Maxwell Poore**, Mayia Vranas, Ananya Rai, James Analytis, Alex Frañó, and Richard D. Averitt. *Quasiparticle dynamics and tracking magnetism in β-Li_2IrO_3*, (in preparation)

ABSTRACT OF THE DISSERTATION

Magnetization dynamics and spin-phonon coupling in $MnBi_2Te_4$

by

Maxwell Poore
Doctor of Philosophy in Physics

University of California San Diego 2024

Professor Richard Averitt, Chair

The field of topological materials offers an intriguing breakaway from the typical Landau symmetry breaking paradigm of phase transitions. In topologically nontrivial materials, inverted band structure leads to surface states which are topologically protected in the presence of disorder. The interplay between topology and the time-reversal symmetry breaking of magnetism yields exotic physics such as the quantum anomalous Hall effect and the axionic insulator state. Concurrent with the advances in topological materials is the field of 2D magnets and Van der Waals materials which offer physicists the ability to study magnetism in low dimensions with the added benefit of easy exfoliation to create even and odd layered samples and hetero-structures on demand. Pumping these materials with pulsed lasers allows for the direct excitation of a nonequilibrium population of hot electrons, and probing with light is an excellent tool to observe how the charge, lattice, and spin degrees

of freedom interact with each other. In this work we will investigate magnetization dynamics and spin-phonon coupling in bulk $MnBi_2Te_4$, the first intrinsic magnetic topological insulator.

Chapter 1

Introduction

An important lesson physicists learn early on in their studies is that nothing is perfect: the real world is full of air resistance, joule heating, friction, and even non-spherical cows. Later on we learn of exceptions to the rule; superconductivity and currents that will outlast humanity, superfluid Helium with zero viscosity, the quantum Hall effect displaying topologically protected edge states and exact quantization of the Hall conductance ($\frac{e^2}{h}$). These "perfect" phenomena naturally lead to an incredible amount of research both theoretically and experimentally with the aims of developing a fundamental understanding and to leverage these exotic states to further technology and industry. But beyond that point these glimpses of perfection, these nuggets of emergence and elegance in an otherwise chaotic world warrant a thorough investigation purely for the reason that they are interesting.

Topological insulators offer a novel and exciting class of materials whose properties are tied to nontrivial band structure and the emergence of edge and surface states which exhibit quantized transport and topological protection against defects. 2D magnets and Van der Waals magnets offer physicists a look at low dimensional magnetism and magnetic excitations. In $MnBi_2Te_4$ topological nontrivial band structure is combined with intrinsic magnetism in a Van der Waals crystal, producing the

first intrinsic magnetic topological insulator.

Magnetic topological insulators host an array of exotic and exciting transport phenomena such as the quantum anomalous Hall effect and Axionic insulator state. The magnetism in these materials offer a tuning knob with which we can change the symmetries in these systems, thereby altering the topological states. Light has long been used as a powerful probe of both the equilibrium and non-equilibrium properties in materials, but most exciting is the prospect of controlling macroscopic material properties with light. Finding pathways to precisely affect the magnetic state in magnetic topological insulators on ultrafast timescales will lead to the ability to selectively control and study topological phase transitions in the ultrafast regime.

Quantum materials are at the forefront of condensed matter research. The interplay between the charge, spin, lattice, and orbital degrees of freedom in these systems frequently yields rich and exciting phenomena. Quantum materials are notoriously hard to define. The Bohr-Van Leeuwen theorem proves magnetism cannot be explained classically and therefore must arise from quantum effects, band structure is predicated on an electron wave-function in a periodic potential, it seems any material is a 'quantum' material. What lies at the heart of quantum materials is the relationship between quantum factors in a material. How the charge, spin, orbital, and lattice degrees of freedom interact and connect with each other in these systems is the million dollar question. It's not simply that magnetism and band structure have quantum origins, it's the fact that the magnetism and its related symmetries influence the band structure of the surface states in MBT which makes it a promising quantum material to investigate. This work will focus on optical pathways as a means to dynamically affect and control magnetism in MBT. Magnetic topological insulators posses an intimate relation between the spin degree of freedom and the topological edge states that make them an attractive system to research.

This dissertation is organized in the following way: chapter 2 establishes the background to a lot of the physics used in the following chapters, in particular optics

and magneto-optics while also providing some background on the material studied, $MnBi_2Te_4$. Chapter 3 focuses on experimental techniques, introducing femtosecond pulsed lasers, optical parametric amplifiers, and the experimental layout and detection schemes used to collect the data presented in this work. Chapter 4 is focused on spin-phonon coupling in $MnBi_2Te_4$, using a variety of experimental probes including time resolved reflectivity (TR-reflectivity) measurements. Chapter 5 focuses on the time resolved MOKE (TR-MOKE) data that I collected, in particular the spin precession observed in the c-AFM phase.

Chapter 2

Background

2.1 Light-matter interaction

The interaction of light and matter is central to this thesis, as well as much of the work that goes on inside the Averitt lab and around the world to characterize and control novel quantum materials. Before diving into light's complex relation to materials let's start with the simplest case: Maxwell's equations in vacuum.

$$\begin{aligned} \nabla \cdot \vec{E} &= 0 \\ \nabla \cdot \vec{H} &= 0 \\ \nabla \times \vec{E} &= -\frac{\partial \vec{H}}{\partial t} \\ \nabla \times \vec{H} &= \epsilon_0 \mu_0 \frac{\partial E}{\partial t} \end{aligned} \tag{2.1}$$

If we take the curl of the third equation on both sides we arrive at:

$$\nabla^2 \vec{E} - \epsilon_0 \mu_0 \frac{\partial^2 \vec{E}}{\partial t^2} = 0 \tag{2.2}$$

Solving this wave equation gives us expressions for the $\vec{E}$ and $\vec{H}$ fields of light in vacuum as:

$$\vec{E} = \vec{E}_0 e^{i(\vec{q}\cdot\vec{r}-\omega t)}$$
$$\vec{H} = \vec{H}_0 e^{i(\vec{q}\cdot\vec{r}-\omega t)} \tag{2.3}$$

Here we see plainly light's intrinsic wave-like nature, made up of fields orthogonal to the propagation direction $\hat{q}$ and to each other. Light oscillates with an angular frequency ω and has wavelength $\lambda = \frac{2\pi}{q}$. The speed of light in vacuum, c, is given by $c = \frac{1}{\sqrt{\epsilon_0 \mu_0}}$, where ϵ_0 and μ_0 are the vacuum permittivity and magnetic vacuum permeability, respectively. It is these values that will report information to us about a sample, since in a material $\overleftrightarrow{\epsilon}$ and $\overleftrightarrow{\mu}$ will take on a tensor form and develop a frequency dependence that will encode information about the plasma frequency, phonons, band structure, and myriad other properties. In a material there will be an electrical displacement field $\vec{D}$ and a magnetic field $\vec{H}$ given by:

$$\vec{D} = \vec{E} + 4\pi\vec{P} = \overleftrightarrow{\epsilon} \cdot \vec{E}$$
$$\vec{B} = \vec{H} + 4\pi\vec{M} = \overleftrightarrow{\mu} \cdot \vec{H} \tag{2.4}$$

These equations assume that the polarization (dipole moment/unit volume) $\vec{P}$ is linear in the electric field $\vec{P} = \overleftrightarrow{\chi_e} \cdot \vec{E}$ and that the magnetization is also linear in the magnetic field $\vec{M} = \overleftrightarrow{\chi_m} \cdot \vec{B}$. $\overleftrightarrow{\chi_e}$ and $\overleftrightarrow{\chi_m}$ are the electric and magnetic susceptibility, respectively. It is important to note that $\overleftrightarrow{\epsilon}$ is a rank two tensor, for now we will assume isotropic media with no off-diagonal terms, so that $\overleftrightarrow{\epsilon}$ is just a number, multiplied by the identity matrix. Later on we will address non-isotropic media, and explore the off-diagonal terms on the dielectric tensor and their intimate relation to magneto-optics. Another assumption is that the material is nonmagnetic, meaning that $\mu = \mu_0$, leaving the dielectric function as the sole parameter needed to explain its interaction with light. Going back to Maxwell's equations, especially Ampere's law with Maxwell's correction, we see that using Ohm's law $\vec{j} = \overleftrightarrow{\sigma} \cdot \vec{E}$ we can rewrite it to look like:

$$\vec{q} \times \vec{H} = \frac{1}{c}\frac{\partial \vec{D}}{\partial t} + \frac{4\pi}{c} j = \frac{-\omega}{c}[\overleftrightarrow{\epsilon_1} + \frac{4\pi i}{\omega}\overleftrightarrow{\sigma_1}] \cdot \vec{E} = \frac{-\omega}{c}\overleftrightarrow{\epsilon} \cdot \vec{E} \tag{2.5}$$

With the corresponding wave equation governing the electric field in a material given by [1]:

$$\nabla^2\vec{E} - \frac{\epsilon_1\mu_0}{c^2}\frac{\partial^2\vec{E}}{\partial t^2} - \frac{4\pi\sigma_1\mu_0}{c^2}\frac{\partial\vec{E}}{\partial t} = 0 \tag{2.6}$$

The subscript 1 refers to the real part of these complex response functions and the term on the end, $\overleftrightarrow{\epsilon}$, is called the complex dielectric function. The dielectric function and optical conductivity can be written as:

$$\begin{aligned} \overleftrightarrow{\epsilon}(\omega) &= 1 + \frac{4\pi i}{\omega}\overleftrightarrow{\sigma}(\omega) \\ \overleftrightarrow{\sigma}(\omega) &= (1 - \overleftrightarrow{\epsilon}(\omega))\frac{i\omega}{4\pi} \end{aligned} \tag{2.7}$$

Note that the imaginary part of $\overleftrightarrow{\epsilon}(\omega)$ looks like the real part of the conductivity, which relates electric current to the applied electric field. The dielectric function and the optical conductivity convey the same information. The real part of the optical conductivity σ_1 describes the in phase current wrought by $\vec{E}$ which is dissipative, and the real part of the dielectric function ϵ_1 describes a current which is 90° out of phase with $\vec{E}$ and is dispersive in nature [2]. I have also put in the frequency dependence of both the dielectric function and optical conductivity, and this point should be emphasized; the response functions of a material are frequency dependent, and it is precisely this frequency dependence which shows us important material properties. Now that we have seen both the dielectric function and optical conductivity it is worth mentioning that the experiments mentioned in this thesis do not directly measure either quantity. Rather, we measure the reflectivity of light over a relatively narrow frequency range on a sample to gather information about the material. How we interact with response functions may vary depending on the experimental technique used, but all data retrieved from time resolved reflectivity, time resolved MOKE, and many other different spectroscopic techniques depend on the complex dielectric function $\overleftrightarrow{\epsilon}(\omega)$.

Now let's see how the dielectric function affects electromagnetic waves as they propagate through a material. Looking at Ampere's law and Faraday's law in a material with dielectric function $\overleftrightarrow{\epsilon}(\omega)$ we get:

$$\begin{aligned} \vec{q} \times \vec{H} &= \frac{-\omega}{c}(\overleftrightarrow{\epsilon}\ \vec{E}) \\ \vec{q} \times \vec{E} &= \frac{-\omega}{c}\vec{H} \end{aligned} \tag{2.8}$$

After some algebra we arrive at a value wavenumber that looks like:

$$q = \frac{\omega}{c}\sqrt{\epsilon} \tag{2.9}$$

The value $\sqrt{\epsilon}$ is also known as the index of refraction $\sqrt{\epsilon} = \tilde{N} = n + i\kappa$. As we can see from Eq. 2.2 this complex index of refraction will change the propagation of light in a material in a few ways. Firstly from the real part of $\tilde{N}$, the wavelength will decrease by a factor of n since $q = \frac{2\pi}{\lambda} = \frac{\omega}{c}\sqrt{\epsilon} = \frac{\omega}{c}(n + i\kappa)$. Secondly the imaginary part of the index of refraction will cause the wave to decay exponentially in a material, since the expression for the E field of light in an isotropic, homogeneous material is given by $E(r, \omega) = E_0 e^{i(qr-\omega t)} = E_0 e^{i(\frac{n\omega}{c}r-\omega t)} e^{\frac{-\kappa\omega}{c}r}$. The absorption coefficient which describes this exponential decay in a material is given by $\alpha = \frac{2\kappa\omega}{c}$, where the factor of 2 comes from the fact that the intensity of light is given by E^2. Framed in another light, n will decrease the speed of light in a material by $v = \frac{c}{n}$, and (since the intensity of light is given by E^2) κ will cause attenuation of the intensity of light in a material by $e^{\frac{-2\kappa\omega}{c}r}$. Lastly the electric field will experience a π phase shift as it enters a material with a higher index of refraction. This phase shift is related to the classic example of a wave on a rope, upon encountering a wall or a rope of higher density the reflected wave will be flipped upside down.

As mentioned previously one of the main experimental techniques of this thesis is time resolved reflectivity, but before diving into time resolved experimental techniques one should understand how the static reflectivity relates to material properties and in particular the dielectric function. To do this we consider light

propagating at normal incidence from air (we can say $\tilde{N}$=1) into a material with $\tilde{N} = n + i\kappa$. By using Maxwell's equations and requiring continuity of the waves at the interface we get Fresnel equations describing the transmission and reflection of light at an interface. The amplitude reflection and transmission coefficients are:

$$\begin{aligned} r &= \frac{1-\tilde{N}}{1+\tilde{N}} \\ t &= \frac{2}{1+\tilde{N}} \end{aligned} \tag{2.10}$$

But these are the coefficients for the fields, and what we measure in the lab is the intensity from a reflected or transmitted beam on a photo-diode, and thus we must square (with the complex conjugate to ensure a purely real intensity) these values to get to a value for our physical observable:

$$\begin{aligned} R = rr^* &= \frac{1-\tilde{N}}{1+\tilde{N}} \cdot \frac{1-\tilde{N}^*}{1+\tilde{N}^*} = \frac{(n-1)^2+\kappa^2}{(n+1)^2+\kappa^2} \\ T = tt^* &= \frac{2}{1+\tilde{N}} \cdot \frac{2}{1+\tilde{N}^*} = \frac{4}{(n+1)^2+\kappa^2} \end{aligned} \tag{2.11}$$

These values, in particular R, will be an invaluable tool to describe material parameters and response.

2.2 Drude model

One of the first basic models of solids that physics students learn is the Drude model, and while it is a simplified toy model that ignores some key factors such as electron-electron interactions and band structure, it reproduces many results and is a useful tool for understanding charge transport under the effect of an applied field [3], [4]. "Why are metals shiny?" may seem like a basic question but its answer gives us a deeper understanding of what goes on microscopically inside solids. In the Drude model we assume that there are unbound electrons that behave like an ideal gas; with elastic collisions occurring with the environment and the positively

charged ions but we do not consider the electron-electron interactions or interband transitions as mentioned before. In this picture we can write the equation of motion as:

$$\frac{d}{dt} < \vec{p} >= -\vec{E}e - \frac{< \vec{p} >}{\tau} \tag{2.12}$$

where $< p >$ is the time averaged momentum, and the two terms contributing to the equation of motion are the force term from the field (-Ee) and the term which describes momentum scattering on a characteristic timescale τ, which we call the scattering time (electrons get accelerated by the external field for a time τ before they scatter, on average). If we view this equation of motion in the frequency domain we get:

$$\begin{aligned} -i\omega < \vec{p}(\omega) >= -\vec{E}e - \frac{< \vec{p}(\omega) >}{\tau} \\ < \vec{p}(\omega) >= \frac{-\vec{E}e}{-i\omega + \frac{1}{\tau}} \end{aligned} \tag{2.13}$$

Now if we want to write an expression for current density $\vec{j}$, we can take advantage of the fact that $\vec{j} = -en < \vec{v} >$, where e is charge of the charge carrier, n is the density of charge carriers, and $< \vec{v} >$ is the time averaged velocity of these charges, and since we already found the steady state momentum in this picture we can use $< \vec{v} >= \frac{<\vec{p}>}{m}$ (m being the effective mass of the charge carrier). Plugging this into the current density expression yields:

$$\vec{j}(\omega) = \frac{e^2 n\tau/m}{1 - i\omega\tau}\vec{E}(\omega) = \sigma_D(\omega)\vec{E}(\omega) \tag{2.14}$$

Here the utility of the Drude model is on display, from an extremely simple set of assumptions we recover Ohm's law and obtain an expression for frequency dependent optical conductivity:

$$\sigma_D(\omega) = \frac{e^2 n\tau/m}{1 - i\omega\tau} = \frac{\sigma_0}{1 - i\omega\tau} \tag{2.15}$$

where σ_0 is the DC conductivity. Plugging this expression into the first expression

in Eq. 2.7 we can recover an expression for the dielectric function:

$$\epsilon(\omega) = 1 - \frac{\sigma_0 4\pi}{\omega^2\tau + i\omega} = 1 - \frac{\omega_p^2}{\omega^2 + i\omega/\tau} \tag{2.16}$$

where $\omega_p^2 = \sigma_0 4\pi/\tau = \frac{4\pi n e^2}{m}$, ω_p is called the plasma frequency. Physically we can think of the plasma frequency as the "natural" frequency of the electrons in the plasma. Normal modes, or resonance frequencies are mentioned throughout this thesis and the ideas are ubiquitous not only in condensed matter, but in all areas of physics and this is no exception.

Inspecting the expression for plasma frequency, we can see that as carrier density n is increased, ω_p increases. On the other hand, if effective mass m is increased, the plasma frequency will go down. There are some simple considerations that will improve upon Eq. 2.16, firstly we have assumed response only from free carriers, but the ion cores will also provide a high frequency modification to the dielectric function (now as $\omega \to \infty$, $\epsilon \to \epsilon_\infty$ instead of 1). Secondly, under the assumption $\omega\tau >> 1$ the second term in the denominator can be left out and we are left with a simplified expression:

$$\epsilon(\omega) = \epsilon_\infty - \frac{\omega_p^2}{\omega^2} \tag{2.17}$$

At a special frequency $\omega_{sp} = \frac{\omega_p}{\sqrt{\epsilon_\infty}}$, called the screened plasma frequency, the dielectric function passes through zero. Put another way, below ω_{sp}, ϵ will always be negative. This means the complex index of refraction N will have purely imaginary components, but above this frequency N will be positive and have real components. Looking at Eq. 2.11 when N is purely imaginary the reflectance should be 1, and when N is purely real it should drop to $R = (n-1)^2/(n+1)^2$.

2.3 Nonlinear optics

As mentioned earlier the polarization of a material, or its dipole moment/unit volume can be expressed by:

$$\vec{P}(t) = \chi^{(1)}\vec{E}(t) \tag{2.18}$$

where $\chi^{(1)}$ is the linear susceptibility and $\vec{P}(t)$ and $\vec{E}(t)$ are complex valued vectors. While this describes the reaction to an electric field inside a material quite well, for large electric fields the polarization may not depend linearly on the electric field and we can expand the polarization in a power series, where the polarization as a function of time is a sum of terms increasing in the power of the electric field:

$$\vec{P}(t) = \chi^{(1)}\vec{E}(t) + \chi^{(2)}\vec{E}^2(t) + \chi^{(3)}\vec{E}^3(t) + ... \tag{2.19}$$

$\chi^{(2)}$ is referred to as the second order susceptibility and will be the main focus of this section. Importantly, due to symmetry requirements, the second order susceptibility vanishes for crystals with inversion symmetry, so the second order effects will only take place in crystals which lack inversion symmetry/ are non-centrosymmetric [5]. If we consider the case where there are two fields present $E(t) = (E_1 e^{-i\omega_1 t} + E_2 e^{-i\omega_2 t}) + cc.$ where E_1 and E_2 represent the amplitudes of the electric fields oscillating at ω_1 and ω_2, respectively. The cc. at the end of Eq.2.20 is the complex conjugate and plays the role of creating optical rectification (OR) and difference frequency generation (DFG), both of which are staples of optics labs and make possible the experiments we undertake. Calculating the second order polarization response:

$$\begin{aligned}\vec{P}^{(2)}(t) = \chi^{(2)}\vec{E}^2(t) = \chi^{(2)}(2(E_1E_1^* + E_2E_2^*) + 2E_1E_2^*e^{-i(\omega_1-\omega_2)t} + \\ E_1E_1e^{-i2\omega_1 t} + E_2E_2e^{-i2\omega_2 t} + 2E_1E_2e^{-i(\omega_1+\omega_2)t} + cc).\end{aligned} \tag{2.20}$$

The first two terms $E_1E_1^*$ and $E_2E_2^*$ describe optical rectification (OR), where the same frequency is involved in difference frequency generation $(\omega_1 - \omega_1)$ and you are left with a frequency independent D.C. electric field. In reality, due to the

bandwidth of the fields ω_1 and ω_2 this is the process which produces terahertz (THz) radiation in nonlinear crystals like $LiNbO_3$ and ZnTe. The term which has frequency dependence $(\omega_1 - \omega_2)$ describes difference frequency generation (DFG) between two non-degenerate waves, this process is the workhorse of optical parametric amplification (OPA) processes [6], [7] which will be talked about later when discussing how we generate the pump pulses for our optical pump-optical probe (OPOP) experiments. The next two terms which have twice the frequency of the components of our original field. $2\omega_1$ and $2\omega_2$ represent second harmonic generation (SHG), a type of sum frequency generation where the same frequency is involved. Like DFG this is a prolific nonlinear process which we use frequently in lab, be it for pumping BBO crystals in an OPA process or for optimizing pulse compression, SHG is another pillar of condensed matter experiment. The final term with $(\omega_1 + \omega_2)$ represents the sum frequency generation (SFG) process, where two photons at ω_1 and ω_2 are absorbed and a photon at $\omega_3 = \omega_1 + \omega_2$ is emitted [5]. The complex conjugate at the end of Eq. 2.20 shows that for every frequency component ω the is a complimentary negative frequency component $-\omega$. Nonlinear optics is a field of far reaching application and depth, for additional details refer to [5].

2.4 Magneto-Optics

At the heart of magneto-optical phenomena such as the Faraday and Kerr effect is the fact that the polarization of linearly polarized light is both rotated and made elliptical when traveling through or reflecting off of a magnetic material. This simple phenomena of magnetism affecting the polarization of light makes possible the experiments detailed later in this work and has become a valuable tool to physicists researching magnetism and magnets in non-equilibrium conditions. One way to understand this effect is that magnetism induces a circular birefringence in that material; that is, right-handed circularly polarized (RCP) and left-handed circularly

polarized (LCP) light travels through a medium at different speeds, causing a phase shift between the two differently-handed polarizations. Similarly, LCP and RCP light will be absorbed at different rates, leading to an ellipticity in the incident linearly polarized light. Just as the dielectric function is composed of dispersive and dissipative parts, so too are the magneto-optical constants we deal with. Kerr rotation refers to the dispersive part (also called circular birefringence), where LCP and RCP have different propagation speeds. Kerr ellipticity refers to the dissipative part (also referred to as circular dichroism) where LCP and RCP are absorbed at different rates. It will be shown later that the degree of rotation and ellipticity are both proportional to M_z in polar MOKE. Since linearly polarized light can be thought of as the superposition of a LCP and RCP light, this effectively causes linearly polarized light to become rotate/elliptical due to this circular birefringence/dichroism [8]–[10].

Phenomenologically we can understand this effect as coming from the Lorentz force ($\vec{F} = q(\vec{E} + \vec{v} \times \vec{B})$). For a material with spins pointing in the z direction the degeneracy of clockwise and counterclockwise electron motion in the x-y plane is broken for LHC vs. RHC light. This leads to the circular motion caused by LHC and RHC having different radii and causes different optical constants for LHC and RHC light. Another way to think of light's interaction with magnetic materials is through the lens of second quantization. In this picture the Faraday or Kerr rotation can be seen as an elastic scattering of photons off of spins which imparts a $\frac{\pi}{2}$ rotation of the polarization. Furthermore, many other magneto-optical effects can be described using the magneto-optical coupling Hamiltonian with both the radiation and the magnetic system described in the second quantization formalism. For the purpose of this thesis I will focus on the circular birefringence description, and direct the interested reader to [10] for further information on the second quantization treatment of magneto-optical processes.

For a sample with magnetization along its c-axis (in the $+\hat{z}$ direction), due

to the change in symmetry in the crystal its dielectric tensor will take the form:

$$\epsilon = \begin{pmatrix} \epsilon_{xx} & \epsilon_{xy} & 0 \\ -\epsilon_{xy} & \epsilon_{xx} & 0 \\ 0 & 0 & \epsilon_{xx} \end{pmatrix} \tag{2.21}$$

Where we have assumed an isotropic medium with magnetization along the c-axis that induces the off-diagonal terms due to breaking of time-reversal symmetry. These off diagonal terms will be proportional to the magnetization and transform anti-symmetrically with field, $\epsilon_{xy}(M_z, \omega) = -\epsilon_{xy}(-M_z, \omega) = -\epsilon_{yx}(M_z, \omega) \propto M_z$. Going back to Eq. 2.2 and plugging the dielectric tensor with the off-diagonal terms into the wave equation for light traveling in the $\hat{z}$ direction will yield a set of coupled equations:

$$\begin{aligned} (\tilde{N}^2 - \epsilon_{xx})\vec{E}_x - \epsilon_{xy}\vec{E}_y = 0 \\ (\tilde{N}^2 - \epsilon_{xx})\vec{E}_y + \epsilon_{xy}\vec{E}_x = 0 \end{aligned} \tag{2.22}$$

Solving $\tilde{N}^4 - 2\tilde{N}^2\epsilon_{xx} + (\epsilon_{xx}^2 + \epsilon_{xy}^2) = 0$ gives us two solutions for $\tilde{N}^2$:

$$\tilde{N}_\pm^2 = \epsilon_{xx} \pm i\epsilon_{xy} = (n_\pm + ik_\pm)^2 \tag{2.23}$$

Where the $\tilde{N}_+$ solution corresponds to RHC polarized light and $\tilde{N}_-$ to LHC polarized light. In the same fashion as equation 2.9 we can define reflection coefficients for RHC and LHC light:

$$\begin{aligned} r_+ &= \frac{1 - \tilde{N}_+}{1 + \tilde{N}_+} \\ r_- &= \frac{1 - \tilde{N}_-}{1 + \tilde{N}_-} \end{aligned} \tag{2.24}$$

With the goal in mind of detecting these observables in lab (namely the rotation and ellipticity of our probe beam) it is useful to define a complex Kerr angle:

$$\tilde{\Theta} = \frac{\tilde{E}_{y,R}}{\tilde{E}_{x,R}} \tag{2.25}$$

To find $\tilde{E}_{y,R}$, the reflected E field in the $\hat{y}$ direction, we will utilize reflection transfer matrices in both the x-y paradigm as well as the circularly polarized basis [11]. To start off let's look at the case of reflection off a magnetic sample with incident $\hat{x}$ polarization:

$$\begin{pmatrix} \tilde{E}_{x,R} \\ \tilde{E}_{y,R} \end{pmatrix} = \begin{pmatrix} r_{xx} & r_{xy} \\ -r_{xy} & r_{xx} \end{pmatrix} \begin{pmatrix} \tilde{E}_{x,I} \\ 0 \end{pmatrix} \tag{2.26}$$

The subscript R refers to the reflected fields and I the incident fields. Going to the circularly polarized basis to utilize Eq. 2.24, we can transform our reflection matrix by doing the following:

$$\frac{1}{2}\begin{pmatrix} 1 & -i \\ 1 & i \end{pmatrix} \begin{pmatrix} r_{xx} & r_{xy} \\ -r_{xy} & r_{xx} \end{pmatrix} \begin{pmatrix} 1 & 1 \\ i & -i \end{pmatrix} = \begin{pmatrix} r_{xx} + ir_{xy} & 0 \\ 0 & r_{xx} - ir_{xy} \end{pmatrix} = \begin{pmatrix} r_+ & 0 \\ 0 & r_- \end{pmatrix} \tag{2.27}$$

Looking at the reflection matrix equation in the circularly polarized basis for incident linearly polarized $\hat{x}$ light:

$$\begin{pmatrix} \tilde{E}_{+,R} \\ \tilde{E}_{-,R} \end{pmatrix} = \frac{1}{\sqrt{2}} \begin{pmatrix} r_+ & 0 \\ 0 & r_- \end{pmatrix} \begin{pmatrix} 1 \\ 1 \end{pmatrix} E_{x,I} = \frac{1}{\sqrt{2}} \begin{pmatrix} r_+ \\ r_- \end{pmatrix} E_{x,I} \tag{2.28}$$

Now that we have expressions for the reflected fields for RCP and LCP light let's convert back to x-y basis so we can obtain an expression for Eq. 2.25:

$$\begin{pmatrix} E_{x,R} \\ E_{y,R} \end{pmatrix} = \frac{1}{\sqrt{2}} \begin{pmatrix} 1 & 1 \\ i & -i \end{pmatrix} \begin{pmatrix} E_{+,R} \\ E_{-,R} \end{pmatrix} = \frac{E_{x,I}}{\sqrt{2}} \begin{pmatrix} r_+ + r_- \\ i(r_+ - r_-) \end{pmatrix} \tag{2.29}$$

Plugging this result into Eq. 2.25:

$$\tilde{\Theta} = \frac{i(r_+ - r_-)}{r_+ + r_-} = \frac{\tilde{N}_- - \tilde{N}_+}{1 - \tilde{N}_-\tilde{N}_+} \tag{2.30}$$

Now using the definitions for $N_\pm$ from Eq. 2.23 and operating under the assumption mentioned previously of $\epsilon_{xx} >> \epsilon_{xy}$ (ignoring terms $(\frac{\epsilon_{xy}}{\epsilon_{xx}})^2$in the binomial expansion) we arrive at:

$$\tilde{\Theta} \approx \frac{i\epsilon_{xy}}{\sqrt{\epsilon_{xx}}(1 - \epsilon_{xx})} \approx \theta + i\eta \tag{2.31}$$

where θ is the real part of the complex Kerr angle that describes the rotation of the polarized light after being reflected from a magnetic sample, and η is the imaginary part of the complex Kerr angle, and corresponds to the Kerr ellipticity.

$$\begin{aligned}\theta &= \frac{Re[\epsilon_{xy}](3nk^2 - n^3 + n) + Im[\epsilon_{xy}](3n^2k - k^3 - k)}{(n^2 + k^2)((n^2 + k^2) - 2n^2 + 2k^2 + 1)} \\ \eta &= \frac{Im[\epsilon_{xy}](3nk^2 - n^3 + n) - Re[\epsilon_{xy}](3n^2k - k^3 - k)}{(n^2 + k^2)((n^2 + k^2) - 2n^2 + 2k^2 + 1)}\end{aligned} \tag{2.32}$$

For a more complete derivation refer to [8] and [11]. Since $\epsilon_{xy} \propto M_z$, Eq. 2.31 shows that the Kerr rotation and ellipticity will be proportional to M_z.

2.5 $MnBi_2Te_4$

The story of $MnBi_2Te_4$ starts with the search for viable materials to realize the Quantum Anomalous Hall Effect (QAHE). As the field of 3D TIs were rapidly growing so was the research goal of gapping the surface states by breaking time-reversal symmetry in the QSHI to achieve the QAHE. In 2010 Rui Yu published a paper predicting that introducing transition metal magnetic dopants in 3D TI would be a viable path towards the realization of the QAHE [12]. In 2013 Cui-Zu Chang and collaborators succeeded in demonstrating the first experimental observation of the QAHE in magnetically-doped TI $Cr_{0.15}(Bi_{0.1}Sb_{0.9})_{1.85}Te_3$ [13]. Although this work demonstrated the telltale signs of QAHE (vanishing longitudinal resistance, $\rho_{xx} = 0$, and quantized hall resistance $\rho_{yx} = \frac{h}{e^2}$), the temperatures required to observe these behaviors were prohibitively low ($\sim$30 mK). Several other studies confirming the quantized hall resistivity soon followed, however they all displayed extremely low temperatures necessary to observe QAHE [14]–[17]. Progress was made as other dopants such as Vanadium were used and remnants of the QAHE state were seen at higher temperatures (5 K). Some advantages of $(Bi_{0.29}Sb_{0.71})_{1.89}V_{0.11}Te_3$ include a much higher Hall angle at zero field and higher temperatures displaying QAHE-like behavior. Despite the relatively high Curie temperature and coercive field of the

sample, extremely low temperatures (25 mK) were still needed to see full quantization of the Hall resistance and Hall angle close to 90°(α=ArcTan($\frac{\rho_{yx}(0)}{\rho_{xx}(0)}$)) [18].

Once the QAHE had been experimentally verified, the search for better candidate materials began. In particular, since magnetism in the first QAHE materials was introduced via magnetic doping, this caused relatively weak magnetism with low Curie temperatures and weak coupling between the topological surface states (TSS) and the localized spins in the material. To create a more robust QAH state, a topological insulator with intrinsic, homogeneous magnetism is needed. In 2017 Mikhail Otrokov and collaborators predicted that including a magnetic extension of an already existing TI would lead to an intrinsic magnetic TI and a robust QAHE material [19]. This amounts to intercalating MnTe, a room temperature magnetic semiconductor, into Bi_2Te_3, a well established TI [20]. Two years later in 2019 Otrokov published the first proof of an intrinsic magnetic topological insulator [21], with ARPES data showing a Dirac point gap increasing as the sample is cooled below T_N.

While being the first intrinsic magnetic topological insulator is exciting, MBT is an interesting material for other reasons aside from exotic topological states. MBT arranges into Te-Bi-Te-Mn-Te-Bi-Te septuple layers (SL), which are weakly bonded to other SL by Van der Waals (VdW) forces, to form a R$\bar{3}$m space group lattice (no. 166) with lattice parameters a=4.3 Å and c=40.9 Å [23], [24]. This means MBT is an easily exfoliated crystal and, as will be mentioned later, MBT has extremely interesting layer-dependent behavior due to its AFM order [22], [25]–[27]. The fact that it is a VdW crystal means that it is amenable to device fabrication and creating hetero-structures with the magnetic SL [24]. While time-reversal symmetry Θ, and the primitive translation symmetry along the c axis $T_{1/2}$ are both broken in the AFM phase, the combined symmetry $S = \Theta T_{1/2}$ is conserved. It is this combined symmetry which provides topological protection to surface states on AFM TIs [28]. Additionally, MBT has robust magnetism, ordering into an A-type AFM

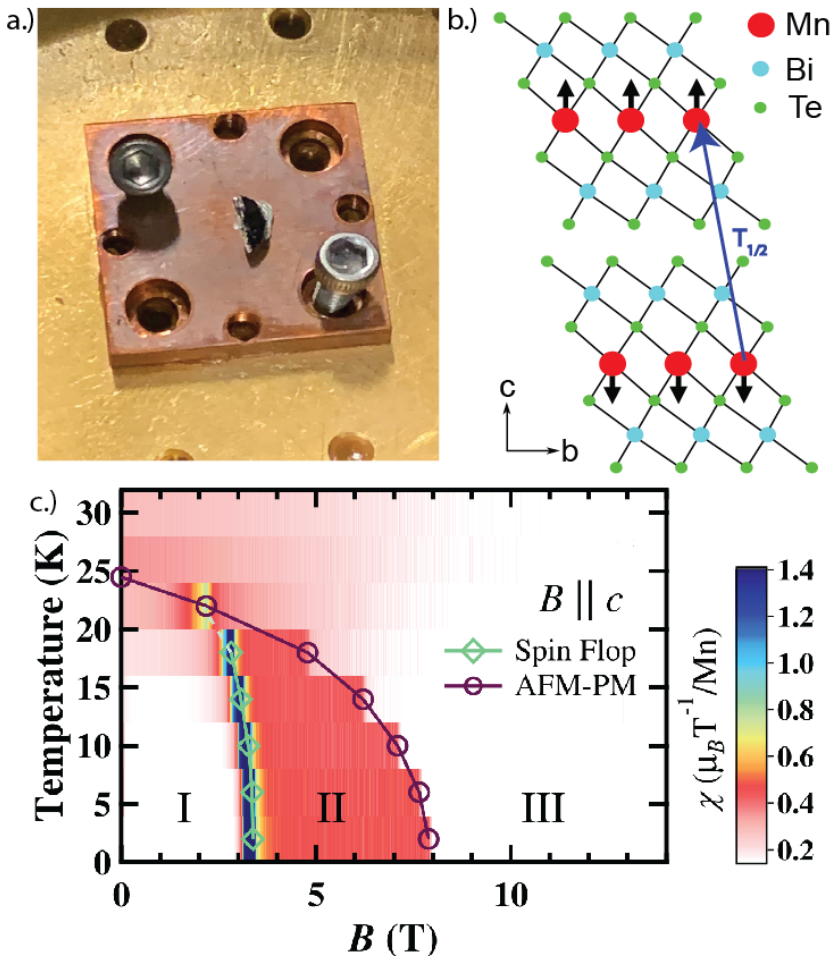

Figure 2.1: **$MnBi_2Bi_4$ crystal structure and phase diagram. a.** MBT sample used in the time-resolved experiments on the sample mount on the cold finger of the Opticool magnet. **b.** Crystal structure of MBT. **c.** Temperature-magnetic field phase diagram in MBT, from [22].

at T_N=24K, with spins aligned ferromagnetically in the a-b plane, and AFM order along the c-axis. Applying a field along the c-axis causes a spin-flop transition to occur at ∼3.7 T with full FM alignment occurring at ∼7.7 T.

There is some controversy regarding the TSS gap across the transition temperature. Although the original paper by Otrokov observed a temperature dependence of the gap across T_N, subsequent studies found either a gapless surface state,

or a small gap on the order of the energy resolution of the ARPES set up, with almost no temperature dependence [22], [29]–[35]. Most of these studies attribute the gapped Dirac cone from [21] misidentifying bulk bands, or from the high photon energies used in the ARPES measurements which saw a large Dirac Point gap. Theoretically, the explanation as to why they don't see the predicted gap opening across T_N hinged on either a reconstruction of surface magnetism which leads to a gapless dispersion [22], [29], [31]–[34] or weak coupling between the TSS and the Mn 3d states that carry the localized spin [30], [32].

On the other hand, there were also several studies following the original Otrokov work which showed TSS gaps of 85 meV [36], 90 meV [37], 25 meV [38], 45 meV [39] and 100 meV [40]. A common theme in these studies is that most were carried out using ARPES light >20 eV, while the studies which used lower energy ($\sim$7 eV) laser light for their ARPES showed no gap opening across T_N, and it has been postulated that it was because of these higher photon energies that a gap was observed due to a photon energy dependent matrix element [31]. Another issue is that the gap is seen to survive well past the transition temperature, where magnetic order should vanish causing the gap to close. This is most likely due to strong spin fluctuations in the PM state arising from the fact that the intralayer coupling is much stronger than the interlayer coupling, giving rise to FM-like spin fluctuations at temperatures far above that of AFM ordering [36]. Some clarity on these disparate results was given in a 2021 paper by Alexander Shikin and collaborators [41]. They studied 15 samples from two different growers using ARPES at 6.3 eV photon energy and found a TSS gap of 15 meV-65 meV, with half of the samples exhibiting a gap of around 30 meV. Additionally, they found that uncompensated charge on the sample surface could result in a reduction of the gap in the TSS, explaining the varied values in gap size between different studies. Despite thorough investigation from groups around the world the behavior of the TSS gap at the Dirac point in MBT is still under debate.

Despite the opening of a gap in the surface states of MBT still being investigated, transport measurements offer strong evidence of the robust topological properties in MBT. In odd layer MBT due to the AFM order there will be an uncompensated layer of spins, leading to a net magnetization in the sample. In these odd layer samples there has been verification of the QAHE, with quantized hall resistance $\rho_{xy} = \frac{h}{e^2}$ and longitudinal resistance, $\rho_{xx} = 0$ [42], [43]. In Fig. 2.2, the left panel shows transport measurements displaying clear signs of the QAHE, with the Hall resistance being quantized in units of h/e^2 and the longitudinal resistance dropping to nearly zero. In most MBT samples the Fermi level is not situated within the surface state gap, so a voltage must be applied to bring the Fermi level into the gap to allow for the exotic transport phenomena [25], [27], [44]. Doping Sb into the material or annealing at a precise temperature are alternate methods to bring the Fermi level into the gap [33], [45].

In even layered samples MBT is predicted to be an axionic insulator, since it satisfies the requirements of having the surfaces be gapped due to magnetism, making sure the Fermi level resides in the surface state gap (this can be done with applied voltage or doping), and having a thick enough sample to get rid of finite size effects [46]. In the right panel of Fig. 2.2 the C=0 axionic insulator state in 6-SL MBT is transformed into the C=1 Chern insulator state by applying a strong magnetic field, inducing ferromagnetic alignment of the spins in the sample. In [25] strict control over the axionic field was demonstrated, which switched between two AFM states causing the Hall resistivity R_{xy} to change sign. Repeatable swtiching was demonstrated by continuous ramping up and down of the gate voltage, with the AFM configurations and AHE switching 18 times within 1000 seconds. The verification of dynamic switching of these exotic states bodes well for the goal of ultrafast control of these states. Although it was on much slower timescales, the fact that these topological states are flexible and repeatable in time opens the door increasing switching speeds and perhaps utilizing light as a control knob for topological control

in MBT.

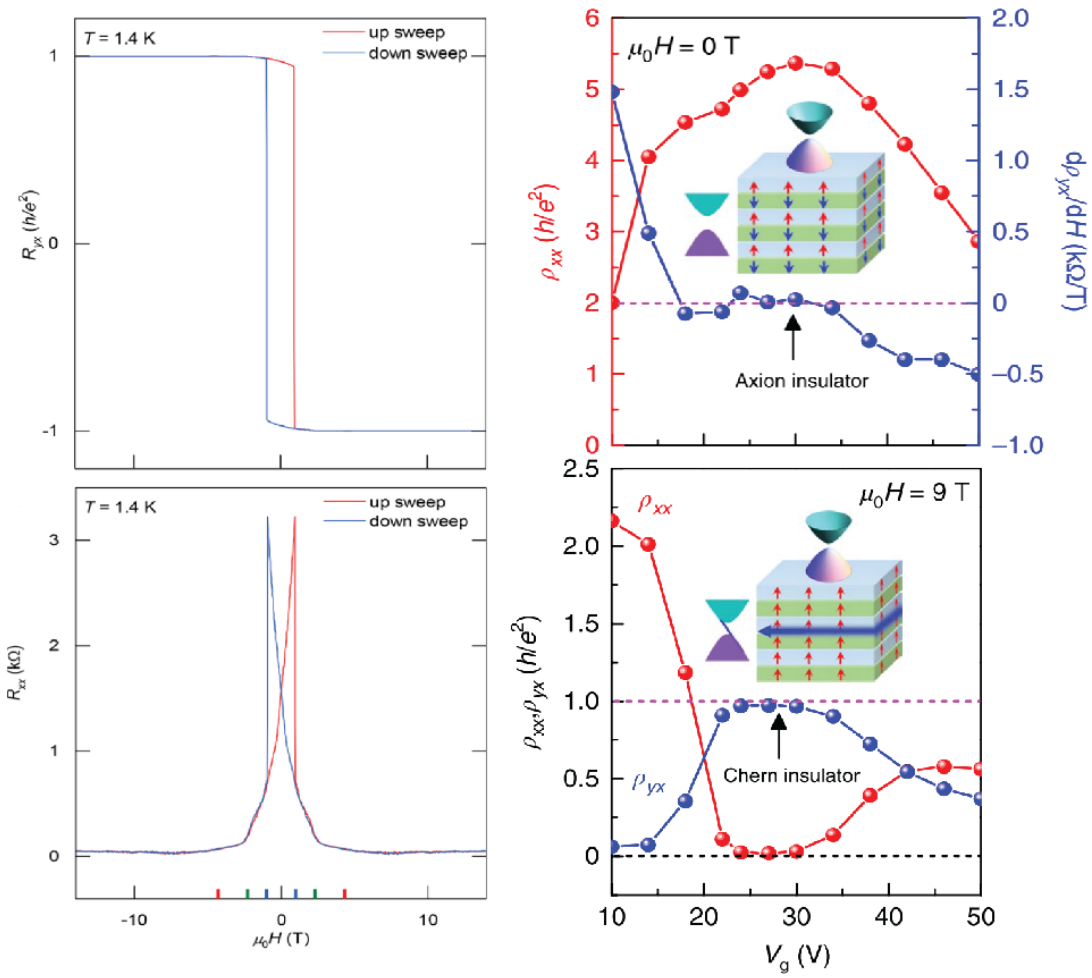

Figure 2.2: **Transport measurements showing QAHE and axionic insulator states.** Left panels: data from [42] on 5-SL samples of MBT showing quantized Hall resistance and near zero longitudinal resistance at zero field, which indicate the QAHE. Right panels: data from [27] on 6-SL samples of MBT demonstrating the C=0 to C=1 transition as the axionic insulator state is turned into a Chern insulator in the presence of a high magnetic field.

2.6 Topological Insulators

The main concept behind topological insulators is that not all insulators are equal; it is possible for a material to have a bulk band gap that is topologically nonequivalent to the vacuum (or an ordinary band insulator). This in-equivalence stems from band inversion caused by spin-orbit coupling, and much like the classic example of the topological in-equivalence between a baseball and a donut, you cannot adiabatically transform between one band-structure and the other without closing the gap. At the boundary between a topological insulator and a trivial insulator gapless surface states with Dirac-like linear dispersion occupy the bulk energy gap, as demonstrated in Fig. 2.3.d, providing a bridge between the inverted and non-inverted band structures [47]. These Dirac-like surface states, one moving to the left and the other to the right (with opposite spin) have the desirable quality of dissipationless transport due to spin-momentum locking providing no channels for back-scattering of the carriers. Additionally the Hall conductivity will be quantized, however in the above case known as the Quantum Spin Hall Insulator (QSHI) which is described in Fig. 2.3.c, there are equal amounts of left-and right-moving surface states. This results in the net charge transported being cancelled out by these opposing spin channels. The net spin however is not cancelled out, and there is a quantized spin hall conductance associated with the surface states.

In 2D topological insulators with broken time-reversal symmetry the Chern invariant is a useful number to describe the topological properties of a material. For a Bloch wavefunction $|u_m\rangle$ corresponding to a specific band m, the Berry connection or Berry potential is given by $A_m = i\langle u_m|\nabla_k|u_m\rangle$ [48]. The Berry phase is given by the line integral of this Berry connection as $\mathbf{k}$ is taken around a closed loop. The Chern invariant, which is closely related to the Berry phase, is the total Berry flux, $F_m = \nabla \times A_m$, in the Brillouin zone:

$$n_m = \frac{1}{2\pi} \int F_m d^2\mathbf{k} \tag{2.33}$$

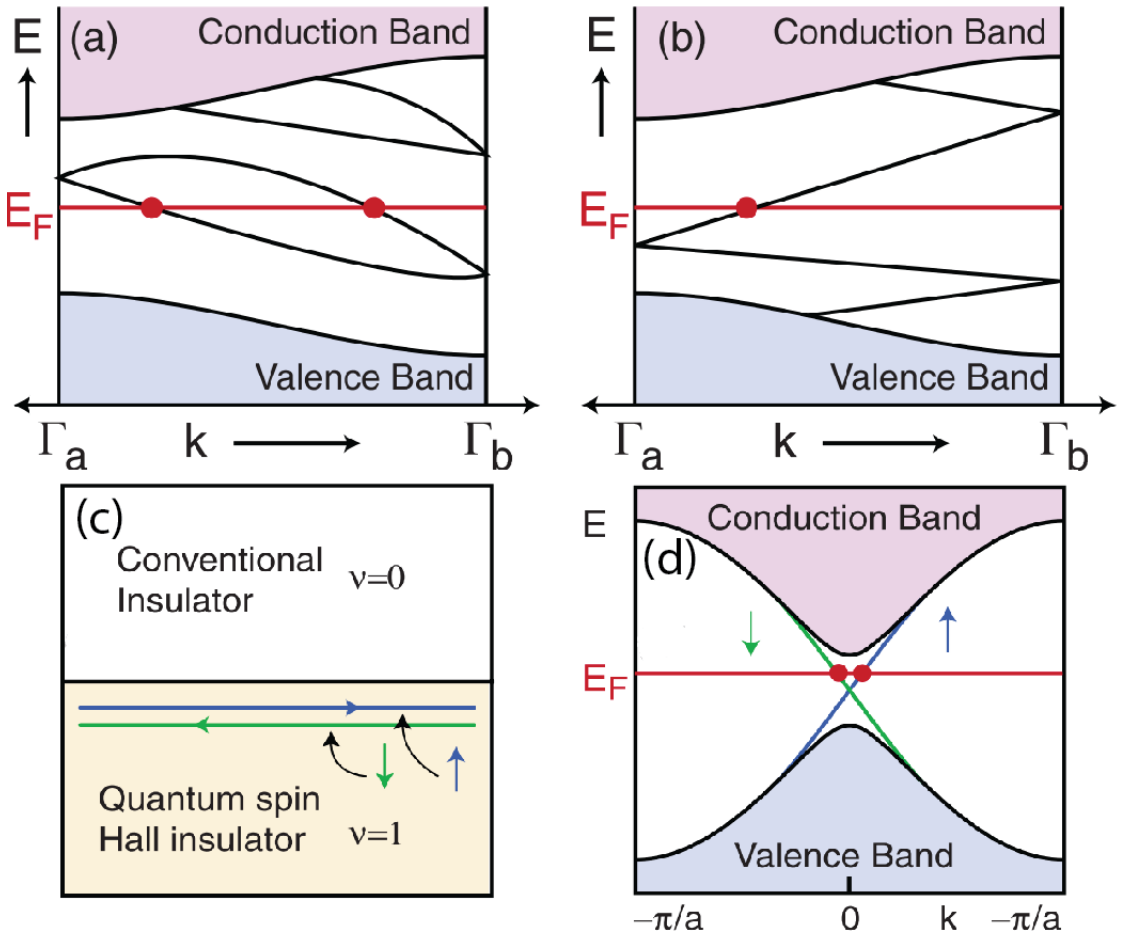

Figure 2.3: **Topological insulators and band structure.** From [47]. **a.** An example of trivial connection, where an even number of surface states cross the Fermi level between two Kramers degenerate points. **b.** A nontrivial connection of surface states across Kramers degenerate points, where an odd number of crossings occur, leading to topologically protected surface states. **c.** A real-space diagram describing the interface between a conventional insulator ($\nu = 0$) and a topologically nontrivial insulator ($\nu = 1$), spin-momentum locked edge states can be seen near the boundary. **d.** Electronic dispersion of a topological insulator, when the Fermi surface lies in the bulk gap spin-momentum locked edge states connect the valence and conduction bands.

Summing over all occupied bands gives the total Chern number: $n = \sum_m^N n_m$. Thouless, Kohmoto, Nightingale, and den Nijs, proved that the n found from taking a surface integral of the Berry flux over the Brillouin zone for all occupied bands is the

same N that shows up in the quantum Hall effect (QHE) [49], $\sigma_{xy} = N\frac{e^2}{\hbar}$.

For time-reversal invariant systems there is another type of topological classification given by the $\mathbb{Z}_2$ invariant ν, where $\nu = 0$ signifies a topologically trivial material and $\nu = 1$ corresponds to topologically non-trivial. The $\mathbb{Z}_2$ invariant is given by

$$(-1)^{\nu} = \prod_{a=1}^{4} \delta_a \tag{2.34}$$

where in general δ_a is computed using complex mathematical formulations [50], [51]. If the crystal has inversion symmetry however, δ_a can be expressed in a more straightforward way as:

$$\delta_a = \prod_{m=1}^{2N} \xi_{2m}(\Gamma_i) \tag{2.35}$$

Where $\xi_{2m}(\Gamma_i) = \pm 1$ is the parity eigenvalue of the $2m^{th}$ band at the crystal momentum Γ_i, which is special in that the eigenvalues ξ_{2m} and ξ_{2m-1} will be equal at this momentum value due to time-reversal invariance and Kramer's theorem [52].

Visually we can think about there being edge states in the bulk gap and how they connect to the time-reversal invariant Γ points in the Brillouin zone. The edge states will have a degeneracy at the time-reversal invariant momenta k=0,π/a, with the spin-orbit interaction lifting this degeneracy in the region between these momenta points. If the edge states cross the Fermi level an even amount of times, the bound states can be pushed out of the gap, meaning an even number of crossings corresponds to the $\nu = 0$ trivial insulator state as shown in Fig. 2.3.a. If the edge states cross the Fermi level an odd number of times like in Fig. 2.3.b, they can not be eliminated and are said to be topologically protected, in this case the material is classified by $\nu = 1$, making it a topological insulator. 3D TIs are classified by 4 $\mathbb{Z}_2$ invariants: $(\nu_0, \nu_1\nu_2\nu_3)$, where $\nu_0 = 1$ signifies strong TI and $\nu_0 = 0$ signifies weak TI, with the other three indices representing the strong or weak topological nature for a specific Miller index of the material. For an introductory review of topological

insulators, and for discussion on AFM TIs refer to [28], [47].

2.7 Magnetic Hamiltonian

Magnetism has played a pivotal role in technical advances that change our world, from compasses used to navigate the globe to nonvolatile computer memory. To understanding the magnetic ground state and excitations of a system we look to the Hamiltonian. A simple magnetic Hamiltonian describing magnetism in MBT is given by

$$H = J\sum_{\langle ij\rangle}\vec{S_i}\cdot\vec{S_j} - K\sum_i (S_i^z)^2 - \vec{H_{ext}}\cdot\sum_i \vec{S_i} \tag{2.36}$$

where $J = J_c z_c/2$ with J_c being the interlayer coupling AFM coupling and $z_c = 6$ corresponds to the number of interlayer nearest neighbors. $S = 5/2$ since Mn has 5 unpaired d-spins. K is the anisotropy term which makes MBT an easy axis magnet. $H_{ext} = g\mu_0 B$ is the applied magnetic field along the $\hat{z}$ direction, with g being the g-factor. Note that we do not include intralayer exchange since in MBT the in-plane exchange is an order of magnitude larger than the out-of-plane exchange. Effectively we model MBT as a 1D spin chain where spins within a layer are represented by a macrospin. Writing S_i^z as $M_1^z = M_0\cos(\theta_1)$ and S_j^z as $M_2^z = M_0\cos(\theta_2)$, where S_1^z and S_2^z are the projections of the magnetizations of the first and second layer along the z direction and θ_1 and θ_2 are the angles the magnetizations make with respect to the z axis. We can rewrite a simplified expression for energy per unit volume E as [53]:

$$\begin{aligned} E &= \frac{H_E}{M}\vec{M_1}\cdot\vec{M_2} - \frac{H_K}{2M}(M_{1z}^2 + M_{2z}^2) - H_{ext}(M_{1z} + M_{2z}) \\ E_M &= \frac{E}{M} = H_E\cos(\theta_1+\theta_2) - \frac{H_K}{2}(\cos^2\theta_1 + \cos^2\theta_2) - H_{ext}(\cos\theta_1 + \cos\theta_2) \end{aligned} \tag{2.37}$$

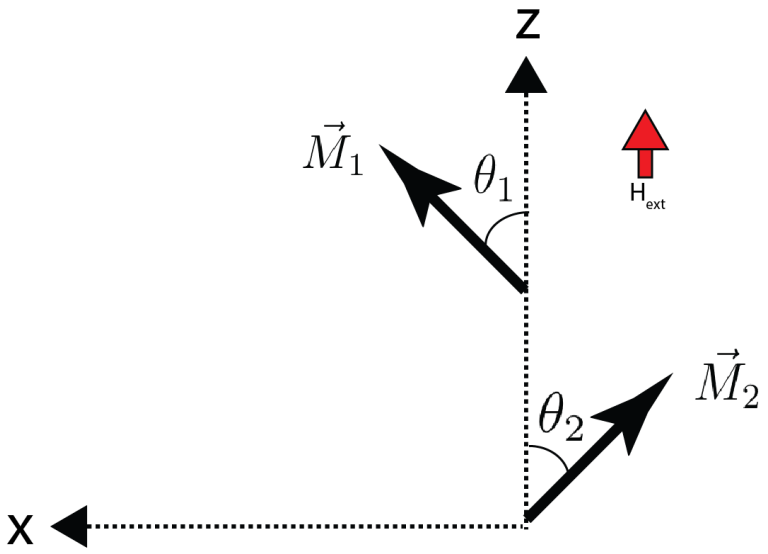

Figure 2.4: .

where $H_E = 2SJ$ and $H_K = 2SK$ are the exchange and anisotropy fields. To find the equilibrium configurations we calculate $\frac{\partial E_M}{\partial \theta_1} = \frac{\partial E_M}{\partial \theta_2} = 0$:

$$\begin{aligned} \frac{\partial E_M}{\partial \theta_1} &= -H_E \sin(\theta_1 + \theta_2) + H_K \cos(\theta_1)\sin(\theta_1) + H_{ext}\sin(\theta_1) = 0 \\ \frac{\partial E_M}{\partial \theta_2} &= -H_E \sin(\theta_1 + \theta_2) + H_K \cos(\theta_2)\sin(\theta_2) + H_{ext}\sin(\theta_2) = 0 \end{aligned} \tag{2.38}$$

A trivial solution to these equations is $\theta_1 = 0$ and $\theta_2 = \pi$, this corresponds to the AFM ground state, with the sub-lattices anti-parallel to each other. A second solution corresponds to $\theta_1 = \theta_2$, plugging this into expression for E_M and using the double angle formula $\sin(2\theta) = 2\sin(\theta)\cos(\theta)$ we get:

$$\begin{aligned} -2H_E \sin(\theta_1)\cos(\theta_1) + H_K \cos(\theta_1)\sin(\theta_1) + H_{ext}\sin(\theta_1) &= 0 \\ -2H_E \cos(\theta_1) + H_K \cos(\theta_1) + H_{ext} &= 0 \\ \cos(\theta_1) &= \frac{H_{ext}}{2H_E - H_K} \\ \theta_1 = \theta_2 &= \arccos(\frac{H_{ext}}{2H_E - H_K}) \end{aligned} \tag{2.39}$$

Plugging in each value of θ into Eq. 2.37 we see that the energies are equal at a field of $H_{ext} = H_c = \sqrt{2H_E H_K - H_K^2}$. For $H < H_c$ the trivial AFM solution will be energetically favorable, whereas for $H > H_c$ the $\theta = \arccos(\frac{H_{ext}}{2H_E - H_K})$ solution will have a lower energy. H_c represents the spin-flop field, where sub-lattices in an AFM suddenly rotate to a more in-plane configuration, usually with a net M_z component. The spin-flop transition is extremely important in MBT as it gives the system a net magnetization in the z-direction and takes the system from a C=0 to a C=1 Chern insulator. For a more thorough investigation of the spin-flop transition in AFMs refer to [53]–[56]. The condition for FM alignment happens when $\theta_1 = \theta_2 = 0$, using the bottom equation of Eq. 2.39 this occurs at $H_{FM} = 2H_E - H_K$. For MBT, using an exchange field of H_E=5.1 T and anisotropy field of H_K=1.58 T [57], respectively, yields H_c=3.69 T and H_{FM}=8.62 T. The calculated spin flop field of 3.69 T matches very well with literature, however the FM alignment field is slightly lower ($\sim$ 7.7T) in experiment [23], [36]. In few-layered materials, with MBT being no exception, even-numbered layered samples will see a surface-spin-flop occur at lower fields than the bulk spin-flop since one of the surface spins will be anti-parallel to the external field and the field to flip that layer's spin will be lower due to the decrease in exchange energy since the surface layer only has one nearest neighbor as opposed to two [58], [59]. This surface-spin-flop grows with external field until, at the bulk spin-flop transition it rapidly grows until the whole sample has a spin-flopped configuration. This is seen in MBT [57], [60], [61], with even layered samples exhibiting a lower spin-flop field than their odd layered counterparts.

It is worth repeating that this is a very simple Hamiltonian, due to the difference in exchange energies we treat in-plane spins as a 1-D macrospin and only include the out-of-plane coupling. Additionally there are many other types of anisotropy such as shape and exchange anisotropy. In particular we assumed that the external magnetic field is applied exactly in the c-axis, in actuality it is exceedingly difficult to make sure your applied field has no in-plane components, and in chapter 5 we

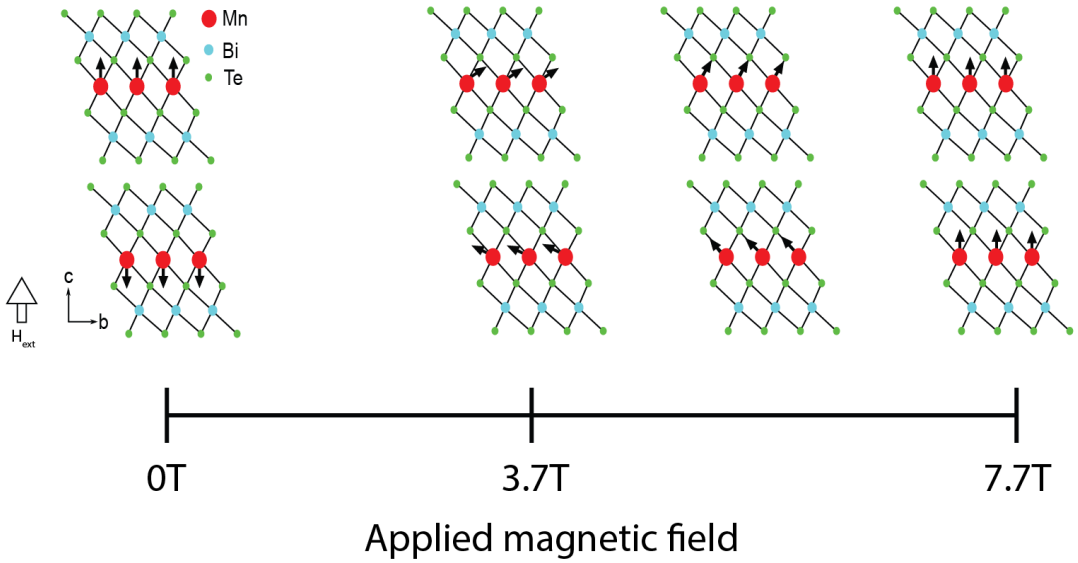

Figure 2.5: **Evolution of AFM state in MBT under applied magnetic field.** Upon application of an external magnetic field along its c-axis, MBT undergoes a spin-flop transition at H_c=3.7 T, with the Mn spins continuously canting up until 7.7 T, when the sample is fully ferromagnetically aligned with the applied field.

will discuss how a small in-plane component of the applied field can transform the magnetic phase transitions as well as the associated magnon dispersion in MBT.

Chapter 3

Experimental Techniques

3.1 Femtosecond Pulsed Lasers

As mentioned in chapter 1, much of physics today is centered around investigating and exploiting perfect processes like superconductivity or topological surface states. Another one of these perfect processes is stimulated emission of radiation, in which an incoming photon of ω_a causes an electron in an excited state to emit a photon at ω_a as it decays to its ground state. Importantly, photons produced by stimulated emission will have the same phase, direction, and energy as the incoming photon which stimulated the emission. Lasers rely on stimulated emission to create a coherent light source.

Femtosecond pulsed lasers, which are utilized for the experiments detailed in this dissertation, usually consist of an oscillator which produces weak, short pulses of light and an amplifier that increases the intensity of the pulses from the oscillator. An oscillator is an optical cavity consisting of two mirrors with gain medium in between, with the gain medium typically being pumped by a diode laser to achieve population inversion. The gain medium is used to store energy which can be accessed by the electric field inside the cavity through stimulated emission. Typically the energy

levels in a gain medium are described as a two level system to demonstrate stimulated emission. However population inversion is only possible in a three-level system (or more), with many commercial lasers using four-level gain media. The cavity supports certain modes which are equally separated in frequency and determined based off of the dimensions of the cavity. The modes will have random phases with respect to each other so the power output will be constant, to achieve pulsed laser operation the modes will have to be locked in phase, this will produce bursts of energy where the energy stored in the gain medium is quickly transferred to the electric field inside the cavity to produce a short pulse of light. Mode locking can be achieved actively with electro-optical or acousto-optical switches, or by synchronous mode locking where the gain medium is pumped by another pulsed laser, effectively turning the gain medium on and off to produce pulses. Mode locking can also be done in a passive manner, one way to do this is with a saturable absorber [62] which absorbs low intensity light and reflects high intensity light. By putting a saturable absorber in the oscillator cavity, high intensity fluctuations of light will necessarily be reflected and travel many round trips through the oscillator. This creates a mode-locked pulse train which has filtered out the low intensity non-mode-locked light.

The pulses produced from an oscillator are usually on the order of a nano-joules. However, for our experiments we require pulses several orders of magnitude higher in energy. To increase the pulse energy from the oscillator the pulses are fed into a regenerative amplifier. A Pockels cell is used to selectively allow a pulse to enter the regen amplifier, where it will stay trapped until it has made enough passes through the gain media to produce a high energy pulse with the desired characteristics, at which point it will pass through another Pockels cell to exit the laser cavity. For a long time the limiting factor in laser operation was the high energy densities achieved in amplifiers would cause nonlinear effects and damage sensitive optics inside the laser. To overcome this problem chirped pulse amplification (CPA) is used. The principle of CPA is straightforward; to avoid damaging the gain media

inside the amplifier the laser pulse is first stretched in time using gratings or prisms, then the low intensity stretched out pulse is sent into the regen where it is amplified, when sufficiently amplified the pulse is compressed upon leaving the laser, avoiding any nonlinear effects like self-focusing and avoiding damage to the laser and gain media [63]. The pioneers of CPA, Donna Strickland and Gérard Mourou, received the Nobel Prize in Physics in 2018.

3.2 Optical Parametric Amplification (OPA)

Pulsed lasers are extremely useful experimental tools, however they come with the drawback of only outputting one color of light, usually at narrow bandwidths. The narrow bandwidths mean that for our Spirit system (which will be described in greater detail later) centered at 1040 nm with a FWHM of < 8 nm we are transform limited in the time domain to a compressed pulse of $\sim$200 fs. This lack of control over frequency means we cannot tune our laser to be resonant to specific optical processes. To overcome this limitation we use Optical Parametric Amplifiers (OPAs) to create broadband laser light over a range of different frequencies. OPAs rely on nonlinear optical processes to both create a broadband white-light spectrum and to amplify the desired frequency.

In Fig. 3.1 the basic OPA process is shown. A pump photon at ω_3 (where $\omega_3 > \omega_1, \omega_2$) inverts the population in a nonlinear crystal while a signal photon, created through white light generation (WLG), at ω_1 causes stimulated emission from the excited virtual state at ω_3. This process causes the pump photon to split up into a signal photon at ω_1 and an idler photon at ω_2. The important thing to note here is that the idler photon also contributes to this process, as it will cause stimulated emission from another virtual ω_3 state, and this emission will in turn produce another ω_1 and ω_2 photon. To obey the conservation of energy the photons must satisfy $\hbar\omega_3 = \hbar\omega_1 + \hbar\omega_2$.

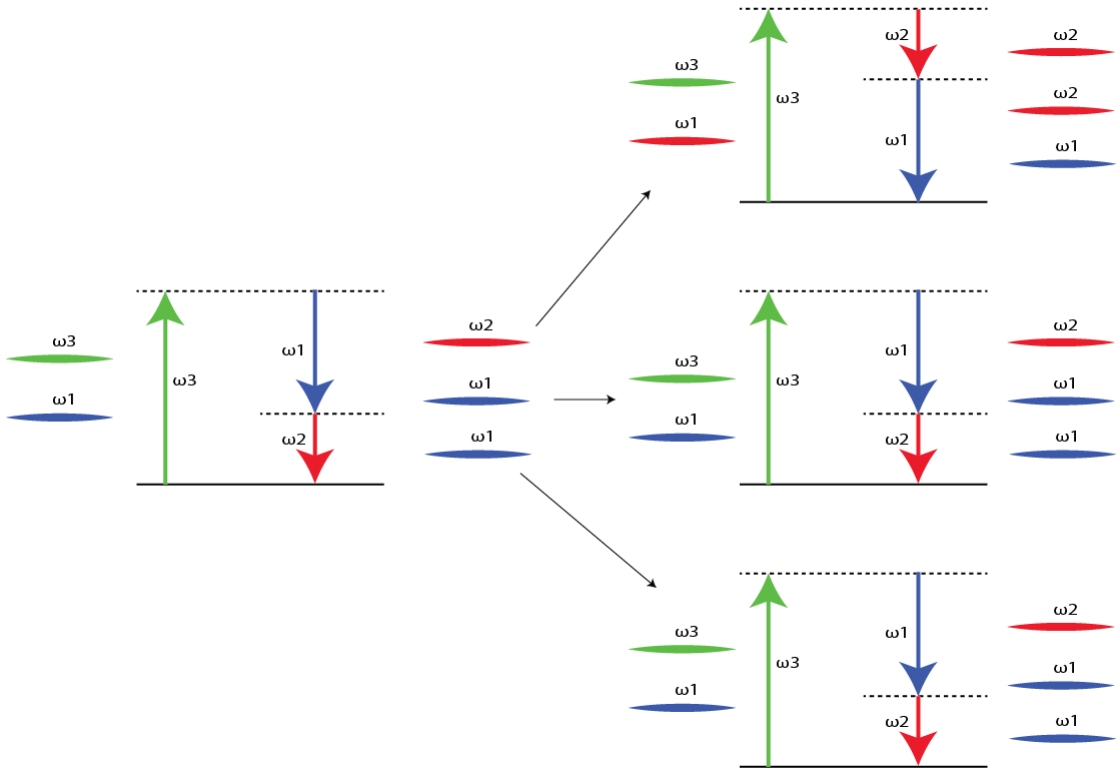

Figure 3.1: **Basic working principle behind OPA process.** Here a basic schematic of an OPA process is shown. In particular this shows that when a pump photon at ω_3 excites a corresponding virtual state a photon at ω_1 (called the signal) can, through spontaneous emission, cause the emission of another ω_1 photon, and due to conservation of energy, another photon (called the idler) is emitted through the difference frequency generation process at $\omega_2 = \omega_3 - \omega_1$. Since the difference in energy between the pump and the signal/idler is just the energy of the idler/signal, in each stimulated emission process 2 photons are generated which contribute to this parametric process, this is the basic idea behind OPAs.

Maxwell's equations for a wave in nonlinear media give [5]:

$$\frac{\partial^2 \vec{E}(z,t)}{\partial z^2} - \mu_0 \frac{\partial^2 \vec{D}(z,t)}{\partial t^2} = \mu_0 \frac{\partial^2 \vec{P_{NL}}}{\partial t^2} \tag{3.1}$$

where $P(t) = \epsilon_0(\chi^{(1)}\vec{E}(t) + \chi^{(2)}\vec{E}^2(t) + \chi^{(3)}\vec{E}^3(t) + ...$ and the electric field present in the nonlinear crystal during this 3-wave mixing is given by $\vec{E}(t) = \frac{1}{2}(\vec{A}_1(t)e^{i(\omega_1 t - k_1 z)} + \vec{A}_2(t)e^{i(\omega_2 t - k_2 z)} + \vec{A}_3(t)e^{i(\omega_3 t - k_3 z)}) + c.c.$. Computing only second order nonlinearities

(E^2 terms) which produce another wave which is present in this process yields:

$$\frac{\partial^2 \vec{P}_{NL}(z,t)}{\partial t^2} = -\epsilon_0(d_{eff}\omega_1^2 \vec{A}_2^*(z)\cdot\vec{A}_3(z)e^{i(\omega_1 t-(k_3-k_2)z)}+ \\ d_{eff}\omega_2^2 \vec{A}_1^*(z)\cdot\vec{A}_3(z)e^{i(\omega_2 t-(k_3-k_1)z)} + d_{eff}\omega_3^2 \vec{A}_1(z)\cdot\vec{A}_2(z)e^{i(\omega_3 t-(k_1+k_2)z)}) \tag{3.2}$$

here d_{eff} represents the effective nonlinear optical coefficient, and depends on the components of $\chi^{(2)}$ which are involved in the second order process [5], [6]. The first term on the right hand side of Eq. 3.2 is DFG between the pump and the idler waves, producing a signal photon from the process. The second term is DFG between the pump and signal waves which produces the idler photons. Finally, the last term represents SFG between signal and idler fields to produce a pump photon [5], [6].

The parametric gain of an OPA is given by the expression [6]:

$$G(L) = \frac{I_1(L)}{I_{10}} = (1 + [\frac{\Gamma}{g}Sinh(gL)]^2) \tag{3.3}$$

where $\Gamma^2 = \frac{2d_{eff}^2\omega_1\omega_2}{c_0^3\epsilon_0 n_1 n_2 n_3}I_3$ and $g = \sqrt{\Gamma^2 - \frac{\Delta k^2}{4}}$, with I_3 being the intensity of the pump beam and Δk the wave-vector mismatch $\Delta k = k_3 - k_2 - k_1$. Clearly the gain is maximized and the OPA process is most efficient when $\Delta k = 0$. This is the condition for momentum conservation: $\hbar k_3 = \hbar k_1 + \hbar k_2$.

The condition $\hbar k_3 = \hbar k_1 + \hbar k_2$, known as the phase matching condition, is one of the most important parameters to optimize when tuning an OPA to a certain wavelength, but it comes with a catch. Using the relation $k_i = \omega_i n_i/c$ we can write the phase matching condition as $\omega_3 n_3 = \omega_2 n_2 + \omega_1 n_1$, substituting $\omega_2 = \omega_3 - \omega_1$ the phase matching condition can be written as $(n_3 - n_2)\omega_3 = (n_1 - n_2)\omega_1$. In isotropic media with positive dispersion ($\frac{\partial\omega}{\partial k} > 0$) if $\omega_3 > \omega_2 > \omega_1$ then $n_3 > n_2 > n_1$, which means $(n_3 - n_2)$ is positive and $(n_1 - n_2)$ is negative, and the same problem occurs in negatively dispersing media ($\frac{\partial\omega}{\partial k} < 0$). From these relations it's clear that the phase matching condition cannot be satisfied in an isotropic media with positive or negative dispersion. To solve this problem we use birefringent material, where the index of refraction, and therefore the propagation speed, varies along different crystal axes,

to satisfy the phase matching condition. In a uni-axial crystal with two ordinary axes (index of refraction n_0) and one extraordinary axis (index of refraction n_e), the index of refraction for a beam propagating at and angle θ to the optical axis of the crystal is given by [5], [6]:

$$\frac{1}{n_e(\theta)} = \frac{\sin^2(\theta)}{n_e} + \frac{\cos^2(\theta)}{n_0} \tag{3.4}$$

A common nonlinear crystal for wavemixing used in many OPAs (including the ones on the Spirit table) is β-Barium Borate (BaB_2O_4) otherwise known as β-BBO. β-BBO is a negative uni-axial crystal ($n_e < n_0$), which means that pump pulse ω_3 must be polarized along the extraordinary axis while the pump and idler beams can either both be polarized along the ordinary axis (Type I phase matching) or cross-polarized (Type II). By tuning θ (which usually amounts to rotating the crystal around its azimuth) and paying close attention to the input polarizations of the pump and signal beam it is possible to satisfy the phase matching condition for a range of wavelengths.

3.3 Experimental setup

Every experiment performed on the Spirit table starts with the fundamental Spirit laser. With 8 W of power and a 209kHz repetition rate, the system provides 38 μJ, 350 fs pulses of 1040 nm light. In Fig. 3.2 the experimental setup used in the experiments mentioned in later chapters is detailed. The output of the Spirit is directed into a beam 50:50 beam splitter, with 4W going into a Noncollinear optical parametric amplifier (NOPA) to be converted into broadband light centered between 660 nm-850 nm for our pump pulses. The other 4 W used are used to create the probe, either by going through a Nd:YAG (Neodymium doped Yttrium Aluminium Garnet) crystal to produce white light (WL) for temporally compressed probe pulses. In experiments where ultrafast time resolution is not needed, like the spin precession

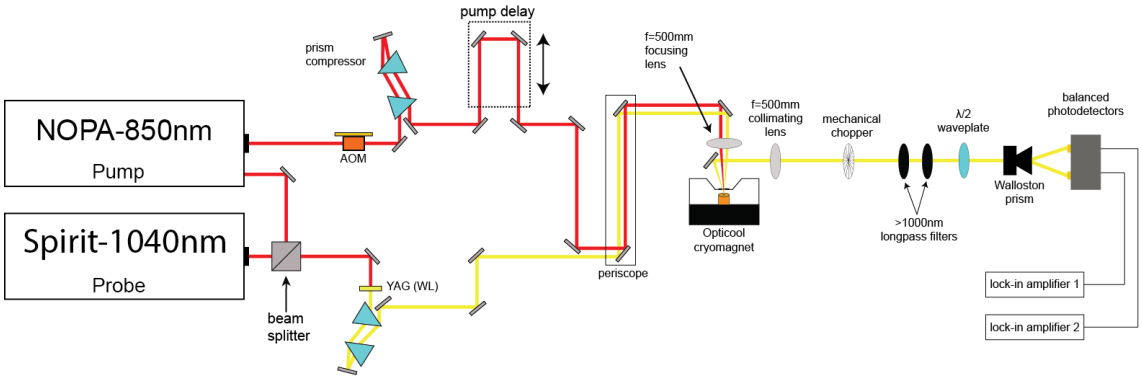

Figure 3.2: **Spirit table experimental layout.** After passing through the beam splitter the probe line is directed into a Nd:YAG (Neodymium doped Yttrium Aluminium Garnet) crystal for white light generation, it is then sent through a prism compressor to ensure ultrafast pulse compression. The probe is directed into the periscope and then through a focusing mirror onto the sample, a pick-off mirror redirects the reflected probe beam into the detection scheme. For time resolved MOKE (TR-MOKE) the detection scheme consists of filters to eliminate pump scatter, a waveplate and a Wollaston prism to balance and separate the probes polarization components onto the balanced photodiode. The pump line starts with half of the fundamental going into the NOPA to create a broadband, temporally compressed pulse between 660 nm-850 nm. Upon exiting the NOPA the pump pulse goes through an acousto-optic modulator (AOM), which chops our pump at 52.25khZ, or a fourth of the Spirit's rep rate, this is vital to our lock-in detection scheme. Next the pump is compressed in time by a prism pair to ensure we have the best time resolution possible, then it is directed into the delay line. The pump then goes into the periscope and through the focusing lens where it is spatially overlapped with the probe on the sample.

data, we simply forgo the white light generation process and use the fundamental 1040 nm, 350 fs pulses from the Spirit.

3.3.1 White light generation

After passing through the beam splitter in Fig. 3.2, the probe is directed into a white light generation set up. White light continuum is a highly complex nonlinear process that relies on self focusing of the beam inside the crystal to form a filament whose intense power density contributes to highly nonlinear processes such as self phase modulation needed for spectral broadening [64]. The super-continuum created by the WL crystal can be used as the seed for optical parametric amplification

(OPA) processes (Sapphire is used as the WL generation crystal in our NOPA), or as a broadband probe which can be highly compressed in time to aid in the detection of ultrafast processes like carrier relaxation and coherent phonons. To achieve stable WL one must carefully optimize the incident power and the numerical aperture (NA). Roughly speaking the NA of the incoming light into the WL crystal should have the same NA as the outgoing super-continuum. For our WL generation we used a 5 mm thick Nd:YAG crystal, focused with a 25 mm lens (collimated using a similar 25 mm lens after WL generation as well) and an input power of ≈250 mW, so there is still around 3.5 W of the Spirit fundamental to use if need be. It is best to have the YAG on a translation stage since the exact point of focusing needs to be carefully tuned inside the crystal for optimization, additionally the YAG should be on a rotation mount, since it is very common for the WL generation crystal to burn and damage, the rotary mount allows you to change the spot on the crystal without changing its position or depth.

3.3.2 Pulse compression

You can't have an ultrafast lab without ultrafast pulses. Due to group velocity dispersion (GVD), $GVD(\omega_0) = (\frac{\partial^2 k}{\partial \omega^2})_{\omega=\omega_0}$, different colors of light will propagate at different speeds through transparent media. This means that by the time an ultrafast pulse travels through all the lenses, windows, neutral density (ND) filters, and other transparent optics present in an experiment, the pulse is no longer compressed and its constituent wavelengths are stretched out in time. To counteract the effect of GVD on our spectrally broad pulses we employ a prism compressor with negative GVD. In Fig. 3.2 we use a prism compressor on both the pump and probe paths to ensure ultrafast time resolution. The goal is to insert the beam enough into the prism compressor such that there are similar amounts of negative GVD (from prism compressor) and positive GVD (from transmissive optics in beam path). To achieve

this we optimized second harmonic generation (SHG) from a BBO crystal by adjusting prism insertion, since SHG intensity goes as electric field squared when the pulse is optimally compressed we will see the largest peak fields and therefore the largest SHG signal. It is important to include all transmissive optics in the beam path you wish to compress, for example we had to take off the window of the cryostat and set it up so that the SHG could be placed after the window to make sure its GVD was accounted for.

3.3.3 Noncollinear Optical Parametric Amplification (NOPA)

In Fig. 3.2 half the Spirit's power is directed into a commercial Spirit NOPA to produce the pump pulses for our experiment. The operation behind the NOPA is similar to the OPA process detailed earlier, except that the phase matching condition is now realized vectorially [6] $\vec{k}_3 = \vec{k}_1 + \vec{k}_2$. Our NOPA provides tuning between 660 nm and 850 nm, for the experiments detailed in later chapters, either 800 nm or 850 nm light was used. From the incident 4 W the NOPA usually produced $\sim$200 mW of 800 nm light. Things like wavelength, time spent optimizing, and age of the NOPA play a role in the output power achieved. The white light crystal starts becoming noticeably damaged after about 6-8 hours and power starts to drift, requiring translation of the WL crystal in the NOPA.

3.3.4 Periscope and focusing onto the sample

Coming out of the NOPA the pump gets sent through an acousto-optic modulator which chops it at a frequency of 52.25 kHz (1/4 Spirit rep rate). After which it is directed into a delay stage, which changes the pump path length, giving us the ability to record data at different pump-probe time delays. After the delay stage the pump along with the probe are both directed vertically up the table and above the Opticool using periscope mirrors which lead to another mirror and an

f=500 mm focusing lens. The last mirror and the focusing lens are both mounted together on a translation stage which has x-y-z degrees of freedom which allow us to take the cleanest data possible. Since we overlap pump and probe on a camera we know that at some depth the are perfectly overlapped on the sample, the z (height) degree of freedom allows us to take scans at different heights and when the signal is maximized we know that the pump and probe are overlapped due to the height being optimized. The x-y degrees of freedom (in the plane of the table) allow us to move the overlapped pump and probe across the surface of the crystal to ensure we find a spot which gives us clean, specular reflection from the surface.

3.3.5 Detection

Once reflected off the sample, a pick-off mirror directs the reflected probe beam through a collimating lens (f=500 mm) and into the detection scheme, seen in Fig. 3.2 on the right hand side after the Opticool. The first component in the detection scheme is a mechanical chopper, operating at 743 Hz, used to record the overall voltage from the probe beam on one of the photodiodes. Next are two >1000 nm longpass filters used to get rid of any pump scatter that may be present, making sure only probe light makes its way into the detector. The next two pieces of optics are integral to the TR-MOKE detection process: a $\lambda/2$ waveplate, and a Wollaston prism. The Wollaston prism spatially separates light into its constituent s- and p-polarized parts, to be directed into the balanced photo-detector. The $\lambda/2$ waveplate is a birefringent crystal which is used to rotate the polarization of light to balance the probe beam on the Wollaston prism so that there are equal parts s- and p- being split onto the balanced photodiodes. More details will be given in the TR-MOKE detection below. For $\Delta R/R$ measurements the Wollaston prism must be removed, and the change in probe reflectivity is recorded on a single photodiode.

3.3.6 Lock-in amplifier

Lock-in amplifiers are the workhorse of many experimental physics labs the world over. While seldom talked about, they are perhaps one of the most important tools for experimental physicists. An age-old problem in science is maximizing signal while minimizing noise to produce the cleanest data possible. In our time-resolved experiments we detect changes in observables such as reflectivity or polarization that are extremely subtle, sometimes registering just hundreds of nanovolts in amplitude. To obtain clean data we implement a chopper/lock-in detection scheme. Like many theoretical and numerical tools in physics, lock-in amplifiers take advantage of orthogonality relations. The SR830 lock-in amplifier used in our experiments takes the probe signal from the detector and multiplies it by a reference signal, usually the chopped pump frequency of 52.25KHz, because sine waves of different frequencies are orthogonal, all other frequency components will average out to zero and the component of the signal which is oscillating at reference frequency will be decomposed into an x and y channel on the lock-in, signifying the in-phase and out-of-phase components of the signal. Since the pump is chopped at 52.25 KHz, setting the reference signal to 52.25 KHz effectively locks-in to the pump-induced changes to the signal. As for the mechanical chopper operating at 743 Hz, we lock in to this frequency to measure the equilibrium voltage of the probe on the detector, which is necessary to make measurements of relative reflectivity or Kerr rotation in radians.

The delay stage usually sits at an individual delay position for 0.9 seconds, meaning the lock-in averages almost 200,000 separate probe pulses for each delay time data point. Averaging over large numbers combined with the lock-in detection scheme gives us excellent signal to noise. To further increase the signal to noise, multiple runs of the complete data sets can be averaged. However, the signal to noise only increases as the square root of the number of scans, meaning that to increase signal to noise by a factor of 10 a total of 100 scans must be averaged.

3.4 TR-Reflectivity

TR-reflectivity measurements consist of a pump pulse used to excite a non-thermal distribution of electrons and a probe pulse used to measure relaxation dynamics of the nonequilibrium, non-thermal electron population. Initially, right after excitation, the non-Fermi distribution created by the pump starts to thermalize, both internally by scattering off of other electrons, and by thermalizing with the lattice [65], [66]. Once the non-Fermi electron distribution has thermalized to a hot Fermi distribution energy exchange with the lattice through electron-phonon scattering relaxes the excited carriers back to equilibrium. It should be mentioned that in optical experiments only direct excitations are possible, meaning that we can only excite electrons to excited states at the same momentum in the Brillouin zone since a photons momentum is negligible compared to the crystal momentum. The change in reflectivity can be related to the dielectric function by [65]:

$$\frac{\Delta R}{R} = \frac{\partial ln R}{\partial \epsilon_1}\Delta\epsilon_1 + \frac{\partial ln R}{\partial \epsilon_2}\Delta\epsilon_2 \tag{3.5}$$

One of the main drawbacks of TR-reflectivity is that it is not as straightforward to analyze the data compared to a conductivity measurement, where you are able to clearly see features like a plasma edge, interband transition, or phonons. With that being said, TR-reflectivity is an excellent tool for many reasons, such as the ability to resolve temporal dynamics from femtoseconds all the way to nanoseconds. The relaxation of the hot Fermi distribution gives us valuable information on the electron-phonon coupling in the material [65]. Along with coupling constants and equilibration times TR-reflectivity measurements can give us a unique perspective of looking at phonons in the time domain, allowing us to get information on the phase and chirp of these lattice excitations.

3.5 TR-MOKE detection

To understand how a change in polarization of our probe light is converted into a voltage on a balanced photodiode, it is useful to work with Jones matrices [8]. Assuming incident s-polarized probe light,the half-wave plate will be set to an angle of $\pi/8$ to ensure equal s and p components from an incident s-polarized probe beam so its Jones matrix will be:

$$\begin{pmatrix} E_{s,I} \\ E_{p,I} \end{pmatrix} = \begin{pmatrix} 1 \\ 0 \end{pmatrix}, R = r_{ss} \begin{pmatrix} 1 & -\tilde{\Theta} \\ \tilde{\Theta} & \frac{r_{pp}}{r_{ss}} \end{pmatrix}, HWP = \frac{1}{\sqrt{2}} \begin{pmatrix} 1 & 1 \\ 1 & -1 \end{pmatrix} \tag{3.6}$$

where R is the reflection coefficient off the sample, with $\tilde{\Theta}$ being the complex Kerr angle from Eq. 2.25. The reflected probe beam will be given by $r_{ss} \begin{pmatrix} E_{s,R} \\ E_{p,R} \end{pmatrix} = \begin{pmatrix} 1 \\ \tilde{\Theta} \end{pmatrix}$. When the reflected light goes through the HWP it will have the form:

$$\begin{pmatrix} E_s \\ E_p \end{pmatrix} = \frac{r_{ss}}{\sqrt{2}} \begin{pmatrix} 1 & 1 \\ 1 & -1 \end{pmatrix} \begin{pmatrix} 1 \\ \tilde{\Theta} \end{pmatrix} = \frac{r_{ss}}{\sqrt{2}} \begin{pmatrix} 1+\tilde{\Theta} \\ 1-\tilde{\Theta} \end{pmatrix} \tag{3.7}$$

The Wollaston prism at the end of the detection scheme simply separates the light into its s- and p-components. On the balanced photo-detector the Kerr intensity is given by $I_s - I_p$, which is effectively channel 1- channel 2. Squaring the electric fields and solving for the Kerr rotation intensity:

$$\begin{aligned} I_\theta = I_s - I_p = \frac{|r_{ss}|}{2}(|1+\tilde{\Theta}|^2 - |1-\tilde{\Theta}|^2) \\ I_\theta = 2R\theta \end{aligned} \tag{3.8}$$

where $R = |r_{ss}|^2$ and θ is the real part of the complex Kerr angle in Eq. 2.25. The change of the Kerr intensity with time is given by

$$\Delta I_\theta(t) = 2\Delta R(t)\theta_0 + 2R_0\Delta\theta(t) \tag{3.9}$$

In the next section it will be shown that the second term on the RHS usually dominates. We can check this by comparing $\Delta\theta(t)$ and $\Delta\eta(t)$ in the time domain

and making sure they do not deviate from each other. If this is the case then we can ignore the first term on the RHS to get:

$$\begin{aligned} \Delta I_\theta(t) &= 2R_0\Delta\theta(t) \\ \Delta\theta(t) = \frac{\Delta I_\theta(t)}{2R_0} &= \frac{I_s(t) - I_p(t)}{2(I_s(t) + I_p(t))} \end{aligned} \tag{3.10}$$

This means that to obtain an accurate measurement of the pump induced Kerr rotation as a function of time, one should divide the data taken from the differential voltage measurement by 4 times the reflectivity on one of the diodes ($I_s(t)$ and $I_p(t)$ should essentially be constant and equal despite the small rotation occurring). To perform ellipticity measurements, one can simply replace the HWP with a quarter waveplate. The analysis above will yield $\Delta I_\eta = 2R_0\Delta\eta(t)$.

While these measurements are relatively straightforward, there are a couple things one should keep in mind. First, we used a mechanical chopper to record the voltage of one of the photodiodes, but the balanced photo diodes have a gain factor (for the TR-MOKE experiments mentioned here it was about 70) associated with the differential voltage channel. When plotting the data one must account for this gain and the static reflectivity to accurately report the Kerr rotation:

$$\Delta\theta(t) = \frac{x(t)}{70 * 4 * aux1(t)} \tag{3.11}$$

the $x(t)$ term is the differential voltage data from the lock-in operating at the pump chopping frequency (channel 1 - channel 2). The $aux1(t)$ term is the R_0 on one of the detectors, the factor of 4 comes from Eq. 3.10 and the fact that we must divide by twice the total R_0, which amounts to 4 times the voltage on one of the photodiodes. The factor of 70 is accounting for the gain of the balanced photodiode.

A second thing to be extremely mindful of when performing TR-MOKE measurements is that if you are recording $\frac{\Delta R(t)}{R}$ measurements as well you must be careful not to accidentally record the Kerr rotation as a voltage change in your reflectivity measurements. It may be tempting to block one photodiode and rotate

the HWP such that all probe light is going into the open photodiode. However since there will be pump induced rotation of the probe, if the Wollaston prism is still in place the voltage on the diode will register a voltage change due to this rotation while still recording a voltage change due to the change in reflectivity. We call this a dirty MOKE measurement. This happened while first taking $\frac{\Delta R(t)}{R}$ measurements on MBT and it took a while to sort out why we were seeing such clear magnetization dynamics in reflectivity data. To be safe, whenever taking $\frac{\Delta R(t)}{R}$ data be sure your probe is not going through any polarization-separating optics after the sample such as a beam splitting polarizer or Wollaston prism. While tedious it is necessary to clean up your probe path to avoid taking a dirty MOKE scan on accident.

3.6 η vs. θ

In the polar MOKE geometry:

$$\tilde{\Theta}(t) = P_b(t) + \tilde{F}(t) \cdot M_z(t) \tag{3.12}$$

where $\tilde{\Theta}$ is the complex MOKE angle and $P_b(t)$ is the generalized pump-induced birefringence that is non-magnetic in origin, $\tilde{F}(t)$ is the complex effective Fresnel coefficient, and $M_z(t)$ is the sample magnetization in the z direction as a function of time. We are only interested in purely magnetic dynamics so we take TR-MOKE scans at both positive and negative magnetic fields. Since the Kerr angle transforms anti-symmetrically under magnetization reversal but the non-magnetic pump-induced birefringence does not this is an effective way of subtracting out non-magnetic signals and making sure the dynamics recovered from a TR-MOKE scan are purely magnetic in nature.

$$\tilde{\Theta}_{3.8T}(t) = \frac{\tilde{\Theta}_{3.8T}(t) - \tilde{\Theta}_{-3.8T}(t)}{2} = \tilde{F}(t) \cdot M_z(t) \tag{3.13}$$

Since $\tilde{F}$ and M_z are both dynamic and changing in time, taking the time

derivative of Eq. 3.13 gives us two terms:

$$\begin{gathered}\Delta\tilde{\Theta}(t) = \Delta\tilde{F}(t)M_{z,0} + \Delta M_z(t)\tilde{F}_0 \\ \frac{\Delta\tilde{\Theta}_0(t)}{\tilde{\Theta}} = \frac{\Delta\tilde{F}(t)}{\tilde{F}_0} + \frac{\Delta M_z(t)}{M_{z,0}} \\ \frac{\Delta\theta(t)}{\theta_0} = \frac{\Delta M_z(t)}{M_{z,0}} + \frac{\tilde{F}_1(t)}{\tilde{F}_1}, \qquad \frac{\Delta\eta(t)}{\eta_0} = \frac{\Delta M_z(t)}{M_{z,0}} + \frac{\tilde{F}_2(t)}{\tilde{F}_2}\end{gathered} \tag{3.14}$$

If the real and imaginary parts of the Fresnel coefficient $\tilde{F}(t)$ are assumed to have different dynamics then the last line of Eq. 3.14 shows that if $\eta(t)$ and $\theta(t)$ have the same dynamics then we can assume the contribution for the Fresnel coefficient term is vanishingly small and that both $\eta(t)$ and $\theta(t)$ reflect purely magnetic behavior from the $\frac{\Delta M_z(t)}{M_{z,0}}$ term [8]. It is common to record both rotation and ellipticity when measuring a change in magnetization on fast timescales, or when the signal is relatively small, to make sure the data is coming from magnetization dynamics and not the parasitic Fresnel dynamics. Below in Fig. 3.3 we see data taken from [67] and [68], where rotation and ellipticity were compared on ultrafast timescales. In [68], Faraday rotation and ellipticity (same as Kerr except in transmission) data was recorded on ferromagnetic films of $CoPt_3$. In [67] the Kerr rotation and ellipticity of ferromagnetic Ni thin films was probed. In both of these studies the disparity between the signals in the ultrafast regime indicates a region of data where the dynamics are not purely magnetic in origin.

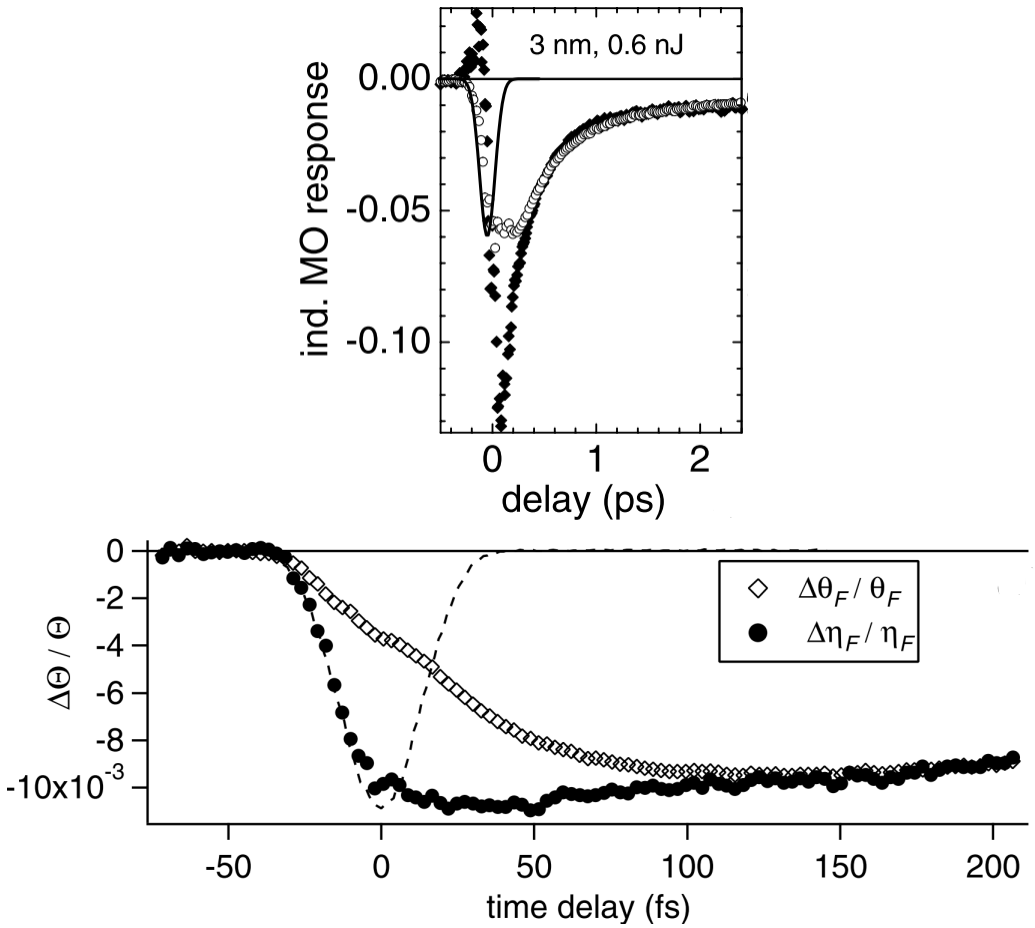

Figure 3.3: Top: Kerr η vs. θ comparison from [67], the filled diamonds correspond to rotation (θ) and the open circles to ellipticity (η). Bottom: Faraday η vs. θ comparison from [68], using a pump fluence of $100\mu J/cm^2$.

Chapter 4

Interlayer magnetophononic coupling in $MnBi_2Te_4$

4.1 Abstract

The emergence of magnetism in quantum materials creates a platform to realize spin-based applications in spintronics, magnetic memory, and quantum information science. A key to unlocking new functionalities in these materials is the discovery of tunable coupling between spins and other microscopic degrees of freedom. In this section we present evidence for interlayer magnetophononic coupling in the layered magnetic topological insulator $MnBi_2Te_4$. Employing magneto-Raman spectroscopy, we observe anomalies in phonon scattering intensities across magnetic field-driven phase transitions, despite the absence of discernible static structural changes. This behavior is a consequence of a magnetophononic wave-mixing process that allows for the excitation of zone-boundary phonons that are otherwise 'forbidden' by momentum conservation. Our microscopic model based on density functional theory calculations reveals that this phenomenon can be attributed to phonons modulating the inter-layer exchange coupling. Moreover, signatures of magnetophononic

coupling are also observed in the time domain through the ultrafast excitation and detection of coherent phonons across magnetic transitions. In light of the intimate connection between magnetism and topology in $MnBi_2Te_4$, the magnetophononic coupling represents an important step towards coherent on-demand manipulation of magnetic topological phases.

4.2 Introduction

The realization of magnetic order in functional quantum materials creates a rich platform for the exploration of fundamental spin-based phenomena, as exemplified in strongly correlated materials [69], multiferroics [70], and more recently, magnetic topological materials [71]. As such, these materials hold great promise for application in spintronics, magnetic memory, and quantum information technology. A new paradigm has recently emerged with the discovery of atomically thin magnets, derived from layered, quasi-two-dimensional materials [72]. In such materials, magnetic order is characterized by strongly anisotropic exchange interactions, with interlayer exchange coupling that is an order-of-magnitude weaker than the in-plane exchange coupling. The weak interlayer exchange coupling offers a high degree of tunability in the two-dimensional limit, enabling the realization of phenomena such as magnetic switching via electric fields [73] and electrostatic doping [74]. Such tunability could potentially be made even more potent in combination with additional functionalities such as those outlined above. For instance, the $Mn(Bi,Sb)_{2n}Te_{3n+1}$ family of layered antiferromagnets is the first experimental realization of intrinsic magnetic order in topological insulators [21], [33], [43]. The interlayer magnetic order is intimately connected to the band topology, with experimental demonstration of switching between quantum anomalous Hall and axion insulator states [27], and realization of a field-driven Weyl semimetal state [75]. In this context, the discovery of new, efficient coupling pathways between the interlayer exchange and other micro-

scopic degrees of freedom would not only add to the rich spectrum of low-dimensional magnetic phenomena, but also potentially unlock pathways for the dynamic manipulation of magnetism and band topology.

In this work, we observe that interlayer magnetic order in $MnBi_2Te_4$ is strongly coupled to phonons, manifesting in the optical excitation of zone-boundary phonons that are otherwise forbidden due to the conservation of momentum. This magnetophononic response is a consequence of a coherent wave-mixing process between the antiferromagnetic order and A_{1g} optical phonons, as determined from equilibrium and time-domain spectroscopy across temperature- and magnetic field-driven phase transitions. Our microscopic model based on first-principles calculations reveals that this phenomenon can be attributed to phonons modulating the interlayer exchange coupling.

4.3 Results

4.3.1 Spectroscopic evidence of magnetophononic coupling

$MnBi_2Te_4$ exhibits magnetic order below a temperature of T_N=24 K, with in-plane ferromagnetic coupling, and out-of-plane antiferromagnetic (AFM) coupling [36],as shown in Fig. 4.1a. With an applied out-of-plane magnetic field, a spin-flop transition occurs at 3.7 T, developing into a fully polarized ferromagnetic-like state (FM) at a critical field of 7.7 T [36].We first present measurements of the phonon spectra across the magnetic phase transitions in $MnBi_2Te_4$,using magneto-Raman spectroscopy. The full polarized Raman phonon spectra, selection rules, and peak assignments can be found in Supplementary Note 1. Our peak assignment is fully consistent with a previous study [76] that investigated Raman phonons in thin flakes of $MnBi_2Te_4$ as a function of number of layers. Here we focus on two fully symmetric "A_{1g}" phonon modes at frequencies of 49 and 113 cm^{-1}, labeled $A_{1g}{}^{(1)}$ and $A_{1g}{}^{(2)}$

respectively. The phonon eigendisplacements, calculated using density functional theory (DFT) simulations, are shown in Fig. 1b. Representative spectra at 0T, in the AFM phase at 15K and the paramagnetic (PM) phase at 35 K, are shown in Fig. 4.1c, d, respectively. We observe that the $A_{1g}{}^{(2)}$ mode clearly exhibits an anomalous increase in scattering intensity in the AFM phase, which has not been reported in previous studies [76]. The temperature-dependence of the $A_{1g}{}^{(1)}$ mode is discussed in detail in Supplementary Note 2. In the following, we focus on the magnetic field-dependent behavior. At a magnetic field of 9 T, where $MnBi_2Te_4$ is in the fully polarized ferromagnetic (FM) state, the spectral weight of both modes decreases, as shown in Fig. 4.1e, f. This is highlighted by subtracting the spectrum at 9 T from the spectrum at 0T and plotting the residual in Fig. 4.1g, h. In Fig. 4.1i, j, the residual is plotted as a function of magnetic field H, upon subtracting the 9 T spectrum. A clear correlation is observed between the residual scattering intensity of the A_{1g} modes and the critical magnetic fields for the spin-flop and FM transitions, denoted by dashed white lines.

The fractional change in integrated intensity of the $A_{1g}{}^{(2)}$ mode is plotted as a function of temperature in Fig. 4.2a (green dots). The integrated intensity follows the AFM order parameter, tracked by the (1 0 5/2) neutron diffraction Bragg peak[23] (purple dots). The gray line is a fit to the power law $I \propto (1 - \frac{T}{T_N})^{2\beta}$, with β=0.35 as in the reference [23]. Furthermore, a plot of the scattering intensity of the $A_{1g}{}^{(1)}$ and $A_{1g}{}^{(2)}$ modes (Fig. 4.2b) as a function of magnetic field reveals the fractional change in integrated intensities of both modes tracks the AFM order parameter**PhysRevX.9.041038** across the spin-flop transition at 3.7 T, and into the fully polarized ferromagnetic state above 7.7 T. The integrated intensities of the $A_{1g}{}^{(1)}$ and $A_{1g}{}^{(2)}$ modes increase by fractions of 0.15 and 0.3 respectively, in the AFM phase, as compared to the FM phase at 9 T. Additionally, the fractional increase in the $A_{1g}{}^{(2)}$ intensity as estimated from the PM to AFM transition and FM to AFM transition in Fig. 4.2a, b, respectively, are of the same magnitude, pointing

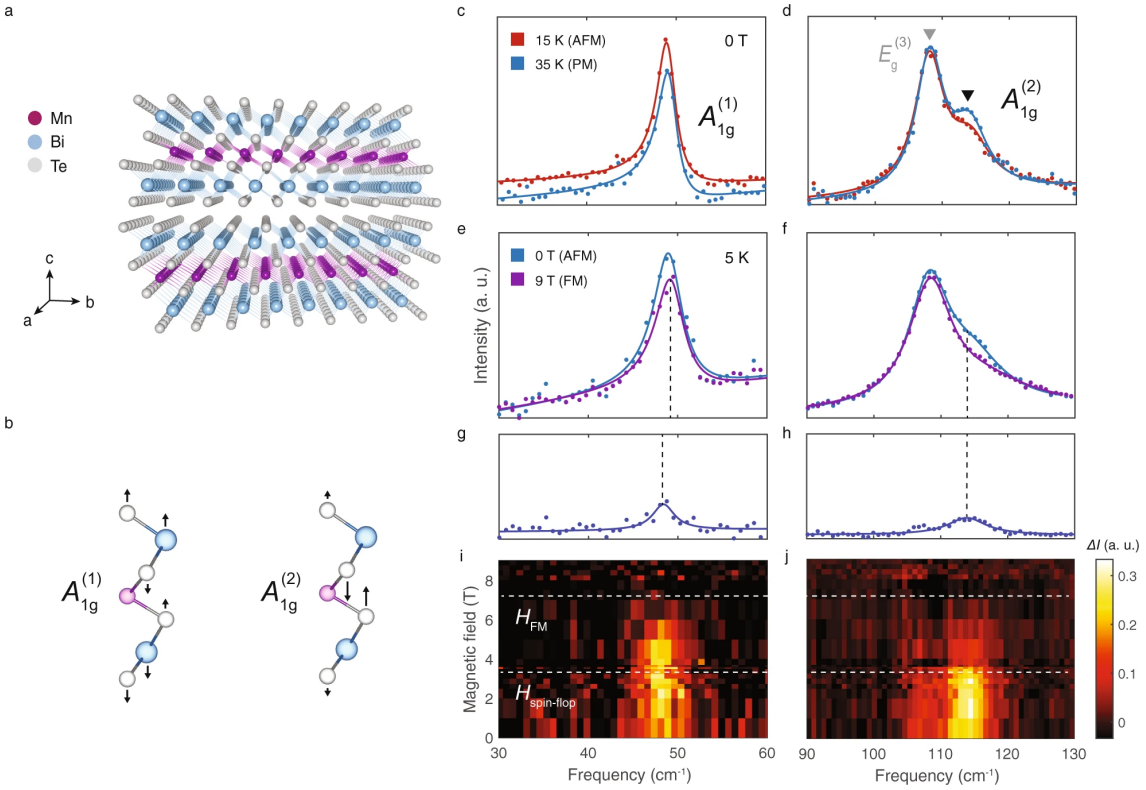

Figure 4.1: **Phonon anomalies across magnetic phase transitions in $MnBi_2Te_4$. a** Crystal structure in $MnBi_2Te_4$. **b.** Eigendisplacements of the $A_{1g}{}^{(1)}$ and $A_{1g}{}^{(2)}$ modes, with arrows denoting the displacement of ions. **c,d** Raman spectra of $A_{1g}{}^{(1)}$(c) and $A_{1g}{}^{(2)}$(d) modes in the paramagnetic (PM) and antiferromagnetic (AFM) phases at 0T, shown in red and blue respectively. **g,h** The difference between spectra in the AFM and FM phases. **i, j** Contour plots of the difference upon subtracting the 9 T spectrum, as a function of magnetic field. The dotted lines denote the FM and spin-flop critical fields.

to a common origin. Importantly, within the limits of our experimental uncertainty (error bars in plots), we do not observe such large changes in the integrated intensity on any of the other Raman phonons (see Supplementary Note 3 for detailed field-dependent data). Below, we show that the experimentally observed temperature- and field-dependent evolution of scattering intensity is consistent with the excitation of 'forbidden' zone-boundary modes of the $A_{1g}{}^{(1)}$ and $A_{1g}{}^{(2)}$ phonon branches.

The AFM order along the out-of-plane direction (crystallographic c-axis)

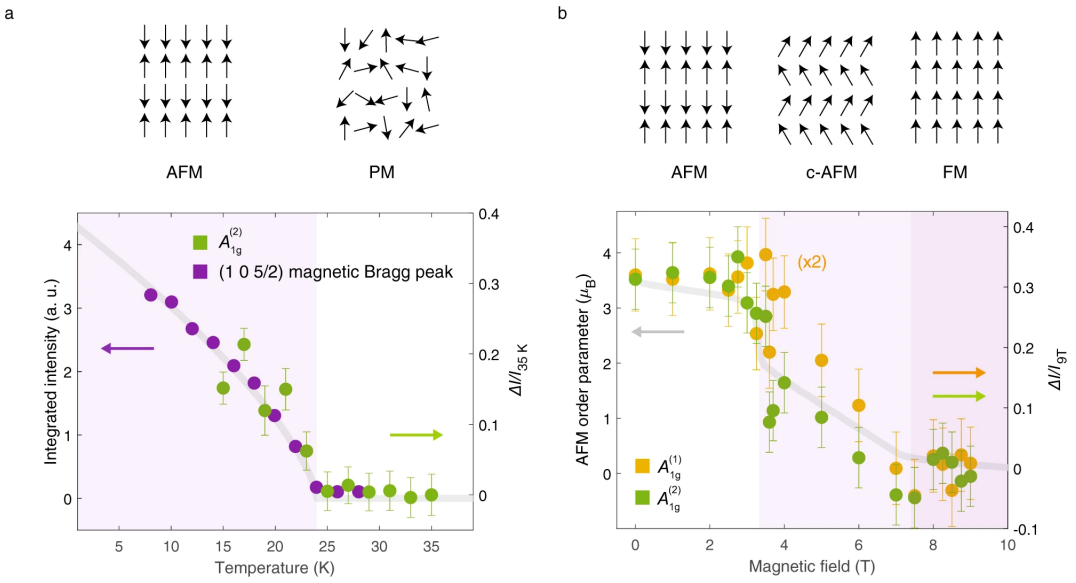

Figure 4.2: **Phonon intensities track the antiferromagnetic order parameter. a** Temperature dependent fractional change in integrated intensity, $\Delta I/I_{35K}$, of the $A_{1g}{}^{(2)}$ mode, overlayed on the integrated intensity of the (1 0 5/2) neutron diffraction peak from reference[23]. The gray line is a fit to $A(1-\frac{T}{T_N})^{2\beta}$ with $\beta = 0.35$, T_N=24 K. **b** The field-dependent fractional change in integrated intensity $\Delta I/I_{9T}$, of the $A_{1g}{}^{(1)}$ and $A_{1g}{}^{(2)}$ modes. The gray line is the AFM order parameter, given by $M - 4.5\mu_B$, where M is the magnetization measured by magnetometry measured by reference**PhysRevX.9.041038**. Error bars are standard deviations in fit values.

results in a magnetic unit cell that is double the size of the crystallographic unit cell, as shown in Fig. 4.3a. In contrast, in the high-field FM state (and the paramagnetic state), the magnetic unit cell is identical with the crystallographic unit cell, as in the paramagnetic state. This behavior manifests in the anomalous field-dependent scattering intensity of the A_{1g} modes, which follows the AFM order parameter with the magnetic unit cell doubling resulting in a folding of the phonon Brillouin zone, allowing for the optical detection of zone-boundary phonon modes. DFT simulations of the phonon dispersion along the out-of-plane direction reveal a flat dispersion for the $A_{1g}{}^{(2)}$ mode, and a small dispersion for the $A_{1g}{}^{(1)}$, consistent with the weak interlayer van der Waals interaction, and our experimental results, denoted in Fig. 4.3b using

bold circles. This supports our assignment of the anomalous scattering intensity as zone-boundary modes. We also consider and rule out alternative explanations for the observed temperature- and magnetic field-dependent scattering intensity changes, such as resonant Raman effects (see Supplementary Note 5) and possible magnon resonances overlapping with the considered phonons (see Supplementary Note 6).

Magnetic unit cell doubling resulting in the activation of zone-boundary phonons is unexpected given the absence of a structural phase transition. Refinement based on neutron diffraction at 10 and 100 K shows no structural unit cell doubling across the AFM transition, and no changes to the unit cell coordinates to within 10^{-3} of the lattice parameters [23]. The negligible change in the spectra of other Raman phonons in $MnBi_2Te_4$ is also consistent with the absence of a structural transition of any kind, and points instead to a mechanism that is mode-dependent.

4.3.2 Microscopic model of magnetophononic wave-mixing

In general, zone-boundary modes are optically inactive or "forbidden" due to the conservation of crystal momentum. Photons in the visible part of the spectrum have negligible momentum in comparison with the crystal Brillouin zone, and thus momentum conservation dictates that only zero momentum (i.e., zone-center) excitations can be generated and detected in first-order scattering processes. This is shown schematically for Raman scattering in Fig. 4.3c. This selection rule can be overcome in the presence of other finite-momentum waves in the crystal, as observed for instance in the case of structural distortions that double the crystallographic unit cell [77]–[79]. However, as noted above, $MnBi_2Te_4$ does not exhibit any structural transition. Instead, we propose that the crystal momentum is provided by the AFM order, via a magnetophononic wave-mixing process. This is shown schematically in Fig. 3c, where the AFM crystal momentum qAFM=$2\pi/2c$ interacts with the phonon crystal momentum, allowing for the excitation of zone-boundary (q=π/c) phonons.

Magnetophononic wave-mixing requires a sufficiently strong scattering cross-section to be observable. This scattering cross-section can typically be written in terms of an interaction term in the free energy. For example, the Raman scattering process is due to a coupling of the incident (E^i) and reflected (E^r) electric fields to a distortion u along a phonon normal mode, via the susceptibility χ_e (i.e., $F = \frac{d\chi_e}{du} u E_i E_r$). In the case of a finite-momentum structural distortion, phonons couple to the structural distortion through elastic interactions. Analogously, in our model of magnetophononic wave-mixing, phonons couple to the AFM order by modulating the interlayer exchange interaction $J^\perp$. The corresponding interaction term in the free energy can be obtained by first writing down a Heisenberg-like Hamiltonian for the spin energy, $\sum_{ij} J_{ij} S_i \cdot S_j$ where J_{ij} is the exchange coupling between spins at sites i and j. Since the coupling is to an out-of-plane antiferromagnetic spin wave, we focus on the interlayer (out-of-plane) exchange coupling $J^\perp$ (only nearest-neighbor interlayer interactions are considered). If a phonon modulates the interlayer exchange interaction, the perturbed exchange coupling $J^{\perp\prime}$ can be written as

$$J^{\perp\prime} = J^\perp + \frac{dJ^\perp}{du} u + ... \tag{4.1}$$

Equation 4.1 is a special case of what is broadly referred to in the literature as "spin–phonon coupling" (see Supplementary Note 4 for the interpretation of higher-order terms in terms of phonon frequency renormalization). Based on this, the free energy term that couples the antiferromagnetic spin wave to the phonon is, to first order,

$$F = (\frac{dJ^\perp}{du} u) \sum_i S_i S_{i+1} \tag{4.2}$$

where i and i+1 correspond to nearest-neighbor spin pairs in the out-of-plane direction. It is clear that the magnitude of this coupling directly depends on $\frac{dJ^\perp}{du}$. In other words, a magnetophononic wave-mixing is possible only when the phonon mode under consideration sufficiently modulates the interlayer exchange coupling.

A microscopic basis for this model can be obtained using DFT simulations. We simulate the modulation of the interlayer exchange coupling $J^{\perp}$ by the six Raman phonons $MnBi_2Te_4$, which include three A_{1g} modes (pure out-of-plane eigendisplacements), and three E_g modes (pure in-plane eigendisplacements, see Supplementary Fig. 4.5b for eigendisplacements). The results, shown in Fig. 4.3d, indicate a striking dichotomy between the out-of-plane A_{1g} modes and in-plane E_g modes. The A_{1g} modes exhibit an order-of-magnitude larger modulation of $J^{\perp}$ than the E_g modes. Furthermore, the ${A_{1g}}^{(2)}$ mode has by far the largest influence on $J^{\perp}$, consistent with our experimental observation of zone-boundary scattering intensity. A quantitative comparison of this model with our experimental results is possible. This is accomplished by defining an experimental magnetophononic scattering cross-section σ, as the ratio of the integrated intensity of the zone-boundary mode (i. e. the residual spectra in Fig. 4.1g, h) to that of the zone-center mode (spectra at 9 T in Fig. 4.1e, f). The scattering cross-section is compared to the calculated interaction term, $|\frac{dJ^{\perp}}{du}|$. The plotted results in Fig. 4.3e show a good agreement between theory and the experiment. In particular, the model reproduces the experimental observation of the ${A_{1g}}^{(2)}$ mode exhibiting the largest zone-boundary scattering intensity. We note that no signature of a zone-boundary mode was observed in the ${A_{1g}}^{(3)}$ branch within the experimental uncertainty (see Supplementary Note 3). Finally, also in agreement with the theoretical prediction, no E_g zone-boundary modes were experimentally observed, i.e., $\sigma = 0$ for all E_g modes, within the experimental uncertainty (see Supplementary Note 3).

The theoretical results outlined above can be rationalized in terms of microscopic interlayer exchange pathways. In general, the exchange coupling across a van der Waals (vdW) gap is understood to be the result of a process named "super-superexchange" (SSE) [80]. In SSE, given that the interlayer exchange interaction is usually much weaker than the intralayer exchange interaction, the two can be effectively decoupled. The individual quasi-two-dimensional layers are treated as macro-

scopic magnetic moments established by the intralayer super-exchange (shown in pink in Fig. 4.3f), which couple across the vdW gap via the weaker interlayer exchange (shown in blue in Fig. 4.3f). As in any exchange process, geometrical parameters that influence the relevant hopping integrals play a major role. In superexchange, the angle between magnetic ions and its ligands mediates the superexchange, in this case the Mn–Te–Mn bond angle θ shown in Fig. 4.3f. These structural superexchange interactions are further controlled by orbital hybridization with cationic Bi p states tuned by the nearest-neighbor ions across the vdW gap [81], in this case, determined by the Te–Te distance Δ shown in Fig. 4.3f, to stabilize the FM interlayer coupling in $MnBi_2Te_4$.

We first note that A_{1g} modes in $MnBi_2Te_4$ modulate Δ whereas E_g modes do not, an observation that accounts for the dichotomy of their respective influence on $J^{\perp}$. Of the A_{1g} modes, examining the eigenvectors in Fig. 4.1b and Supplementary Fig. 1b, ${A_{1g}}^{(2)}$ exhibits the largest modulation of the Mn–Te–Mn bond angle θ. The modulation of θ by the ${A_{1g}}^{(2)}$ mode is a factor of 2 larger than by ${A_{1g}}^{(1)}$, which in turn is a factor of 5 larger than by ${A_{1g}}^{(3)}$. This rationalizes the trend seen in the calculated $\frac{dJ^{\perp}}{du}$ in terms of the SSE pathways.

4.3.3 Time-domain signatures of magnetophononic coupling.

Finally, we investigate magnetophononic coupling by direct measurement of phonons in the time domain. To do this, we carry out "pump-probe" experiments to generate and detect coherent optical phonons as a function of magnetic field (see schematic in Fig. 4.4a). Excitation with ultrafast optical pump pulses (1.55 eV, 50 fs) results in the generation of coherent phonon oscillations. A second, time-delayed probe pulse (1.2 eV, 50 fs) measures pump-induced changes in the transient reflectivity (ΔR/R). The transient reflectivity is sensitive to changes in carrier density and coherent phonons. These measurements are carried out at 2 K, as a function of

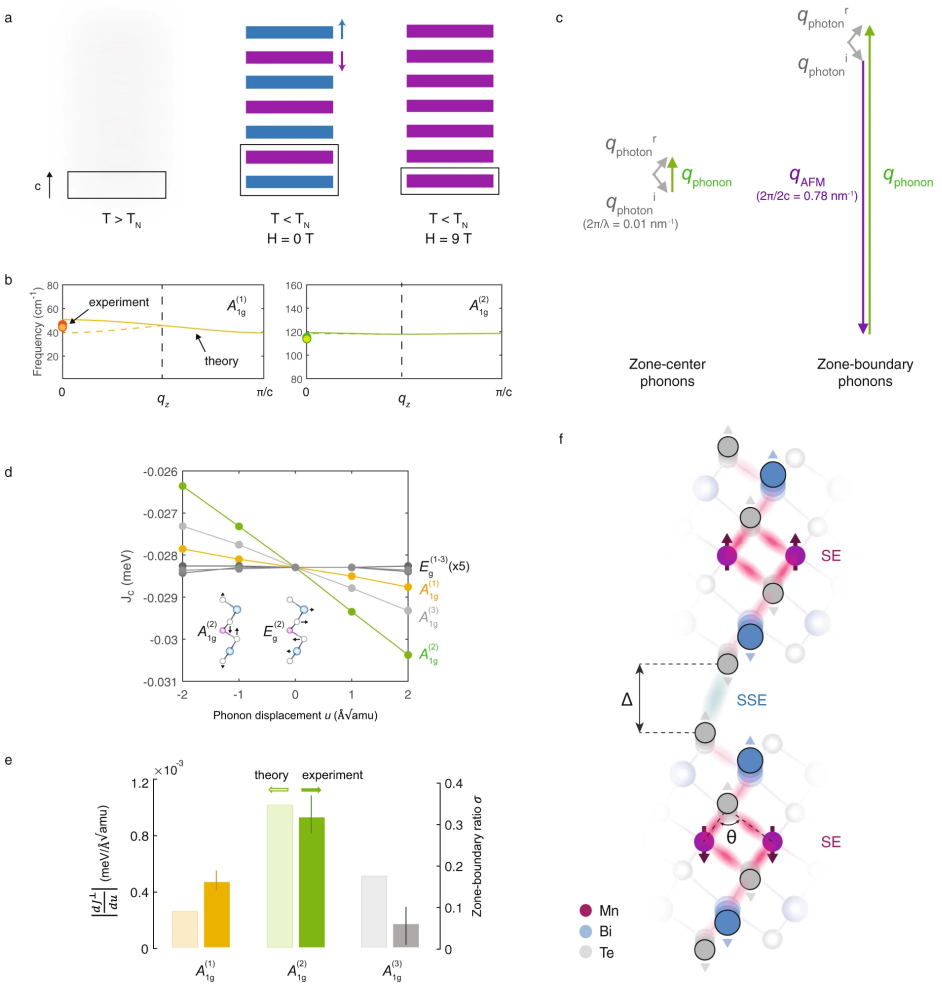

Figure 4.3: **Magnetophononic wave-mixing.** **a** Schematic of layered magnetic ordering in $MnBi_2Te_4$, with blue and purple denoting opposite in-plane spin orientations, and gray denoting disordered spins. The antiferromagnetic (AFM) wavevector is shown schematically, labeled "qAFM". **b** The dispersion relations of the $A_{1g}{}^{(1)}$ and $A_{1g}{}^{(2)}$ modes along the c-axis, calculated using density functional theory. The experimental zone-center and zone-boundary phonon frequencies are denoted using colored and empty circles respectively. **c** Schematic of wave-mixing for zone-center and zone-boundary modes. The wavevectors of the photon (i = incident, r = reflected), phonon, and AFM spin-wave are shown using gray, green, and purple arrows (not drawn to scale). **d** Modulation of the interlayer exchange coupling $J^{\perp}$ by Raman phonons. Inset shows the eigendisplacements of two representative phonons. **e** Comparison between the calculated magnetophononic scattering cross-section $|\frac{dJ^{\perp}}{du}|$ and the experimental zone-boundary ratio σ (see text for definition). Error bars are standard deviations in fit values. **f** Schematic of superexchange (SE) and super-superexchange (SSE), with Δ denoting the interlayer distance, θ denoting the Mn–Te–Mn bond angle, and pink and blue clouds denoting SE and SSE pathways, respectively.

magnetic field from 0 to 6.4 T, across the spin-flop transition. The transient reflectivity, shown in Fig. 4.4b, exhibits an initial sub-picosecond dip, followed by a slow relaxation. Overlayed on this are multiple distinct coherent oscillation components that (as described below), correspond to the $A_{1g}{}^{(1)}$ and $A_{1g}{}^{(2)}$ phonons. We normalize the pump-probe reflectivity traces with respect to their maximum amplitudes, to account for field-dependent variation in the absorbed fluence, and thus photo-carrier density, which can influence coherent phonon amplitudes (see Supplementary Note 7 and Supplementary Fig. 4.12 for detailed discussion). Upon subtracting biexponential fits (black line fit to 0T data in Fig. 4.4b shown as a representative example), we observe that the normalized phonon oscillation amplitudes in the residual $\Delta R/R$ in Fig. 4.4c visibly decrease with increasing magnetic field, much like the phonon spectral weights measured using Raman spectroscopy. The individual oscillatory components are obtained by fitting the residual $\Delta R/R$ to the sum of two exponentially decaying sinusoidal functions (see Methods) as shown for the representative 0 T data in Fig. 4.4d The individual sinusoidal functions, shown in Fig. 4.4e, are readily identified as the $A_{1g}{}^{(1)}$ and $A_{1g}{}^{(2)}$ modes at 1.47 THz (49 cm^{-1}) and 3.44 THz (115 cm^{-1}), respectively. Plotting the amplitudes of the two coherent phonon modes as a function of magnetic field in Fig. 4.4e, it is clear that both modes track the AFM order parameter denoted by the solid gray line, in striking similarity to the field-dependent change in the Raman scattering intensities.

The detection of coherent phonons in pump-probe experiments occurs through a process that is identical to spontaneous Raman scattering [82], [83]. The generation of coherent phonons can also be described within a Raman formalism, with the real and imaginary parts of the Raman tensor responsible for phonon excitation in transparent and absorbing materials, respectively [82]. The similarity of the magnetic-field-dependent coherent phonon amplitudes in Fig. 4.4f to the static Raman scattering intensities in Fig. 4.2b thus suggests that these are a consequence of the same mechanism, namely the excitation of zone-boundary phonons via the

crystal momentum associated with the antiferromagnetic order.

For resonant excitation of $MnBi_2Te_4$ with 1.55 eV pulses, phonon excitation through the imaginary part of the Raman tensor may be physically thought of in terms of a "displacive" excitation [84], where the ultrafast excitation of carriers by the pump pulse shifts the quasi-equilibrium coordinates of the lattice in a spatially and temporally coherent manner, generating coherent phonons. Within this picture, magnetophononic zone-folding as described in the previous section would allow for the generation of both zone-center as well as nominally zone-boundary A1g modes. Additionally, the electronic excitation that shifts the quasi-equilibrium coordinates may itself have a $q_z = \pi/c$ component owing to the contrast in spin-split electronic bands in alternating layers, acting as a direct driving force for the generation of zone-boundary phonons. Unfortunately, the small frequency splitting of the A_{1g} modes precludes the explicit resolution of zone-boundary phonons in the time domain. Nonetheless, it is clear from Fig. 4.4f that the coherent phonons track the AFM order parameter in accord with the magnetophononic wave-mixing proposed here.

We note that in general, phonons in time-domain measurements are expected to exhibit qualitative deviations from steady-state spectroscopy, owing to the nonequilibrium nature of the former. While the ultrafast carrier excitation in displacive phonon excitation is itself a manifestly nonequilibrium process, additional deviations may emerge from nonequilibrium phonon interactions. We directly measure the timescale of phonon equilibration using ultrafast electron diffraction (see Methods). Here, pump-induced changes in the root-mean-square displacements $\langle u^2 \rangle$ of ions through carrier-lattice and lattice thermalization appear in the transient intensity of Bragg peaks through the Debye-Waller effect (see Supplementary Note 8). These measurements require an order-of-magnitude higher pump excitation fluence than the optical pump-probe measurements (see Methods) in order to produce a discernible signal. Regardless, these high fluence measurements set a lower bound for

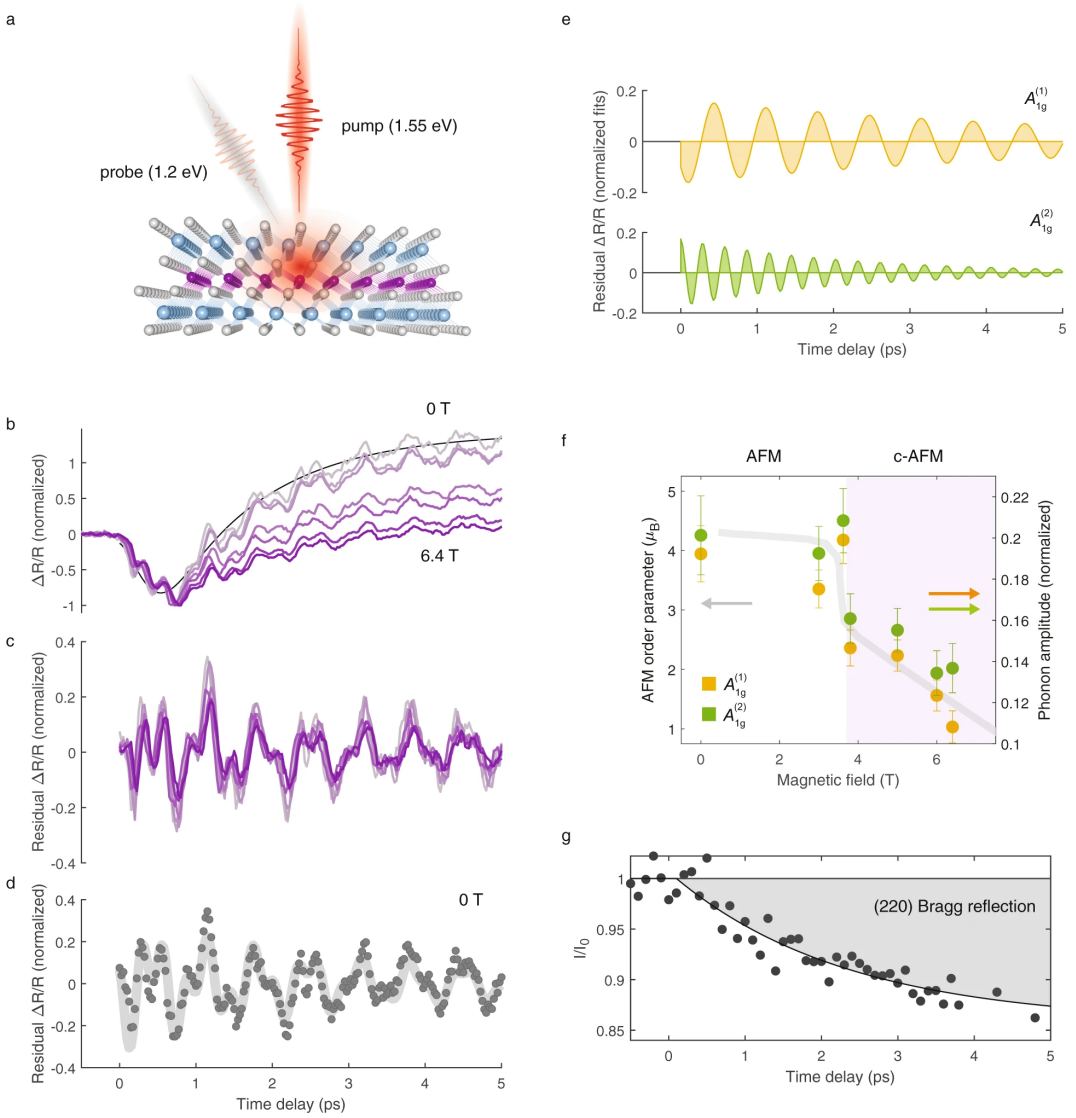

Figure 4.4: **Ultrafast signatures of magnetophononic wave-mixing.** **a** Schematic of pump probe measurement. **b** Pump-induced changes in the transient reflectivity (ΔR/R) as a function of time delay at various magnetic fields, normalized to the maximum amplitude. The black line is a representative biexponential fit to the 0T data. **c** The residual ΔR/R upon subtracting a biexponential fit. **d** Residual ΔR/R at 0T, with black dots denoting experimental data points and the gray line denoting the fit to the sum of two decaying sinusoidal functions. **e** Individual decaying sinusoidal components obtained from the fit in(**b**), corresponding to the $A_{1g}{}^{(1)}$ (top) and $A_{1g}{}^{(2)}$ (bottom) phonons, respectively. **f** Initial amplitude of the $A_{1g}{}^{(1)}$ and $A_{1g}{}^{(2)}$ phonons obtained from fit result in (**b**). The gray line is the antiferromagnetic order parameter from reference**PhysRevX.9.041038**. **g** Measured transient electron diffraction intensity of the (2 2 0) Bragg peak, with black dots denoting experimental datapoints, and the black line denoting the fit to an exponential decay function. Error bars are standard deviations in fit values.

the phonon thermalization time, as discussed in Supplementary Note 8. As a representative sample, we show in Fig. 4.4g, the transient intensity of the (2 2 0) Bragg peak, with the evolution of the peak intensity fit to an exponential decay (black line). The results indicate that phonon populations indeed remain in a nonequilibrium state through the entire time delay range considered. It is noteworthy that clear signatures of magnetophononic coupling are observed even under such nonequilibrium conditions. Finally, we mention that there may possibly be additional contributions to the coherent phonon amplitudes from magnetodielectric effects which are not explicitly accounted for here. We discuss the possible contributions to coherent phonon amplitudes due to such an effect Supplementary Note 7.

4.4 Discussion

We have demonstrated that optically "forbidden" zone-boundary phonons are observed due to magnetophononic wave-mixing in $MnBi_2Te_4$. While it is uncommon for purely magnetic unit cell doubling to give rise to phonon zone-folding effects, such signatures were first observed in transition metal dihalides [85]. These observations were rationalized in terms of phenomenological models of electron-phonon coupling that took into consideration phonon modulation of the spin–orbit coupling and exchange interactions [85], [86]. Our model instead considers the scattering cross-section between the AFM order and phonons, arriving at qualitatively similar conclusions. Importantly, our work provides a description of such a model using first-principles theory. The excellent agreement between the theory and experimental results not only validates the model, but also provides a microscopic basis for the observed phenomena in terms of SSE interlayer exchange pathways. Our work may also help rationalize similar phenomena recently reported [87], [88] in other quasi-two-dimensional magnets such as CrI_3 and $FePS_3$.

Our discovery is especially of significance in light of the critical role played by

tunable interlayer exchange interactions in layered magnetic materials. For instance, in $MnBi_2Te_4$, the interlayer magnetic ordering can drive topological phase transitions between quantum anomalous Hall and axion insulator states. Our work unlocks the possibility of controlling the interlayer magnetic ordering in $MnBi_2Te_4$ by exploiting the strong coupling of A_{1g} phonons to $J^{\perp}$. A promising route towards the ultrafast control of magnetism in $MnBi_2Te_4$ is the use of resonant THz excitation to drive large amplitude distortions along A_{1g} modes, as opposed to employing carrier-based mechanisms (such as displacive excitation) that suffer from ultrafast heating effects, which limit the amplitude of coherent phonons. This may be through anharmonic coupling to Raman-active modes [89], or alternatively through sum-frequency ionic Raman scattering [90]. Such mechanisms based on resonant coupling have been used to drive ultrafast light-induced magnetic oscillations and phase transitions, as experimentally demonstrated in other materials [91]–[97]. Experimental studies [98] on Bi_2Se_3, a material closely related to $MnBi_2Te_4$, have demonstrated the feasibility of ionic Raman scattering as a way to drive large amplitude oscillations along Raman-active modes. Recent theoretical work[99] has outlined an approach based on anharmonic phonon interactions in $MnBi_2Te_4$. In particular, it was shown that resonant excitation of an IR-active A_{2u} phonon (at a frequency of 156 cm^{-1} = 4.7 THz) could drive large amplitude oscillations, which via anharmonic coupling, would drive a unidirectional distortion along Raman- active A_{1g} modes such as the ones identified in the present work. It was predicted that such an approach could be used to drive an AFM to FM transition concurrent with a topological phase transition, using experimentally accessible ultrafast modalities. The magnetophononic wave-mixing in the present work provides an experimental foundation for such approaches and a path toward achieving ultrafast light-induced topological phase transitions.

4.5 Methods

4.5.1 Crystal growth and characterization.

Single crystals of $MnBi_2Te_4$ were grown using a self-flux method11. Mixtures of 99.95% purity manganese powder, 99.999% bismuth shot, and 99.9999+% tellurium ingot with a molar ratio Mn:Bi:Te = 1:10:16 were loaded into an aluminum crucible and sealed in evacuated quartz tubes. The mixture is heated up to 1173 K for 12 h and slowly cooled down at the rate of 1.5 K/h to 863 K. This is followed by centrifugation to remove excess flux. The phase and crystallinity of the single crystals were checked by X-ray diffraction. The antiferromagnetic order with the Néel temperature of 24 K was confirmed using SQUID magnetometry.

4.5.2 Raman spectroscopy measurements.

Temperature-dependent Raman spectra were collected using a Horiba LabRam HR Evolution with a freespace Olympus BX51 confocal microscope. A 632.8 nm linearly polarized HeNe laser beam was focused at normal incidence using a LWD 50× objective with a numerical aperture of 0.5, with the confocal hole set to 100 μm. A Si back-illuminated deep depleted array detector and an ultra-low-frequency volume Bragg filter were used to collect the spectra, dispersed by a grating (1800 gr/mm) with an 800 mm focal length spectrometer. The system was interfaced with an Oxford continuous-flow cryostat for low-temperature measurements, using liquid helium as the cryogen.

Field-dependent magneto-Raman spectra were collected using a home-built Raman spectrometer. A 632.8 nm linearly polarized HeNe laser beam was focused at normal incidence using a LWD 50x objective with a numerical aperture of 0.82. A Si back-illuminated deep depleted array detector and a set of ultra-low-frequency volume Bragg filters were used to collect the spectra, dispersed by a grating(1800

gr/mm) with a 300 mm focal length spectrometer. The system was interfaced with an Attocube AttoDRY 2100 closed-cycle cryostat for low-temperature, high magnetic-field measurements, using liquid Helium as the cryogen. The field-induced Faraday rotation in the objective was calibrated and corrected using a half-waveplate.

The laser power was maintained below 50 μW in all measurements, to minimize laser heating and maintain the power well below the damage threshold. Laser heating was calibrated by measuring Raman phonon peak shifts as a function of and using thermal conductivity values from reference [23]. Polarized spectra were obtained using a half-waveplate to rotate the polarization of the incident beam, with a fixed analyzer.

After peak assignment using polarization analysis, temperature- and field-dependent spectra were collected without a polarizer, to maximize signal throughput. Spectra were averaged over 60 and 120 min in the case of temperature-dependent and field-dependent measurements respectively, with a temperature stability of $\pm$0.1 K. Any subtle drift in the spectrometer ($<$0.15 cm^{-1}) over the temperature-dependent studies was corrected using the HeNe line at 632.8 nm.

The $A_{1g}{}^{(1)}$ peak was fit using an inverse Fano lineshape in combination with a linear background. Its lineshape is given by the expression $I(\omega) = \frac{(q\Gamma-(\omega-\omega_0))^2}{\Gamma^2+(\omega-\omega_0)^2}$ where I is the scattering intensity, ω is the energy, ω_0 and Γ are the resonant energy and linewidth of the excitation respectively, and 1/q is a measure of the peak asymmetry. The $E_g{}^{(2)}$ and the $A_{1g}{}^{(3)}$ peaks were fit with a standard Gaussian lineshape, and the $E_{1g}{}^{(3)}$ and the $A_{1g}{}^{(2)}$ peaks were fit with a standard Lorentzian lineshape. A nonlinear least-squares fitting procedure was used. To ensure robustness of the temperature-dependent fits, the same initial fit values and constraints were used for each set of temperature-dependent and field-dependent spectra.

4.5.3 Magnetic field-dependent ultrafast optical spectroscopy.

Ultrafast optical pump-probe measurements were carried out using a 1040 nm 200 kHz Spectra-Physics Spirit Yb-based hybrid-fiber laser coupled to a noncollinear optical parametric amplifier. The amplifier produces <50 fs pulses centered at 800 nm (1.55 eV), which is used as the pump beam. The 1040 nm (1.2 eV) output is converted to white light, centered at 1025 nm with a FWHM of 20 nm, by focusing it inside a YAG (Yttrium Aluminum Garnet) crystal. The white light is subsequently compressed to ∼50 fs pulses using a prism compressor pair and is used as the probe beam. The pump and the probe beams are aligned to propagate along the [001] axis of the crystal, at near normal incidence.

The samples were placed in a magneto-optical closed-cycle cryostat (Quantum Design OptiCool). Pump-probe measurements were carried out as a function of magnetic field applied normal to the sample surface (along the [001] direction). The sample temperature was fixed at 2 K. A pump fluence of ∼100 $\mu J/cm^2$ was used in order to generate sufficiently large coherent phonon oscillations, while keeping the transient heating to a minimal amount, to ensure we avoid melting of the magnetic order.

4.5.4 Ultrafast electron diffraction measurements.

Ultrafast electron diffraction measurements were carried out at the MeV-UED beamline at the SLAC National Accelerator Laboratory. The principle and other technical details of the experimental setup are outlined elsewhere [100]. A 60-fs laser pulse with a photon energy of 1.55 eV and fluence of 7 mJ/cm^2 were used to excite the sample. A higher pump fluence was required than in the optical pump-probe measurements, in order to produce a sufficiently large pump-induced change in diffraction intensities. Fluence-dependent damage studies revealed no signs of laser-induced damage, and the measurements were repeatable over thousands of cycles.

Femtosecond electron bunches of ∼100 fs pulsewidth and 3.7 MeV kinetic energy were used to measure pump-induced changes in electron diffraction intensities.

Measurements were carried out on flakes with an average thickness of around 100 nm, exfoliated from a single crystal of $MnBi_2Te_4$ and transferred onto an amorphous Si_3N_4 membrane using an ex-situ transfer stage. The flakes were protected with an additional layer of amorphous Si_3N_4 to prevent degradation. The spot sizes of the pump and probe beams were 464 × 694 μm and ∼70 μm, respectively, and the measurements were carried out at 30 K.

The ultrafast electron diffraction intensities were obtained by averaging over several scans, normalizing individual diffraction images to account for electron beam intensity fluctuation. Individual diffraction peaks were fit to a two-dimensional Gaussian function, and then averaged over symmetry-related peaks based on the R-3m space group of $MnBi_2Te_4$.

4.5.5 Pump-probe data analysis.

The time-resolved reflectivity traces were first fitted to a product of an error function and a biexponential decay function. The error function models the excitation of photo-carriers and instrumental temporal resolution, and the exponential decay is an approximation for the sum of various unknown processes occurring over the measured time delay, including electron-electron and electron-phonon thermalization. The functional form is:

$$(1 + erf(\frac{t}{t_r}) \times (A_1 exp(-t/\tau_1) + A_2 exp(-t/\tau_2) + C)$$

Where t is the time-delay, τ_r is the rise time for the excitation of photo-carriers, τ_1 and τ_2 are the time constants of exponential decay, and A_1, A_2, and C are constants.

Upon subtracting the biexponential decay, the residual traces were fit to the sum of two decaying sinusoidal functions. The functional form is:

$$A_1 sin(2\pi f_1 t + \phi_1) exp(-t/\tau_{d1}) + A_2 sin(2\pi f_2 t + \phi_2) exp(-t/\tau_{d2})$$

where t is the time delay, f_1 and f_2 are the frequencies of the sinusoidal functionals, corresponding to the $A_{1g(1)}$ and $A_{1g(2)}$ phonons, ϕ_1 and ϕ_2 are the phases, and τ_{d1} and τ_{d2} are the time constants of exponential decay of the oscillations. The initial amplitudes A_1 and A_2 are plotted in Fig. 4d.

The ultrafast electron diffraction intensities were fit to an exponential decay function of the form:

$$A_1 exp(-t/\tau_l) + C$$

where t is the time delay, τ_l is the time constant, and A_1 and C are constants.

4.5.6 Electronic structure and phonon calculations.

DFT calculations were carried out using the Vienna Ab Initio Simulation Package (VASP) [101]–[105] with the PBE exchange correlation functional [106] and van der Waals correction via the DFT-D3 [107], [108] method with Becke-Jonson damping. A Hubbard U was also added to the Mn (4 eV) using Dudarev's [109] approach. A non-primitive cell containing two Mn atoms was used to obtain the equilibrium geometry of the system with AFM-A magnetic structure. Γ-point phonons were obtained with the finite displacement method on a 1 × 1 × 1 "supercell" using the PHONOPY software package [110] and VASP. An energy cutoff of 300 eV was used for all calculations. A 4 × 4 × 4 Γ-centered k-point mesh was used for equilibrium relaxations and phonon calculations. The general energy convergence threshold was 1×10^{-8} eV and the force convergence threshold for relaxation was 1 × 10_{-5} eV/Å. When including SOC in the magnetic parameter calculations, however, the energy convergence threshold was 1×10^{-6} eV. Gaussian smearing with a 0.02 eV width was also used in all relaxation and single-point energy calculations. Density of states calculations employed the tetrahedron method. The metallic state was modeled by electron doping the unit cells with 0.1 electron/Mn atom. Supercells for magnetic exchange calculations were generated using VESTA [111].

4.5.7 Exchange coupling constants calculations.

Magnetic exchange parameters were obtained by considering a model spin Hamiltonian of the form $H = -\sum_{<ij>} J_{ij} S_i \cdot S_j$, where J_{ij} includes intralayer exchange parameters J_1 and J_2 and interlayer exchange parameter $J^{\perp}$.A $\sqrt{2} \times \sqrt{2} \times 1$ supercell of the conventional cell was used get the intralayer exchange parameters, while a $1 \times 1 \times 2$ supercell of the primitive cell was used to get the interlayer exchange parameter. Γ-centered k- point meshes of $4 \times 4 \times 1$ and $4 \times 4 \times 4$ were used in the respective calculations. For the intralayer exchange parameters, one FM and two AFM configurations (stripe and up-up-down-down) were used. The spin exchange energy equations in terms of magnetic exchange parameters for structures of $R\bar{3}m$ symmetry are as follows:

$$E_{FM} = 3E_{NM} - 60J_1 S_i \cdot S_j - 60J_2 S_i \cdot S_j$$

$$E_{AFM1} = 3E_{NM} + 12J_1 S_i \cdot S_j + 12J_2 S_i \cdot S_j$$

$$E_{AFM2} = 3E_{NM} + 12J_1 S_i \cdot S_j - 12J_2 S_i \cdot S_j$$

For the interlayer exchange parameter, one FM and one AFM configuration were used.

$$E_{FM} = E_{NM} - 6J^{\perp} S_i \cdot S_j$$

$$E_{AFM1} = 3E_{NM} + 6J^{\perp} S_i \cdot S_j$$

The calculated values were multiplied by S^2 to obtain the exchange coupling in meV, assuming the spin of the local moment is $S = 5/2$.

4.6 Supplementary Information

4.6.1 Raman peak assignment and eigenvectors

We start with a systematic analysis of Raman phonon spectra, shown in Fig. 4.5a. The nonmagnetic unit cell contains seven atoms, and thus there are 21 phonon modes in total, consisting of 18 optical and 3 acoustic modes. Using representation theory, these can be decomposed into irreps of the point group $\bar{3}m$. Of these, only the E_g and A_{1g} modes are Raman active. Polarized Raman spectroscopy measurements are used to readily identify these modes based on their different selection rules. In particular, E_g modes have non-vanishing diagonal Raman tensor components and are thus visible under both parallel- and cross-polarized configurations, whereas the A_{1g} modes have only diagonal Raman tensor components and are visible only under the parallel-polarized configuration. We did not observe any dependence on the in-plane crystallographic orientation. First-principles calculations are used to enumerate

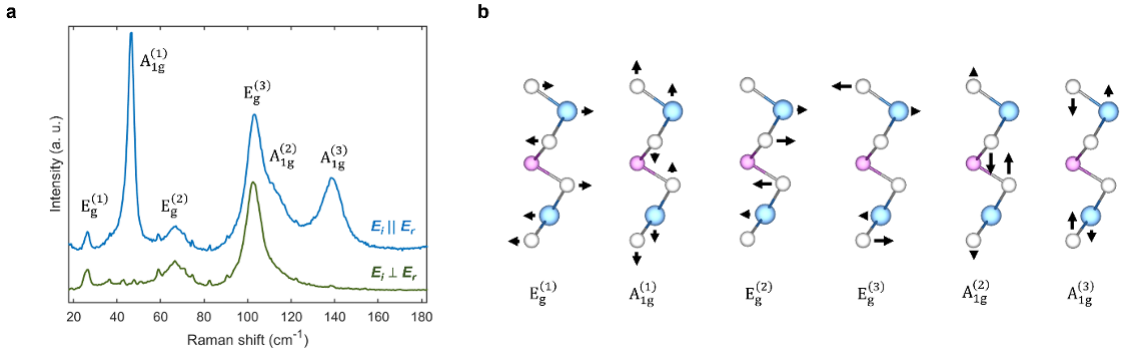

Figure 4.5: **Polarized Raman spectra.** **a**, Raman spectra with the incident and reflected beams parallel- and cross-polarized with respect to each other, at 298 K. **b**, Eigenvectors of Raman phonons, with the arrows denoting ionic motions, calculated using density functional theory simulations. The arrow lengths are proportional to the actual calculated ionic eigendisplacements for all modes.

all the Γ-point Raman-active optical phonon modes and their energies in Table 4.1. Good agreement is obtained between the calculations and measurements for all the

observed Raman phonons, confirming that the first-principles calculations provide a good description of the lattice dynamics.

Table 4.1: **Supplementary table 1. Raman phonon mode assignment.** Raman phonon symmetries and frequencies at the Γ-point, from density functional theory calculations (theory), and Raman spectroscopy (experiment) at 15 K.

Symmetry	**Frequency (cm^{-1}) (Theory, DFT)**	**Frequency (cm^{-1}) (Experiment at 15K)**
E_g	32.9	27.2
A_{1g}	50.7	49.1
E_g	79.8	69.8
E_g	112.9	108.3
A_{1g}	119.2	113.1
A_{1g}	148.9	146.6

The phonon eigendisplacements at the Γ-point, calculated using density functional theory simulations, show that A_{1g} phonons have purely out-of-plane ionic motions, whereas E_g phonons have purely in-plane ionic motions.

4.6.2 Anomalous temperature-dependence of $A_{1g}^{(1)}$ mode

In Figure 4.6a, we plot the Raman spectra measured at 15 K and 300 K, normalized to the height of the $E_g^{(3)}$ peak at ∼113 cm^{-1}, for convenience. We note that the result identified below is independent of the choice of normalization. In general, phonon peaks in Raman spectra broaden with increasing temperature due to increased phonon-phonon scattering, with resultant lower peak heights. This is visible for instance in the$A_{1g}^{(3)}$ peak at ∼145 cm^{-1}. On the other hand, the scattering intensity of the $A_{1g}^{(1)}$ mode exhibits an anomalous temperature-dependence, with a dramatic *decrease* in height and integrated intensity, with decreasing temperature

(see Supplementary Fig. 4.6b). It is apparent that this decrease in amplitude is independent of the choice of normalization. The amplitude does not show any clear correlation with the magnetic transition at $T_N = 24$ K.

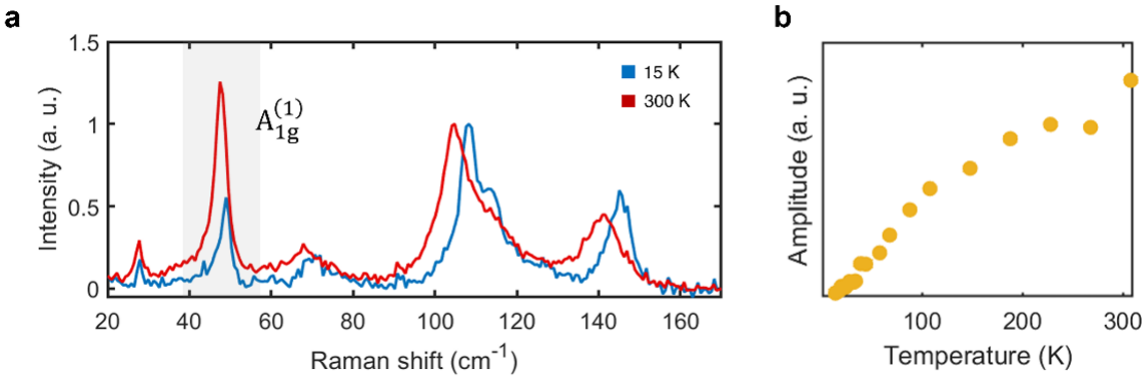

Figure 4.6: **Anomalous temperature-dependence of $A_{1g}^{(1)}$ amplitude** a, Unpolarized Raman spectra at 15K and 300K, normalized to the height of the $E_g^{(3)}$ peak at ∼115 cm^{-1}. The $A_{1g}^{(1)}$ mode is highlighted in grey. **b**, The amplitude of the $A_{1g}^{(1)}$ peak, fit to a Fano lineshape, as outlined in the Methods section.

A possible explanation for the dramatic change in scattering intensity with temperature is proximity of the Raman excitation energy (633 nm = 1.96 eV) to electronic transitions correlated with the ionic motion of the $A_{1g}^{(1)}$ mode. Optical conductivity measurements [112] indeed show large changes in the measured temperature range. Such resonant effects may be probed by measuring relative Raman phonon scattering cross-sections as a function of the excitation energy. Resonant effects are discussed in detail in Supplementary Note 5. The scattering intensity associated with the zone-boundary $A_{1g}^{(1)}$ mode is clearly visible in the field-dependent Raman spectra in Fig. 4.1e in the main text. In the temperature-dependent Raman spectra in Fig. 4.1c however, the anomalous temperature-dependence, described above, appears to swamp the small zone-boundary scattering intensity.

4.6.3 Field-dependance of $E_g^{(2)}$, $E_g^{(3)}$, and $A_{1g}^{(3)}$ spectral weights

The integrated intensities of the $E_g^{(2)}$, $E_g^{(3)}$, and $A_{1g}^{(3)}$ phonons are plotted in Figure 4.7a-c, respectively, as a function of magnetic field. The integrated intensities were obtained by fitting individual spectra following the procedure outlined in the Methods section, with the error bars denoting the standard deviation in fit values. We note a small dip in the $E_g^{(2)}$ intensity at the spin-flop critical field of 3.7 T. Outside of this, the three modes shown here exhibit no clear field-dependent behavior above the experimental and fitting uncertainty. In particular, there is no signature of coupling to the antiferromagnetic order parameter and the associated zone-boundary phonons.

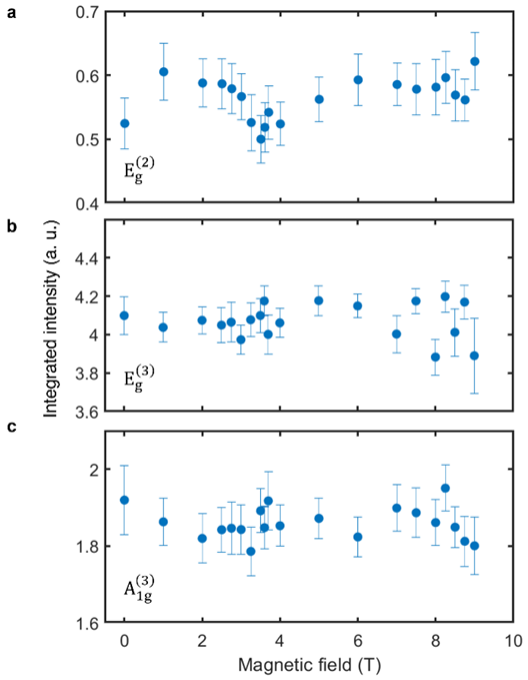

Figure 4.7: **Absence of magnetophononic coupling.** The panels show spectral weights of the **a**, $E_g^{(2)}$, **b**, $E_g^{(3)}$, and **c**, $A_{1g}^{(2)}$ modes respectively, as a function of magnetic field. The error bars are standard deviations of the fit values.

4.6.4 Generalized magnetophononic coupling and frequency renormalization

We write down minimal lattice and spin Hamiltonians[113] to describe a generalized magnetophononic coupling. Consider the lattice Hamiltonian described by the harmonic approximation,

$$H_L = H_L^0 + \frac{1}{2!}\frac{\partial^2 H_L^0}{\partial u_\alpha^2}u_\alpha^2 + \mathcal{O}(u_\alpha^3) \approx H_L^0 + \frac{1}{2}N\mu_\alpha\nu_\alpha^{0^2}u_\alpha^2, \tag{4.3}$$

Where u_α is the displacement along the phonon normal mode α, μ_α is the reduced mass, ν_α is the frequency, and N is the number of unit cells. The magnetic ground state energy described by a Heisenberg-like Hamiltonian,

$$H_m^0 = -\sum_{ij} J_{ij} S_i \cdot S_j \tag{4.4}$$

where i and j are spin site indices, and J_{ij} is the isotropic exchange interaction between spins at i and j. When this is perturbed by a zone-center optical phonon α, the perturbed magnetic energy can be derived by considering the derivatives of J_{ij} with respect to the phonon normal mode displacement u_α. Expanding up to second order in u_α , the perturbed exchange interaction is

$$J'_{ij}(u_\alpha) = J_{ij} + \frac{\partial J_{ij}}{\partial u_\alpha}u_\alpha + \frac{1}{2}\frac{\partial^2 J_{ij}}{\partial u_\alpha^2}u_\alpha^2 \tag{4.5}$$

Here, the first order term, in the specific case of J=$J^\perp$ is responsible for the magnetophononic wave-mixing described in detail in the main text (Eq. 4.3 and 4.4). The second order term, proportional to u_α^2, renormalizes the harmonic term in the lattice energy, resulting in spin-induced phonon frequency changes. Separating the in-plane and out-of-plane exchange couplings, denoted by J_μ and $J_\mu^\perp$, respectively, where μ = 1 ,2, ... are the first- and second-nearest-neighbors and so on, and assuming small spin-induced energy shifts i. e. $\nu_\alpha + \nu_{\alpha 0} \approx 2\nu_\alpha$, the renormalized phonon frequency is given by

$$\nu_\alpha - \nu_{\alpha 0} = \frac{1}{4N\mu_\alpha\nu_{\alpha 0}}[\sum_\mu \frac{\partial^2 J_\mu}{\partial u_\alpha^2} \sum_i S_i \cdot S_{i+\mu} + \sum_\mu \frac{\partial^2 J_\mu^\partial}{\partial u_\alpha^2} \sum_i S_i \cdot S_{i+\mu^\perp}]. \quad (4.6)$$

The above expression shows the renormalization of the phonon frequency due to spin order along different directions, through the respective exchange couplings. Under a mean-field approximation, Eq. 4.6 simplifies to $\nu_\alpha - \nu_{\alpha 0} \propto < S^2 >$. Experimentally, we observe such a spin-induced phonon frequency renormalization in the $A_{1g}{}^{(1)}$ mode. The phonon frequencies are first extracted as a function of temperature, using the fitting procedure outlined in the Methods section of the main text. We then account for phonon-phonon interactions by fitting the temperature-dependent phonon frequencies to that of a (cubic) anharmonic phonon, given by $\omega(T) = \omega_0 + A(1 + \frac{2}{e^{\hbar\omega_0/2k_BT}-1})$, where ω is the phonon frequency renormalized by anharmonic (phonon-phonon) interactions, T is the temperature, ω_0 is the bare phonon frequency, and A is the mode-specific fitting constant.

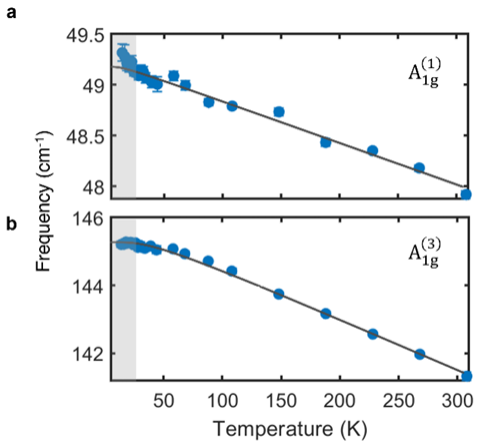

Figure 4.8: **Spin-induced phonon frequency renormalization.** Temperature-dependent frequency of the $A_{1g}{}^{(1)}$ phonon mode **a,** and $_{1g}{}^{(3)}$ phonon mode **b,**. The black lines are fits to the anharmonic phonon model described in the text. Error bars are standard deviations in fit values.

Fig. 4.8 shows the temperature-dependent frequency of the $A_{1g}{}^{(1)}$ mode, with the black line 5 showing a fit to the anharmonic phonon model. The plot

shows a small but clear deviation from the fit below $T_N = 24$ K, indicating a spin-induced phonon frequency renormalization. In contrast, the temperature-dependent frequency of the $A_{1g}{}^{(3)}$ mode in Fig. 4.8 shows good agreement with the anharmonic phonon model down to the lowest temperatures, indicating that the $A_{1g}{}^{(3)}$ mode does not exhibit a significant spin-induced frequency renormalization.

Interestingly, we note that a previous study [76] on atomically thin flakes of $MnBi_2Te_4$ reported a negative spin-induced frequency renormalization of the $A_{1g}{}^{(1)}$ mode, contrary to the positive frequency renormalization observed in the bulk crystals used in our study. This difference may possibly be due to changes in the electronic and magnetic structure as a function of sample thickness in the 2D limit.

The strong magnetophononic coupling observed in the $A_{1g}{}^{(2)}$ mode in our magneto-Raman measurements suggests that it too might exhibit a significant spin-induced frequency shift. Unfortunately, the spectral overlap between the $A_{1g}{}^{(2)}$ and $E_g{}^{(3)}$ modes (see Fig. 4.5a) and strong $A_{1g}{}^{(2)}$ zone-boundary scattering intensity below T_N hinders a similar temperature-dependent frequency analysis for the $A_{1g}{}^{(2)}$ mode. None of the other observed Raman phonons exhibit a spin-induced frequency renormalization above the experimental uncertainty.

4.6.5 Resonant Raman effects

Resonant Raman effects may potentially give rise to temperature- and field-dependent artifacts in phonon peak intensities due to changes in the electronic band structure across phase transitions. In order to rule out such an explanation for the phenomena reported in Fig. 4.1 and Fig. 4.2, we investigate resonant Raman effects in $MnBi_2Te_4$ by measuring phonon spectra at different laser excitation energies. In Fig. 4.9, we show the Raman phonon spectra measured with laser excitation energies of 1.58 eV (785 nm), 1.96 eV (633 nm), and 2.71 eV (458 nm), at 297 K and zero magnetic field. Note that the 1.58 eV Raman spectrum is only shown down to 65

cm^{-1} due to the limitation of our low-frequency filters at this excitation wavelength.

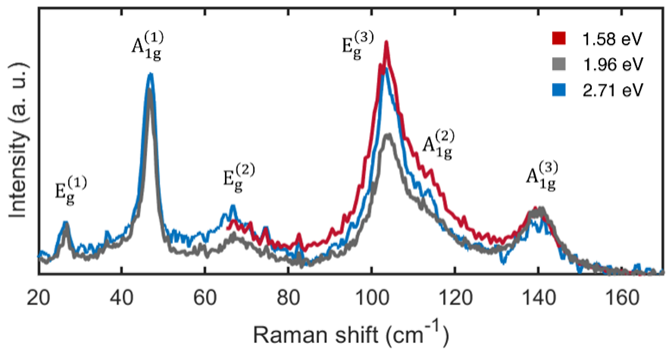

Figure 4.9: **Phonon spectra at different laser excitation energies.** Raman phonon spectra measured using 1.58 eV (785 nm), 1.96 eV (633 nm), and 2.71 eV (458 nm) laser excitation energies at 297 K and zero magnetic field. Spectra are normalized to the $A_{1g}{}^{(3)}$ peak intensity.

It is observed that phonon peak intensities indeed change as a function of the laser excitation energy, however, these changes occur across all the observed phonon modes, i. e. the three A_{1g} modes as well as the three E_g modes. It is clear that this result is independent of the choice of normalization. In contrast, the temperature- and field-dependent magnetophononic effects observed in our study are only in the $A_{1g}{}^{(1)}$ and $A_{1g}{}^{(2)}$ modes, with negligible changes in the scattering intensities of other modes. Our observations reported in Fig. 4.1 and Fig. 4.2 are thus inconsistent with resonant Raman effects.

Furthermore, upon tracking the $A_{1g}{}^{(2)}$ mode across the PM $\rightarrow$ AFM transition at 24 K using the 1.58 eV (785 nm) laser excitation, it is found that the Raman scattering intensity exhibits quantitatively the same behavior (see Fig. 4.10) as with the 1.96 eV (633 nm) laser excitation (see Fig. 4.1c) – i. e. the $A_{1g(2)}$ scattering intensity is enhanced by around 35% in the AFM phase. This is additional evidence that the observed phenomenon is inconsistent with resonant Raman effects, wherein different excitation energies would give rise to qualitatively different temperature-dependent intensity changes. It is instead consistent with an effect arising from the

AFM order, as in our model of magnetophononic wavemixing.

It is useful to consider the exchange energies involved in various magnetic phase transitions in $MnBi_2Te_4$. The dominant in-plane nearest neighbor exchange coupling is 0.12 meV, whereas the interplanar exchange coupling is an order-of-magnitude weaker [114]. The temperature-driven PM $\rightarrow$ AFM transition is accompanied by significant magnetic energy changes due to the in-plane ordering of spins, and the large in-plane exchange coupling. On the other hand, the in-plane ordering remains unchanged in the out-of-plane magnetic field-driven AFM $\rightarrow$ FM transition, with only the interplanar magnetic order being modulated.

The accompanying magnetic energy changes are thus an order of magnitude weaker than in the PM $\rightarrow$ AFM transition. Hence it is expected that the associated electronic structure changes as a function of out-of-plane magnetic field would also be correspondingly small, minimizing artifacts due to resonant Raman effects. This assertion is validated in our work, where we find that the scattering intensities of the E_g modes and the ${A_{1g}}^{(3)}$ mode are unchanged as a function of out-of-plane magnetic field within the experimental uncertainty, as outlined in Section 4.6.3, allowing us to identify magnetophononic zone-folding in the ${A_{1g}}^{(1)}$ and ${A_{1g}}^{(2)}$ peaks. Importantly, the phenomena observed in Fig. 4.1 and Fig. 4.2 are correlated not with magnetic order itself, but specifically with AFM order. The zone-boundary phonon intensity vanishes in the FM phase. In fact, as the results in Fig. 4.2 show, the zone-boundary intensity of the ${A_{1g}}^{(2)}$ phonon quantitatively tracks the AFM order in both the temperature- and magnetic field-dependent experiments.

Based on the above arguments, in order to rule out resonant Raman effects and isolate peak intensity changes due to magnetophononic coupling, it is essential to measure and analyze phonon scattering intensities as a function of both temperature and magnetic field, as carried out in the present work.

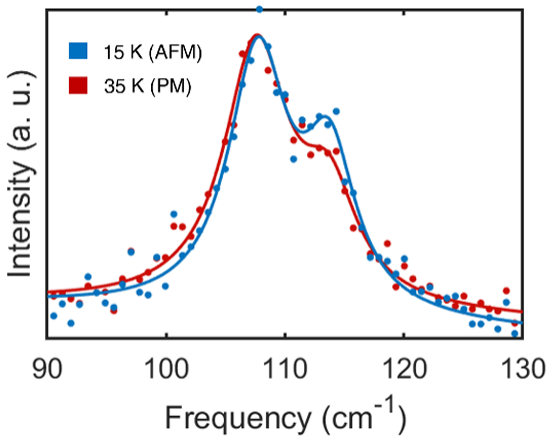

Figure 4.10: **Temperature-dependent intensity of $A_{1g}^{(2)}$ mode with 1.58 eV excitation.** Raman spectra measured at 15 K and 35 K using a 1.58 eV (785 nm) laser excitation. The dots are experimental datapoints, and the solid lines are fits as outlined in the Methods section.

4.6.6 Symmetry of anomalous scattering intensity

Magnetic ordering can potentially give rise to one-magnon and two-magnon resonances in Raman spectra. In order to eliminate the possibility that the anomalous scattering intensities observed in our work (plotted in Fig. 4.1 and Fig. 4.2) are due to magnons, we carry out a polarization analysis.

Magnons, by virtue of breaking time-reversal symmetry necessarily have off-diagonal terms in the Raman tensor [115]. In $MnBi_2Te_4$, this is associated with E_g modes, as opposed to A_{1g} modes which are fully symmetric and have only diagonal components. The symmetry associated with Raman scattering intensity can be identified as A_{1g} or E_g using polarized Raman measurements, as in Supplementary Note 1. Here, we focus on the $A_{1g}^{(2)}$ mode. In Fig. 4.11, we show Raman spectra obtained below and above the AFM ordering temperature $T_N = 24$ K, corresponding to parallel-polarization, which is sensitive to both A_{1g} and E_g modes, and cross-polarization, which is sensitive only to E_g modes. Our results clearly show that the anomalous scattering intensity overlapped with the $A_{1g}^{(2)}$ phonon in the AFM

phase has an A_{1g} symmetry, since it is absent in the cross-polarized channel. This rules out the possibility that it is due to a magnon. It is instead consistent with our interpretation in terms of scattering intensity due to $A_{1g}^{(2)}$ zone-boundary phonons.

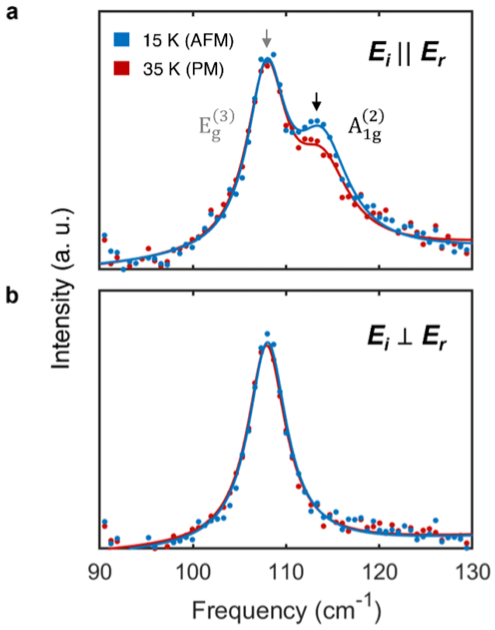

Figure 4.11: **Temperature- and polarization-dependent $A_{1g}^{(2)}$ scattering intensity.** Raman spectra 17 measured at 15 K and 35 K with parallel- (**a**) and cross-polarization (**b**) of incident and reflected light. The dots are 18 experimental datapoints, and solid lines are fits as outlined in the Methods section.

The above inference is also consistent with magnon dispersions measured using inelastic neutron scattering [114]. The dispersion shows that zone-center magnons are at around 1 meV ($\sim$8 cm^{-1}), whereas the highest energy zone-boundary magnons are at 3 meV ($\sim$25 cm^{-1}). The low energy of zone-center magnons rules out the possibility of one-magnon resonance interfering with phonon peaks. A two-magnon resonance may plausibly interfere with the $A_{1g}^{(1)}$ mode at 47 cm^{-1} but would be too low in energy to affect the $A_{1g}^{(2)}$ mode at 115 cm^{-1}, ruling it out as an explanation for the observed phenomena. Two-magnons are also typically associated with a broad continuum of excitations rather than a well-defined peak, a feature that we do not

observe in our experiments.

Pump-probe measurements-Fluence-dependence

The pump-probe measurements outlined in the main text show phonon excitation via a displacive mechanism, where the ultrafast excitation of carriers by the pump pulse shifts the quasiequilibrium ionic coordinates, generating coherent phonons. Here, the amplitude of coherent phonons is directly proportional to the pump-induced carrier density, i. e. the absorbed fluence. In this context, field-dependent optical conductivity changes may influence coherent phonon amplitudes, in addition to the magnetophononic coupling highlighted in the main text. We account for such magnetic-field dependent changes in absorbed fluence by normalizing the pump-probe measurements with respect to the pump-induced carrier density. The carrier density can be tracked by the maximum amplitude of the transient reflectivity trace, which occurs at a time delay of $\sim$0.9 ps. In Fig. 4.4 of the main text, all the pump-probe traces are normalized with respect to this amplitude.

We verify the validity of this approach by separately measuring the transient reflectivity and coherent phonon amplitudes as a function of pump fluence, shown in Fig. 4.12a. The fits in Fig. 4.12b and 4.12c, carried out as outlined in the Methods, show that both the maximum transient reflectivity (which tracks the absorbed fluence and photoinduced carrier density) as well as the unnormalized coherent phonon amplitudes scale linearly with fluence, confirming that the maximum amplitude of the transient reflectivity trace indeed tracks the carrier density, validating the normalization procedure used in the main text.

Finally, we note that outside of magnetic-field dependent changes in absorbed fluence, there may potentially be additional magnetodielectric effects that change the electron-phonon interactions and thus the Raman susceptibility, which can affect coherent phonon generation. To lowest order, such changes may be phenomenologically described by a magnetodielectric effect of the form $\chi_e = \chi_e^{(0)} + \gamma M^2$, where χ_e is the

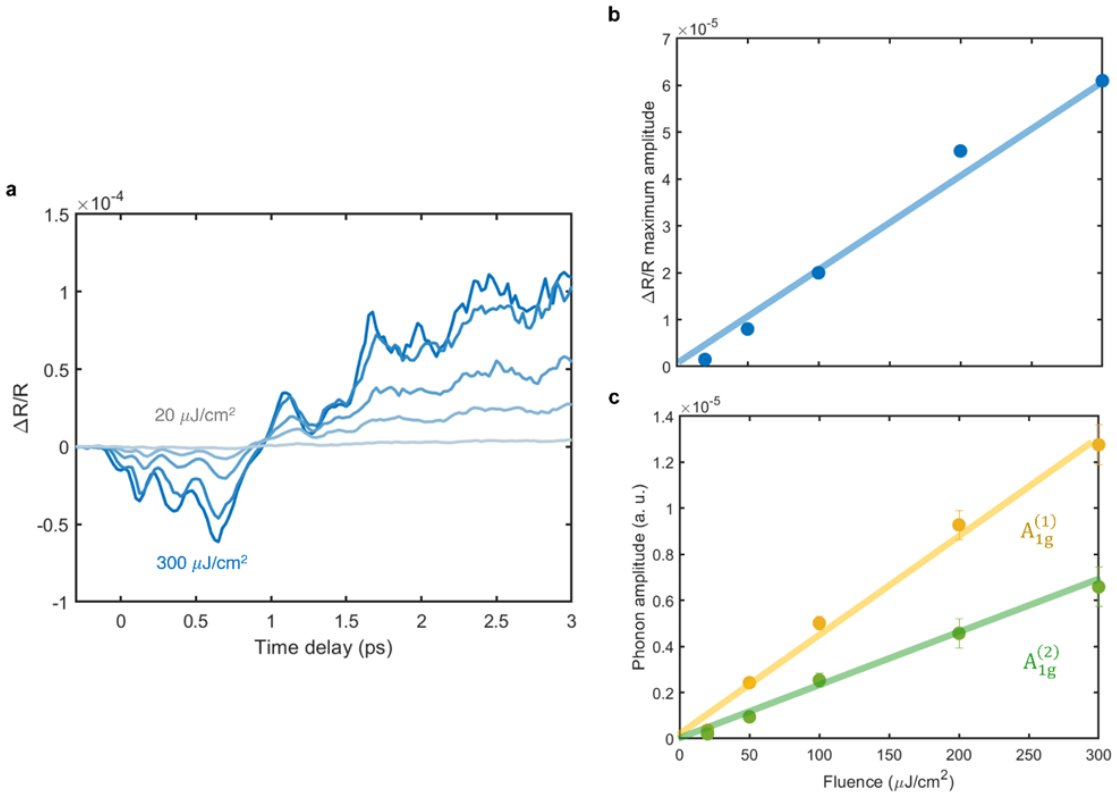

Figure 4.12: **Fluence-dependence of coherent phonons.** **a,** Transient reflectivity traces as a function of pump fluence from 20 to 300 $\mu J/cm^2$. **b,** Maximum sub-picosecond amplitude of transient reflectivity as a function of pump fluence, which is a measure of the photoinduced carrier density. **c,** Amplitude of $A_{1g}{}^{(1)}$ and $A_{1g}{}^{(1)}$ coherent phonons as a function of pump fluence, extracted using the method outlined in the main text and Methods. The lines in b and c are linear fits. Error bars are standard deviations in fit values.

electrical susceptibility, γ is magnetodielectric coefficient, and M is the net magnetization. Below, we explore possible changes to electron-phonon interaction due to such a magnetodielectric effect. In the interest of conceptual clarity, we consider a simple $M-H$ dependence $M = \chi_m H$, where χ_m is the magnetic susceptibility and H is the external magnetic field, the Raman susceptibility of a phonon (which determines the coherent phonon amplitude via a Raman-like displacive excitation) can then be written as $\frac{d\chi_e}{du} = \frac{d\chi_e^{(0)}}{du} + H^2(2\gamma\chi_m\frac{d\chi_m}{du} + \chi_m^2\frac{d\gamma}{du})$. The expression in parenthesis determines

the change in Raman susceptibility due to the magnetic field, where $\frac{d\chi_m}{du}$ and $\frac{d\gamma}{du}$ are the phonon modulation of the magnetic susceptibility and magnetodielectric coupling coefficient, respectively. Such a field-dependent change in the coherent phonon amplitude would then be a form of indirect magnetophononic coupling. Based on our current pump-probe experimental data, we cannot completely rule out that such indirect magnetophononic effects also have a contribution, in addition to the direct magnetophononic effects highlighted in our manuscript.

4.6.7 Debye-Waller effect in ultrafast electron diffraction

Optical pump-probe experiments are typically initiated by ultrafast optical (pump) pulses which generate photo-excited carriers (electrons and holes) - which, after thermalizing, decay through the generation of lattice (and spin) excitations. The lattice excitations result in a disordering of the lattice. Ultrafast electron diffraction is a direct probe of this pump-induced lattice disorder, through the transient Debye-Waller effect.

In general, the intensity of a Bragg reflection in an electron diffraction experiment is given by

$$I_0(Q) = \sum_j f_j(Q) exp(-2\pi^2 B_j Q^2) exp(-i2\pi Q \cdot r_j) \tag{4.7}$$

where the summation is over atoms in the unit cell (indexed by j), Q is the scattering wavevector, f_j is the atomic structure factor for electron diffraction for atom j, B_j is the isotropic Debye-Waller factor for atom j, and r_j is the position of atom j in the unit cell. The Debye-Waller factor is given by $B_j =< u_j^2 >$, which is the root-mean-square displacement of atom j about its mean position. A representative static diffraction pattern from a ∼100 nm flake of $MnBi_2Te_4$ oriented along the (0 0 1) crystallographic direction is shown in Fig. 4.13a.

Pump-induced lattice disorder increases B_j, i. e. $B_j \rightarrow B_j + \Delta B_j$, thus generally resulting in a decrease in the transient Bragg reflection intensities. We can

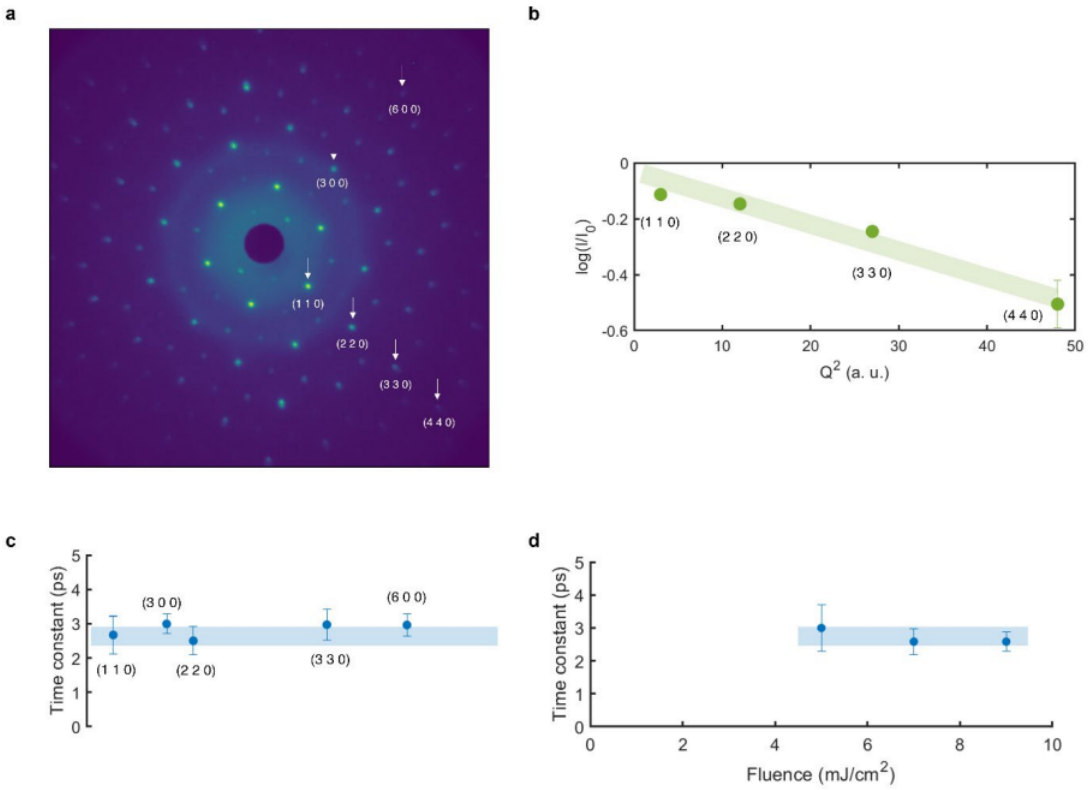

Figure 4.13: **Transient Debye-Waller effect. a,**, Static electron diffraction image, with the (n n 0) family of peaks labeled. **b,** Transient Bragg reflection intensity obtained in the $t \to \infty$ limit from the exponential decay fit, plotted as a function of **Q**. The green line is a guide to the eye. **c,** The exponential decay constant of the transient intensity of various Bragg peaks. **d,** The exponential decay constant of the (2 2 0) peak as a function of pump fluence. Error bars are standard deviations of fit values. The blue lines are guides to the eye.

define an effective transient Debye-Waller factor ΔB_{eff} as follows

$$\begin{aligned} I(Q) &= \sum_j f_j(Q) exp(-2\pi^2(B_j + \Delta B_j)Q^2) exp(-i2\pi Q \cdot r_j) \\ &= exp(-2\pi^2 \Delta B_j Q^2) I_0(Q) \end{aligned} \tag{4.8}$$

The transient Bragg reflection intensity $I(Q)$ is thus a quantitative measure of the pump-induced lattice disorder, $\Delta B_{eff} = \Delta < u^2_{eff} >$. The Debye-Waller effect for a given family of Bragg reflections scales with Q, such that $log(\frac{I}{I_0}) \propto -Q^2$.

In Fig 4.13b, we plot the transient intensity $log(\frac{I}{I_0})$ of the (n n 0) family of Bragg reflections at the $t \to \infty$ limit from the exponential decay fit (see Methods), as a function of Q^2. The linear dependence confirms that the observed evolution of transient Bragg intensities is due to a Debye-Waller effect via pump-induced lattice disorder.

The time constants of the transient intensities of various Bragg peaks, obtained from exponential decay fits, are shown in Fig. 4.13c. Within the experimental uncertainty, the time constant is uniform across different peaks.

In the main text, we use the transient Debye-Waller time constant from our UED measurements to establish the timescale of lattice thermalization. However, the optical pump-probe measurements reported in the main text use a much lower fluence, of 0.1 mJ/cm^2, as opposed to 7 mJ/cm^2 used in the UED measurements reported above. In this context, we report the thermalization time constants from our UED measurements as a function of fluence, in Fig. 4.13d. The time constants are largely unchanged from 5 to 9 mJ/cm^2, with a slight increase at lower fluences.

Such a behavior is consistent with increased phonon-phonon scattering at higher fluences [116]. It is expected then that the thermalization time constant at the low fluences used in our optical measurements, with their correspondingly lower phonon populations, would likely be even higher than that extracted from the UED measurements; i. e. the UED time constant sets a lower bound for the phonon thermalization time. This supports our assertion that phonon subsystem remains in a nonequilibrium state through the entire time delay range measured in our study.

4.7 Acknowledgments

Chapter 4, in full, is a reprint of the material as it appears in Nature Communications 2022. Hari Padmanabhan, Maxwell Poore, Peter K. Kim, Nathan Z. Koocher, Vladimir A. Stoica, Danilo Puggioni, Huaiyu (Hugo) Wang, Xiaozhe Shen,

Alexander H. Reid, Mingqiang Gu, Maxwell Wetherington, Seng Huat Lee, Richard D. Schaller, Zhiqiang Mao, Aaron M. Lindenberg, Xijie Wang, James M. Rondinelli, Richard D. Averitt, and Venkatraman Gopalan. The dissertation author shared the role of primary investigator and author with Hari Padmanabhan and Peter K. Kim.

Chapter 5

Spin precession and magnetization dynamics in bulk $MnBi_2Te_4$

5.1 Abstract

We investigate spin precession and magnetization dynamics in the first intrinsic magnetic topological insulator $MnBi_2Te_4$ using time-resolved MOKE (TR-MOKE) techniques. Clear indications of magnetic phase transitions are observed in our time-resolved data, as well as detailed information on the magnetic ground state present in the ultrafast demagnetization data. In the canted-AFM (c-AFM) phase, magnetic oscillations of a few GHz appear. The frequency trend with the out-of-plane external magnetic field points toward the oscillations originating from an acoustic k=0 magnon which is gapped out due to some additional U(1) symmetry breaking term. A theoretical model is developed which identifies the misalignment between magnetic field and c-axis as the leading mechanism for magnon gap. The c-AFM to FM transition as inferred from the sharp change in magnon frequency trend obtained from TR-MOKE data takes place at a lower magnetic field than the c-AMF-FM transition seen in equilibrium measurements.

5.2 introduction

Magnetic 2D materials have seen an explosion of interest in recent years, providing intriguing and versatile platforms for theorists and experimentalists to explore novel low-dimensional magnetism while potentially enabling real-world applications including magnetic memory storage and quantum computing [117], [118]. These materials host a variety of exotic magnetic phenomena and phases. This includes the Quantum Anomalous Hall Effect (QAHE), axionic and Chern insulating phases, proximate spin liquid ground states, and layer-dependent magnetism [22], [25], [27], [36], [44], [46], [119]–[122]. Additionally, van der Waals (vdW) magnets can be exfoliated down to the monolayer limit, which permits layer control of MBT and enables engineering layered 2D heterostructures [123].

In stride with the goal of characterizing these new and exciting materials is the goal of controlling their macroscopic properties. Light is a useful tool on both fronts providing novel routes for mode-selective excitation and probing of quantum materials. One of the most exciting examples of light-based control in quantum materials was seen in the time-resolved ARPES measurements on the topological insulator Bi_2Se_3. Using Mid-IR light hybridization between between the surface states and photons were seen in the form of Floquet-Bloch states appearing after excitation [124], [125]. In the optical and near-IR light has the ability to drive electronic interband transitions. Moreover, with short pulse excitation the abrupt introduction of excited charges in a sample causes ultrafast modification to the crystal lattice, orbital, and spin degrees of freedom [126], [127]. For example, recent studies [92] have shown mid-IR optically-driven phonons in $DyFeO_3$ cause an ultrafast non-thermal spin reorientation which takes the system from an AFM to a weakly ferromagnetic (WFM) magnetic configuration, proving the utility of optics in driving macroscopic phase transitions which change the magnetic state and symmetry of the system. In 2D systems like $MoTe_2$, photoexcitation can change the electron density in the

material which ultimately causes a structural transition leading to nontrivial band topology, highlighting the usefulness of photoexcitation in controlling 2D and topological materials [128].

In recent years, $MnBi_2Te_4$ (MBT) has garnered great interest in the condensed matter community. An intrinsic magnetic topological insulator (TI), MBT overcomes the issue of extremely low ordering temperatures that is prevalent in other materials [13], [14], [18], [129]. MBT is a van der Waals (vdW) magnet, which orders into an A-type antiferromagnet at a Néel temperature of T_N=24K. As a function of temperature and magnetic field, MBT also experiences canted-AFM (c-AFM), paramagnetic (PM), and field-induced ferromagnetic (FM) states (see Fig. 5.1a) [22]–[24], [44]. There are reports of the quantum anomalous Hall effect (QAHE) and axionic insulator states for odd and even number of layers MBT, respectively [22], [25], [27], [46], [119]. Additionally there are reports of a C=1 Chern insulator phase in MBT when it is in the c-AFM phase, indicating nontrivial topology [27], [36], [44]. These results indicate a link between the magnetic phases and the topology, suggesting the possibility of inducing concomitant magnetic and topological transitions in MBT. Recent magneto-Raman and ultrafast pump-probe spectroscopy measurements reveal that the interlayer exchange is coupled to optical phonons [130]. Theoretical work indicates that intense laser pulses in resonance with phonons in MBT lead to sign changes in the interlayer exchange interactions accompanied by topological band transitions [99], while circularly polarized light in the eV range could induce Chern number changes in MBT [131] and related heterostructures [132]. As topology and magnetism are intertwined, MBT is a prime candidate for magnetic topological control. One route to accomplish this is with optics. Therefore it is imperative to understand photoexcited magnetization dynamics in MBT with a view towards topological control.

In this chapter we focus on magnetic spin precession in bulk MBT. The precession is observed in the c-AFM phase detected using time-resolved magneto-

optical Kerr effect (TR-MOKE) in the polar Kerr geometry. We investigate how the precession dynamics evolve with external magnetic field, temperature, and fluence. The collective spin excitations of the magnetic phases of MBT have been reported for few-layer MBT samples studied via Raman scattering [133], and two-color pump-probe reflectivity and MOKE measurements in the presence of an in-plane magnetic field [60]. In our work, MBT demagnetization dynamics will also be highlighted, as they offer a clear indication of magnetic phase transitions and help in describing the microscopic physics of what happens to the complex magnetic system after an optical pump pulse arrives. By thoroughly investigating the magnetization dynamics and spin precession, we will demonstrate that MBT is an intriguing material not just for its topological characteristics but also for its rich magnetic properties and its sensitivity to optical perturbation.

5.3 Methods

5.3.1 Experimental set up

In this study, we performed time-resolved MOKE (TR-MOKE) on bulk single-crystal MBT as a function of magnetic field, temperature, and fluence. The pump beam was centered around 850 nm (1.46 eV) and compressed to approximately 50 fs with an FWHM diameter of 92 μm on the sample surface. The output from our Spirit laser (Spirit-1040-8) was used as the probe beam, centered at 1040 nm (1.19 eV) with a pulse duration of 350 fs and FWHM diameter of around 52 μm. The penetration depth of our pump is 49nm, or around 12 septuple layers (SL). For the pump, a fluence of 20 $\mu J/cm^2$ was used for all data unless specified otherwise, the probe was set to a fluence of 10 $\mu J/cm^2$. After reflecting off the sample a pick-off mirror directs the probe beam into the detection scheme. Lenses and long pass filters shape the beam and get rid of pump scatter to improve the signal to noise,

respectively. A half waveplate, Wollaston prism, and balanced photodiode detector are used to perform the MOKE measurements (See Chapter 3 for more information).

5.3.2 Data analysis

In general, the dynamics of the TR-MOKE data can be categorized by the fast demagnetization ($\sim$ 1 ps), the slower demagnetizations (70 ps and 400 ps), and in the c-AFM phase, oscillations of the Mn spins ($\sim$ 100 ps). Since our probe energy is around 1.2 eV, the experiment is sensitive to the Bi and Te p-like spins, whereas the localized Mn d spins are $\sim$ 4 eV below the Fermi energy [134]. Despite this, due to a large J_{pd} coupling (coupling of the itinerant p spins to the localized Mn d spins) the p-like spins reflect the dynamics of Mn d spins at longer timescales. In the first 10ps a fast demagnetization process occurs, with a characteristic timescale of around a picosecond. This process is attributed to ultrafast demagnetization of the p-like Bi/Te bands due to electron-optical phonon scattering where the phonons provide the momentum to cause a spin-flip in these itinerant bands [134]. This demagnetization process is fit to a minimal single exponential rise: $A_f(1 - e^{-}t/tf) + C_f$. $\mathrm{A_F}$ and $\mathrm{t_f}$ are the amplitude and rise time of the ultrafast demagnetization, while $\mathrm{C_f}$ is an offset. The demagnetization process with the longer timescale can be attributed to spin-lattice thermalization of the Mn spins ($\sim$ 400 ps). There is an intermediate timescale ($\sim$ 70 ps) which comes from the J_{pd} term mentioned earlier, this process corresponds to the localized Mn d spins reacting to the ultrafast demagnetization of the itinerant p-like spins through J_{pd} coupling. This 70 ps demagnetization timescale is clearly seen at higher fluences, where there is more ultrafast demagnetization of the p-like spins to drive the J_{pd} driven demagnetization dynamics. Since most of the data was taken at lower fluences where this intermediate timescale demagnetization is less apparent, the data can be fit by just using one slow timescale. For more information on the J_{pd} demagnetization see supplemental note 4. The spin precession and slow

demagnetization data was fit from 10-1000 ps, leaving out the ultrafast electron-optical phonon mediated demagnetization process and focusing on the localized Mn spins. To fit the spin precession data, the exponential demagnetization signal was fit with $(A_1 - A_2 * e^{-t/t_1})e^{-t/t_2} + C_1$ and the residual damped oscillation was fit with $A_3 \sin(\omega t)e^{-t/t_3} + C_2$. Here, A_3 represents the amplitude of the spin precession, ω the frequency, and t_3 is the decay time constant of the precession, which can be used to find the Gilbert damping parameter α by $\alpha = \frac{1}{\omega t_3}$.

5.4 Results

5.4.1 Ultrafast optical and magneto-optical response of MBT

Before discussing the spin precession and slow demagnetization dynamics it is important to understand the response of the charge, lattice, and spin degrees of freedom in the ultrafast regime. In Fig. 5.1b, from time-resolved reflectivity there are clearly two oscillations that are launched by the pump, riding on top of an ultrafast carrier relaxation peak. The oscillations correspond to the fully symmetric $A_{1g}^{(1)}$ and $A_{1g}^{(2)}$ phonon modes, with frequencies of 1.5 THz and 3.4 THz, respectively (see Fig. 5.1c)[76], [99], [130], [135], [136]. In Fig. 5.1d we see the full tr-MOKE response to the pump, with the initial ultrafast demagnetization followed by a ∼6 GHz oscillation on top of a slower exponential demagnetization. This oscillation emerges in our data as we go from the AFM to the c-AFM phase. The oscillating dynamics will be the main focus of this work. To clearly demonstrate the ultrafast demagnetization Fig. 5.1e shows the first 10 ps of Fig. 5.1d. This ultrafast demagnetization was explained in a previous work [134] as Elliott-Yafet demagnetization where itinerant spins scatter off of optical phonons launched by the pump. This results in a spin flip and thus an overall demagnetization of itinerant carriers on ultra-fast timescales.

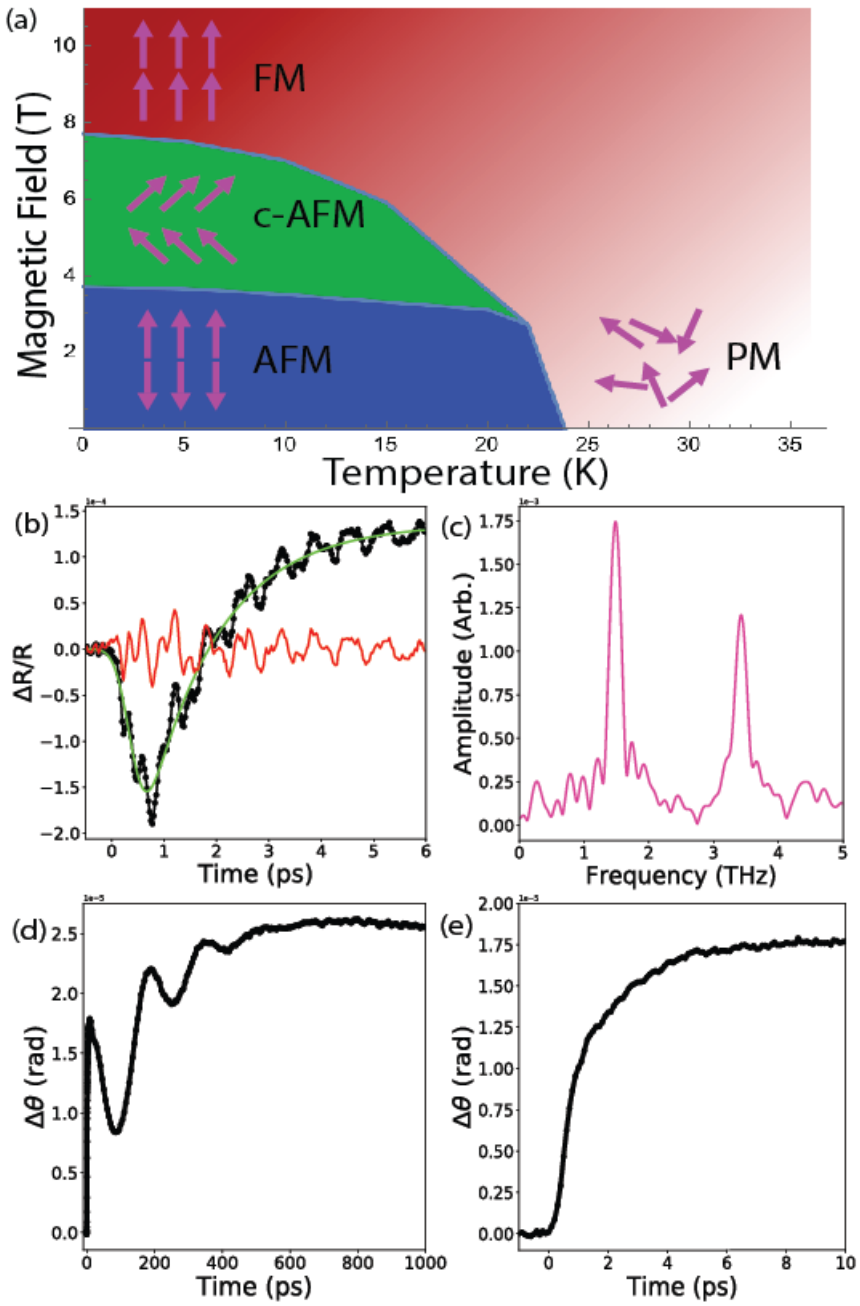

Figure 5.1: **Crystal structure and ultrafast response**: **a.** Temperature vs. field applied along the c-axis phase diagram adapted from [22]. **b.** The ultrafast dR/R signal from MBT, shown with a fit in green and the residual in red. The data was taken at 2 K, 3.8 T, with a pump fluence of 100 $\mu J/cm^2$. **c.** FFT of the residual from **b.**, the peak at 1.5 THz corresponds to the $A_{1g}{}^{(1)}$ phonon and the peak at 3.4 THz corresponds to the $A_{1g}{}^{(2)}$ phonon. **d.** Time-resolved MOKE scan, data collected at 2 K, 3.8 T, with a pump fluence of 20 $\mu J/cm^2$. **e.** First 10 ps of the data in **d**.

5.4.2 Temperature dependence of spin precession

At a field of 3.8 T, a temperature sweep was performed to investigate how the spin precession evolves (Fig. 5.2a). The ultrafast demagnetization amplitudes are plotted in Fig.5.2b. The amplitudes reflect the equilibrium magnetization as seen in other studies [23], [24], with $T_N \sim 20$ K, confirming that TR-MOKE is a sensitive probe of the magnetization in MBT. The dip in amplitude around 10 K however was not observed in the previous studies. This may be due to the fact that in [23], [24] magnetization was measured directly with SQUID magnetometry. The dip at 10 K in Fig.5.2b may be due to changes in the optical properties of the material, or a change in the population of phonons which cause the ultrafast demagnetizaiton. Interestingly, the spin precession amplitude in Fig. 5.2d seems to be affected by the lower than expected ultrafast demagnetization amplitude at 10K as well. This points toward the ultrafast demagnetization in MBT affecting the precessional amplitude seen at later times. Further studies are needed to understand this feature. As the temperature is increased from 2 K to 30 K the spin precession displays a clear trend where the frequency and amplitude decrease. This is illustrated in Fig.5.2c,d, where the frequency follows an order parameter-like decrease upon approaching T_N (at 3.8 T, $T_N \sim 20$ K) [23], [24], marking the transition from c-AFM to PM. The decay times and Gilbert damping of the precession as a function of temperature are in Supplemental note 3. Fig.5.2a. shows a distinct difference in the response for MBT in the c-AFM vs. the PM state under these experimental conditions. Most notably, as the temperature is increased the response transforms from a spin precession on top of an exponential background (c-AFM) to a purely exponential demagnetization process (PM) with a larger amplitude around T_N. This further reinforces the idea that the oscillations are magnetic in nature. The increase in demagnetization signal across the phase boundary can be understood in the framework of a simple heating model proposed in [60], [134]. The evolution of the slow and fast demagnetization dynamics across the c-AFM-PM phase boundary is explored in more detail in Supplemental

note 5.

To gain additional insight into the magnetic nature of MBT we fit the spin precession frequency at 3.8 T as a function of temperature to the power law function:

$$Frequency \propto (\frac{T_N - T}{T_N})^{\beta} \tag{5.1}$$

which gives a critical exponent of β=0.332±0.028 and T_N is fit to 18.126±0.076. This reduced T_N can be explained by pump induced heating. At 18K, heating from the 20 $\mu J/cm^2$ pump is around 2.5 K, matching well with the previously mentioned T_N at 3.8 T of roughly 20 K [23], [24]. Supplemental note 1 provides more details on the pump-induced heating. As for the critical exponent, β=0.332±0.028 is quite close to the value seen in [23] of β=0.35±0.02, retrieved from Bragg intensity signal as a function of temperature. The value of β=0.332±0.028 is close to the 3D Ising model value of β=0.326 [137]. See Supplemental note 2 for more information on critical exponent fitting with heating accounted for.

The main take-away from the temperature sweep is that the spin precession appears to be intimately connected to the ground state behavior of the Mn d-spins present in the system. The frequency displays order parameter-like behavior, reproducing a similar T_N at 3.8 T, and showing clear differences in the response across the magnetic phase transitions in MBT. Supplemental note 5 has a detailed analysis of the fast and slow demagnetization amplitudes vs temperature at 3 different fields (3.8 T, 5.8 T, and 7 T), with both amplitudes being an accurate reporter on the magnetic ground state and closely reproducing the different T_N observed at different fields.

5.4.3 Magnetic field dependence of spin precession

To further investigate the magnetic nature of the oscillation seen in the c-AFM phase, we conducted a detailed field dependence from 3.8 T to 7 T in steps of 0.2 T while the sample was kept at 2 K. The magnetic field dependence of the spin

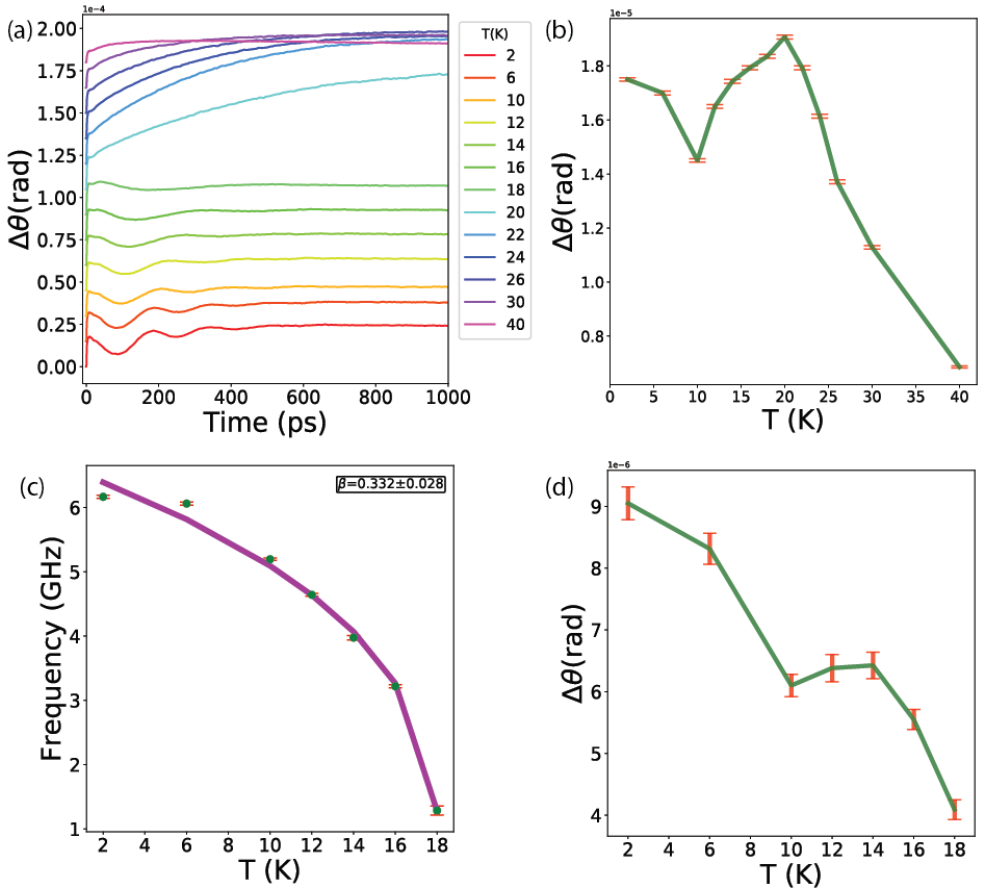

Figure 5.2: **Temperature dependence of spin precession a.** A temperature sweep taken at, 3.8 T, each temperature is presented with an offset to help show the dynamics. A clear cross-over in behavior is observed between 18 K and 20 K indicating the c-AFM-PM phase transition. **b.** Ultrafast demagnetization amplitude vs. temperature. **c.** Frequency vs. temperature, clear order parameter-like behavior occurs as the temperature approaches T_N, with a critical exponent of β=0.332. **d.** Precessional amplitude vs. temperature, also displaying magnetization-like behavior upon increasing the temperature to T_N.

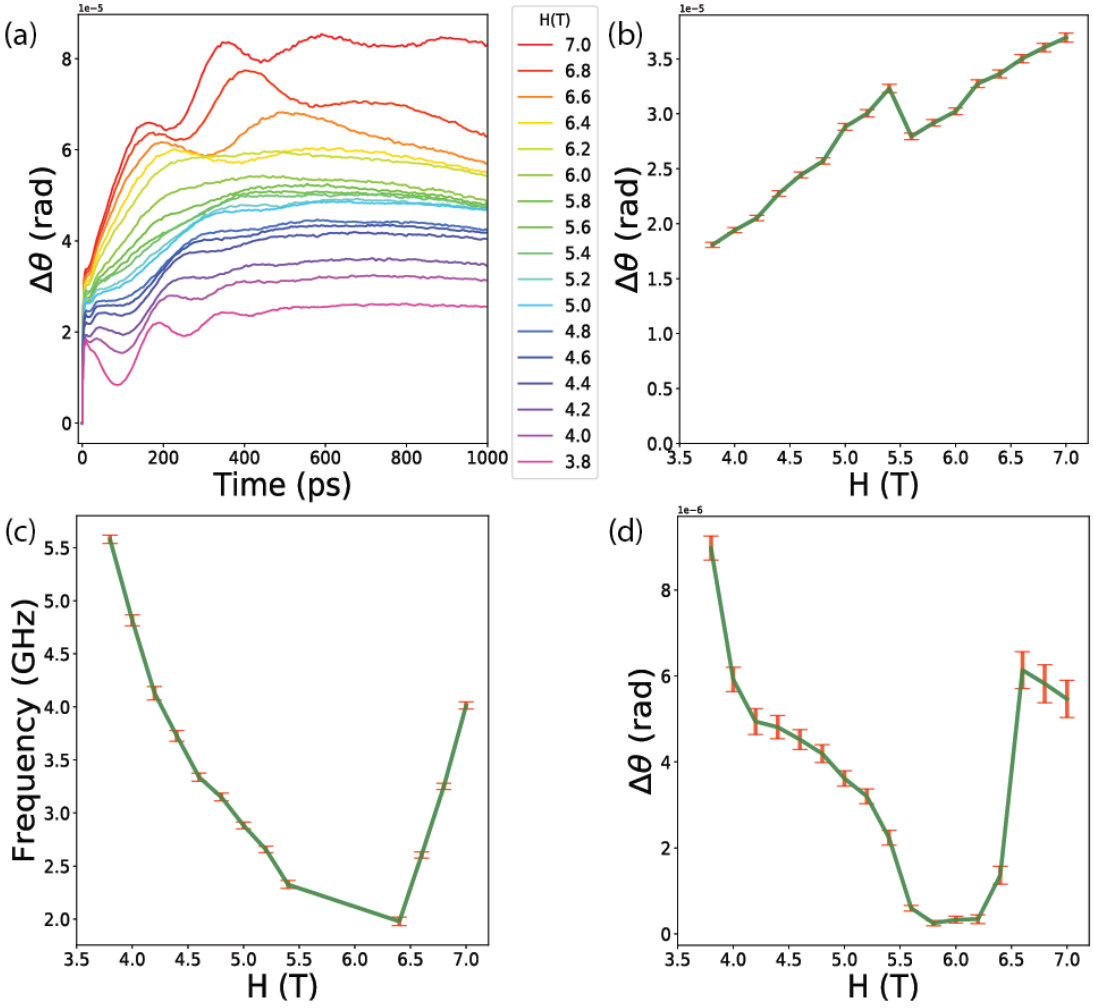

Figure 5.3: **Magnetic field dependence of spin precession**: **a.** A magnetic field sweep taken at 2 K. **b.** Ultrafast demagnetization amplitude vs. field extracted from the field sweep. **c.** Precessional frequency vs. field, initially decreasing with increasing field up to 5.4 T, from 6.4 T to 7 T frequency increases linearly. Data in the range of 5.6 T-6.2 T showed no apparent oscillations. **d.** Oscillation amplitude vs. field, computed by fitting the residual of the exponential fits to a decaying oscillation. For field values in the region of 5.6 T-6.2 T the dynamics fit well to a purely exponential model.

precession can be seen in Fig. 5.3a. As the field is increased from 3.8 T the amplitude and frequency of the oscillation decrease until, at around 6 T, the dynamics appear purely exponential in nature. Interestingly, as the field is increased past 6T the oscillation reappears with increasing frequency at larger fields as seen in Fig. 5.3c. Importantly, the oscillations reappear with a π phase shift as the field is increased past 6 T. This is an unexpected result, as this change from decreasing to increasing behavior with field usually marks the transition from c-AFM to FM alignment. This will be discussed in greater detail in Section V. In Fig. 5.3d the amplitude of the spin precession was calculated by fitting the residual signal taken from subtracting the data from the exponential fit described in methods and fitting it to a decaying oscillation. It is apparent from this plot that the field values 5.6 T-6.2 T display purely demagnetization dynamics, with no oscillations being observed. The Gilbert damping and decay times of the oscillation as a function of magnetic field are shown in Supplemental note 3.

In the following section magnon energies will be theoretically computed to aide in understanding the field dependence of the spin precession. Interestingly, Fig. 5.3b shows the ultrafast demagnetization signal increasing with field for all field steps except for a kink between 5.4 T and 5.6 T. Whether this is experimental noise and can be attributed to error or if it is indicative of an intrinsic physical change in the system is currently unclear. Importantly this points toward MBT still being in the c-AFM state in equilibrium up to 7 T, since magnetization monotonically increases with field in the c-AFM state until FM alignment. And as demonstrated in Fig. 5.2b, the ultrafast demagnetization amplitude is a good reporter of equilibrium magnetization in the sample.

5.4.4 Fluence dependence of spin precession

The spin precession dynamics at 3.8 T and 2 K, are plotted at several fluences in Fig. 5.4a,b. In general, the spin precession amplitude increases linearly with respect to fluence (Fig. 5.4d) up until around 200 $\mu J/cm^2$, where the behavior is a mixture between c-AFM spin precession and PM demagnetization, with the oscillation appearing over-damped. See Supplemental note 4 for more information on the fluence dependence. As seen in Fig. 5.4c, the frequency is relatively unaffected by increasing fluence with a more noticeable decrease in frequency happening at higher fluences. The frequency behavior can be attributed to the background thermalization that takes place amongst the Mn d spins and the lattice. In Supplemental note 2 the heating calculated from the frequency decreases in the fluence data extrapolates well to a basic two-temperature model (TTM). Information on the decay time and Gilbert damping of the oscillations as function of fluence is given in Supplemental note 3.

Both the oscillation amplitude and the ultrafast demagnetization (see Supplemental note 4) are linearly related to the fluence. This points toward the spin precession being tied to the ultrahot carriers excited by the pump. In previous optical studies on MBT with similar pump and probe energies [130], a linear relation between fluence and excited carriers observed in time-resolved reflectivity was established. In this paradigm the launching mechanism for the spin precession is caused by the absorption of a photon by the p-like spins in the system.

Starting from the oscillation which emerges in the TR-MOKE data as the magnetic order is changed from AFM to c-AFM we confirmed its magnetic nature by taking temperature dependent data. The precession amplitude and frequency both go to zero as the T_N is approached, with the frequency in particular showing order parameter-like behavior. The magnetic field was tuned and dramatic changes to the frequency, amplitude, and phase of the mode were observed. By taking data as a function of fluence the linear relation between ultrafast demagnetization, ultrahot

excited carriers, and precession amplitude is established. In the next section we use theory and modelling to uncover information about the mode we are exciting and the symmetry requirements.

5.5 Theory

In this section the magnetic Hamiltonian from Chapter 2 is used, where an external field along the z direction, parallel to the c-axis in MBT is applied.

$$H = J\sum_{\langle ij\rangle}\vec{S_i}\cdot\vec{S_j} - K\sum_i (S_i^z)^2 - \vec{H_{ext}}\cdot\sum_i \vec{S_i} \tag{5.2}$$

Using Holstein-Primakoff transformations analytic expressions for the magnon energies in the c-AFM phase are found with the two solutions corresponding to an upper and lower branch which represent optical and acoustic magnons respectively. Due to selection rules this will naturally be a k=0 magnon, the energies of the magnon branches at small k are:

$$\begin{aligned}\omega_k^+ &\sim \sqrt{2H_E(\frac{H_{ext}^2(2H_E+H_K)}{(2H_E-H_K)^2} - H_K)} + O(k^2)\\ \omega_k^- &\sim k\sqrt{H_E((2H_E-H_K)^2 - H_{ext}^2)} + O(k^2)\end{aligned} \tag{5.3}$$

where H_E and H_A are the exchange and anisotropy fields defined in Chapter 2. Using the values of H_E=5.1 T and H_A=1.58 T, at 3.8 T the ω_k^+ mode corresponds to a frequency of ∼75GHz. This upper branch mode also increases frequency with increasing field, opposite to what is observed in our experiments. The acoustic mode shows for finite k, increasing applied field will decrease the frequency up until zero, when the critical field of $H_{FM} = (2H_E - H_K)$ is achieved and the sample is FM aligned.

The main issue is the the linear dependence on k of the acoustic magnon mode, since we are limited to optical transition and processes, this means that the

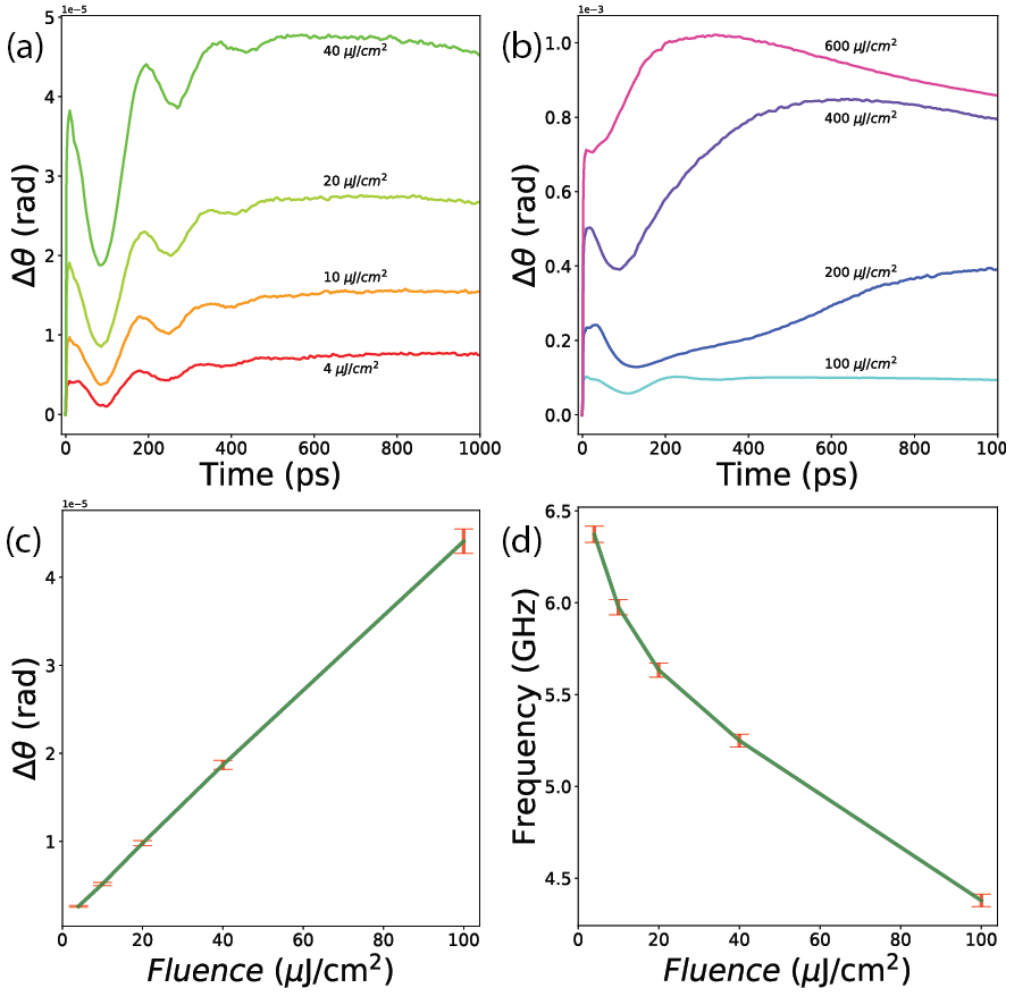

Figure 5.4: **Fluence dependence of spin precession**: **a,b.** Spin precession at 3.8 T swept through fluences of 4 $\mu J/cm^2$-40 $\mu J/cm^2$ in **a.** and 100 $\mu J/cm^2$-600 $\mu J/cm^2$ in **b**. For fluences up to 100 $\mu J/cm^2$ the spin precession can be clearly resolved. **c.** Spin precession amplitude vs. fluence for 4 $\mu J/cm^2$-100 $\mu J/cm^2$. **d.** Frequency vs. fluence for 4 $\mu J/cm^2$-100 $\mu J/cm^2$.

lower branch mode will always be gapless. One way to think of this is that with the field applied exactly along the c-axis, the system has $U(1)$ symmetry and will necessarily have gapless excitations. To overcome this an in-plane anisotropy must be considered to break this symmetry and gap the lower branch magnons at k=0. To explain this gapped behavior we considered a small misalignment between the magnetic field and the c-axis. The small misalignment breaks the U(1) symmetry and is found to gap the acoustic magnon branch at k=0 (see Fig. 5.5a). Now the expression for the lower branch acoustic magnon at k=0 with an in-plane anisotropy field H_{Kx} given by

$$\omega_{-}(k=0) = \sqrt{H_{Kx}(2H_E - (H_K - H_{Kx}) - \frac{H_{ext}^2}{2H_E - (H_K - H_{Kx})})} \tag{5.4}$$

In Fig. 5.5b, for small misalignment angles between three and five degrees there are oscillations which match both the frequency values and the field behavior extremely well. For the misalignment angle of 3.4 degrees in Fig. 5.5b, to fit to the experimental data the exchange field must be changed to twice its original value while the exchange field decreases by roughly 10%.

While the model accurately captures the frequency behavior of the gapped acoustic magnon from 3.8 T to 5.4 T it does not explain the oscillations seen at higher fields. In Fig. 5.5b after the mode goes to zero and the system is FM aligned, the frequency of the FM mode increases much fast with field than our experimental data. FM spin precession frequency is given by $\mu_B g H$, where g is the g-factor. This means that all FM spin precession should exhibit a frequency vs. field slope of 28 GHz/T. Our data in the FM-like region only has a slope of ~ 4 GHz/T. A possible explanation may be that as the system approaches FM alignment, the magnon energies tend toward zero. At these low energies their may be a large thermal population of magnons which can lead to enhanced interaction effects. These magnon-magnon interactions could play a role in altering the FM transition as well as changing the slope of frequencies with field.

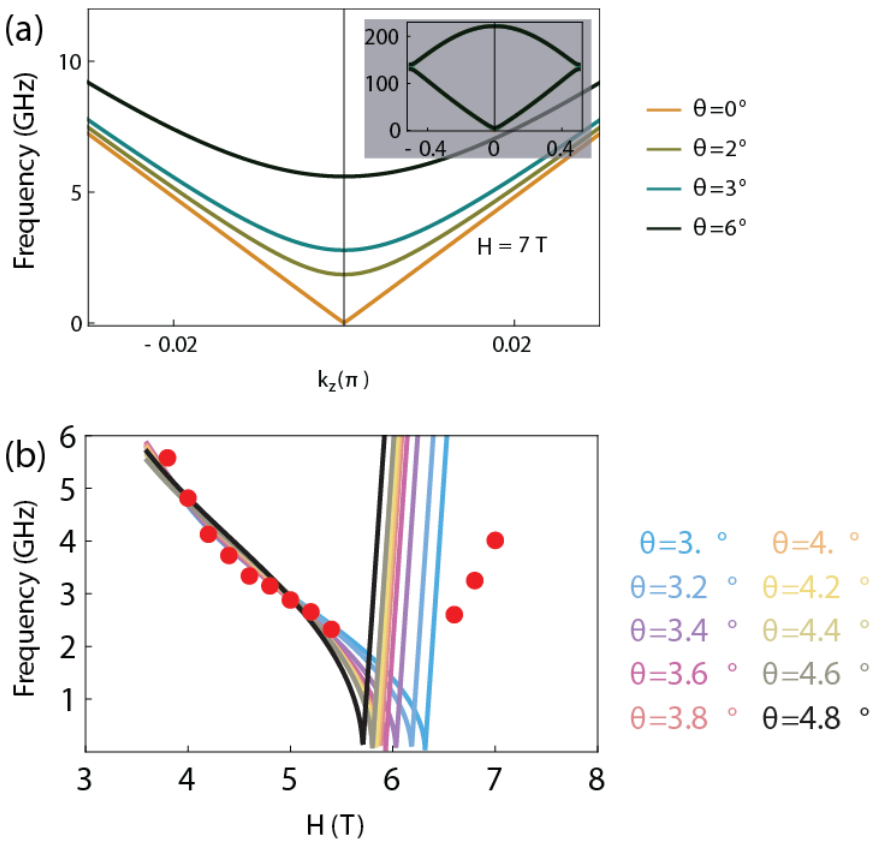

Figure 5.5: **Modelling the acoustic magnon with a misaligned field: a.** The acoustic branch dispersion close to the k=0 point at 7 T as a function of misalignment angles. Inset: zoomed out view of the optical and acoustic magnons when no misalignment is present. **b.** Frequency vs. field of the acoustic mode for different misalignment angles.

5.6 Discussion

In other studies on VdW materials with A-type AFM magnetic ordering there is an observed in-phase k=0 acoustic mode which is seen to decrease in frequency as magnetic field is increased in the geometry where the field induces a canting as it is applied perpendicular to the easy axis [60], [138], [139]. While our field is applied parallel to the easy axis, since MBT undergoes a spin-flop transition, above 3.8 T the field is effectively canting the sublattices in a similar fashion. In this scenario when the field fully polarizes the spins the low energy mode goes to zero, with the frequency increasing at a rate of 28 GHz/T once FM spin alignment is achieved by the external field. This is similar to what is seen in our data, interestingly though, the frequency goes to zero at around 6 T. This is well below the FM alignment of around 7.7 T, however in [139] the low energy mode also reaches zero frequency at a field slightly lower than the FM field. This behavior may be indicative of the crossover of c-AFM to FM-like magnons occurring at a lower field than the equilibrium crossover in vdW material.

We modeled the acoustic branch in the c-AFM state of MBT as a function of field and found that for many k values near k=0 the frequency behavior was matching what was seen in our data. One issue is that for k=0 the acoustic branch magnon energy is always zero, this can be resolved by the fact that our magnetic field is slightly offset from the c-axis, giving some in-plane anisotropy due to the external field. An in-plane anisotropy effectively gaps the magnon mode at k=0 on the acoustic branch and gives finite frequency to the spin precession which matches well with our data. A similar behavior has been observed in 7- and 8-SL MBT in [60], and was also explained as originating from the magnetic field having some in-plane component gapping the k=0 acoustic mode. The behavior with the field follows our data, with the frequency decreasing with increasing field. Additionally, the frequencies that we calculate with an in-plane anisotropy due to a slight misalignment

angle (3-4 degrees) agree with our values in the experiment. The consistency between both the frequency values and behavior with external field indicate that what we see in the TR-MOKE data is an acoustic magnon which is gapped due to a small in-plane anisotropy due to field misalignment or other effects, as we have discussed.

The c-AFM-FM type crossover at 6 T is not very well understood at the moment, however other works on MBT have noted AFM-FM like crossover in the magnon branches at around 6 T [137]. A study on another VdW AFM [139] see an FM crossover behavior in the magnon frequency vs field at slightly lower fields, similar to what we see. Developing a better understanding of why magnon dynamics in some vdW materials display a lower c-AFM to FM transition could guide the way towards the goal of controlling the magnetic ground state. Another open question is related to the behavior of how the spin precession evolves with external field takes past 6 T, where 'FM-like' spin precession is observed. FM-like precession in high fields should have a slope of 28 GHz/T, equal to the electron gyromagnetic ratio, and is observed in a similar optical MOKE experiment on a VdW magnet [139]. The FM-like spin processions observed in our data have a slope of around 3.5 GHz/T, which is a factor of 8 smaller than the expected value. This may be due to the high thermal magnon population around the c-AFM-FM transition field causing increased magnon-magnon interactions.

Despite MBT being an AFM, recent studies point toward it having FM character in the c-AFM phase. An ESR study [137] on $MnBi_2Te_4(Bi_2Te_3)_n$ n=0,1 demonstrated that $MnBi_4Te_7$ behaves like a FM even though it has AFM interlayer coupling. The authors explain that due to the weak interlayer coupling $MnBi_4Te_7$ displays FM like dynamics. Similarly they found that in $MnBi_{24}$ the magnon dispersions cross over from c-AFM-like to FM-like at around 6 T, before the FM transition and at a similar field where we see our frequency behavior reverse. Another reason why $MnBi_{24}$ may have FM-like characteristics is because of Mn_{Bi} antisite defects [140], [141]([140] was on $MnBi_4Te_7$ and $MnBi_6Te_{10}$). These defects place magnetic Mn ions

which carry a localized moment where Bi atoms should located. These misplaced Mn spins have an AFM coupling with the Mn spins in the middle layer of the same unit cell while having an FM coupling to adjacent Mn_{Bi} antisite spins, giving the system a ferrimagnetic like ordering. This type of defect with its associated couplings effectively lowers the energy for an FM alignment in MBT, although the amount of Mn_{Bi} defects vary greatly sample to sample and are intimately related to the growing conditions. This Ferrimagnetic configuration arising from Mn_{Bi} antisite defects could be a part of the explanation for the non-trivial behavior of the spin precession with applied field and why MBT plays host to FM like magnetic excitations below the FM saturation field. In addition to the competition between AFM and FM ground states, magnetic anisotropy in MBT is extremely dependent on the spin-orbit coupling of both the Mn and Te [142]. Since our pump is exciting electrons in the Te p-states it is reasonable to believe that this could be the cause of the change in anisotropy that our model predicts.

5.7 Conclusion

Time resolved MOKE is an invaluable tool for probing both the magnetic ground state and excitations in MBT. We see clear signs of phase transitions between the c-AFM and PM phases in the slow dynamics, while the fast dynamics give us a look at the equilibrium magnetization in the material. Sweeping temperature in the c-AFM state demonstrates how the spin precession evolves as a function of temperature, with the frequency in particular showing order parameter like behavior. The critical exponent matches up well with values reported in the literature, demonstrating that the oscillation is intimately related to the magnetism in MBT.

The magnetic field dependence of the spin precession in MBT is striking, and some features are slightly unexpected. We observe what appears to be a k=0 acoustic magnon that is gapped by a small in-plane component of the external magnetic field

due to misalignment. The behavior of the precession going to zero frequency at 6 T points to c-AFM–FM transition occurring at a field almost 2 T below what literature and our ultrafast tr-MOKE data indicate. Whether this is due to a massive pump-induced change in anisotropy and/or interlayer coupling or if the magnon spectrum in MBT naturally goes from AFM-FM at lower fields than equilibrium, which has been reported elsewhere[137] remains to be seen. Additionally, in what appears to be the FM state, the precession frequency vs. field slope is much lower than the expected value of 28 GHz/T. The prospect of understanding this spin precession data is exciting since there is a natural incentive to control magnetism in MBT to switch between topological states in the material. Understanding why the excitation spectrum can be biased toward FM behavior at lower fields than the equilibrium transition then that may open the door for tuning the magnetic ground state between c-AFM-FM on demand.

5.8 Supplementary Information

5.8.1 Pump-induced heating

When looking at time-resolved pump-probe data, it is absolutely imperative that one understands the effects of laser heating on the sample, and MBT is no exception. The top temperature vs. fluence plot was calculated using a two temperature model (TTM), wherein energy in the form of the pump pulse is deposited into the electron subsystem, which initially thermalizes with itself on ultrafast timescales (electron-electron thermalization), and then with the lattice on longer but still ultrafast timescales (1-2ps). This two temperature model neglects both the itinerant spin systems from the p-like bands of Te and Bi and the localized Mn 3d spins. This means that the heating calculated with the TTM is an upper bound since it does not account for energy flowing into the spin subsystems.

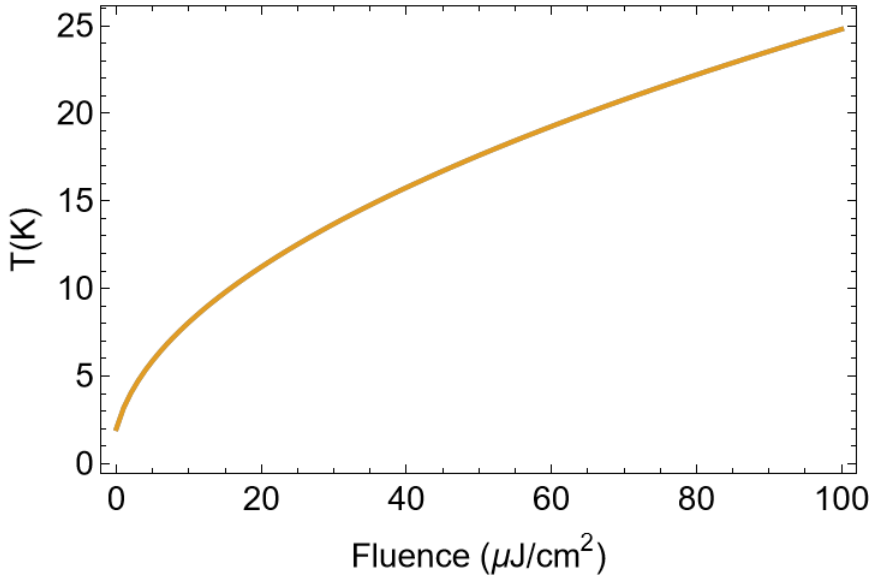

Figure 5.6: Heating vs. Fluence calculated from the TTM.

Using a fluence of 20 $\mu J/cm^2$, our sample is heated from 2 K to 11.2 K by the pump. Again, to reiterate: since the TTM ignores the spin subsystems this is no doubt an upper bound of the heating, and as we'll see in the next section we most likely heat the sample to around 8.6 K under normal experimental conditions.

5.8.2 Heating calculated from fluence data

Operating under the assumption that the frequency change in the fluence sweep originates from background heating, the frequency vs. fluence data can be used to estimate heating vs. fluence. First the low fluence data is used to approximate what the zero fluence frequency would be at 2K. Using the same power law dependence of $\beta = 0.332$, and with a zero temperature frequency estimated from the low fluence and low temperature data we can now estimate the heating from the fluence data. By equating the frequency at a certain fluence to a frequency as a function of temperature using the power law equation the heating at each fluence can be calculated. From the right side of Fig. 5.7 it can be seen that the TTM overestimates

the equilibrium temperature reached by electron-lattice thermalization. This makes sense since the TTM neglects both the spin subsytems of the Mn d-spins and the Bi and Te p-spins. The heating calculated from the fluence data predicts that the 20 $\mu J/cm^2$ pump fluence at 2 K causes the sample to reach a temperature of around 8.6 K. Using the heating calculated from the heating data a frequency vs. temperature plot can be made using adjusted values of temperature to account for the heating from our pump. On the left of Fig. 5.7 we can see that the critical exponent is slightly higher than the original value of 0.332, and now the critical temperature for this adjusted plot is fit to T_C=20.7 K, which agrees extremely well with previous values reported in literature [23], [24].

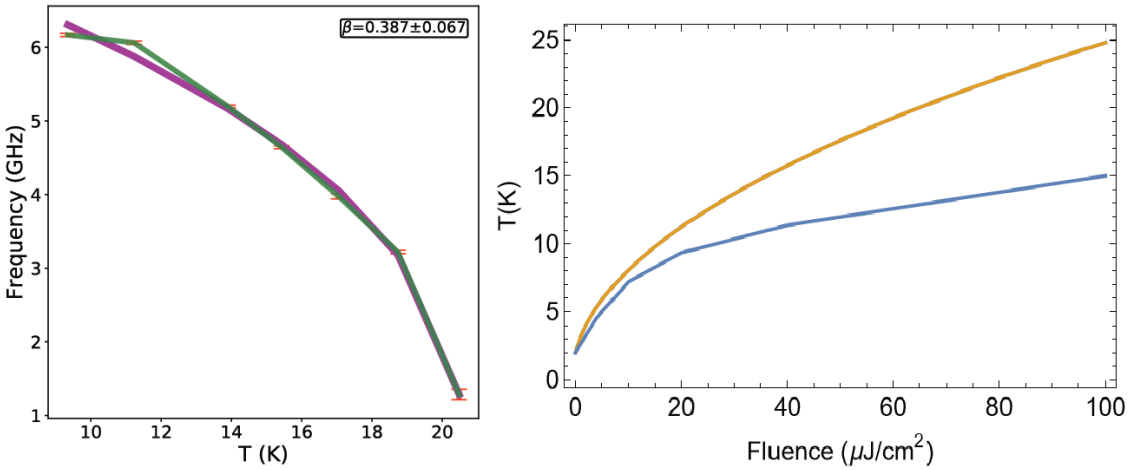

Figure 5.7: **Left:** Critical exponent fit for frequency vs. temperature plot, with the temperatures adjusted for pump heating. **Right:** The heating calculated from the frequency vs. fluence data set (blue) compared to the TTM heating (orange).

5.8.3 Decay times and Gilbert damping

In Fig. 5.8 a.-c. The decay times of the spin precession oscillations are shown as a function of temperature, fluence, and field, respectively. To complement these decay times in Fig. 5.8 d.-f. The Gilbert damping ($\alpha = \frac{1}{\omega t_3}$) of the spin precession

oscillations are shown as a function of temperature, fluence, and field, respectively. In general, the temperature and fluence plots tell a similar story of the decay time decreasing as the temperature increased. Note however, the last two temperatures show an increasing decay time which goes against this trend. The decrease of decay time with temperature can be rationalized by the fact that spin fluctuations increase around magnetic phase transitions [36]. The increase of spin fluctuations around phase transitions can cause the oscillations to die out faster than they would at lower temperatures. Fig. 5.8d.,e. the Gilbert damping monotonically increases as a function of fluence and temperature, in part due to the decreasing decay times but mostly due to the decrease in frequency seen in these data sets. Fig. 5.8c shows the decay time of the oscillations increase with increasing field. The Gilbert damping in Fig. 5.8f staying mostly flat in the field region where the acoustic mode is observed, before dropping noticeably in the FM-like region of precession. The fact that the oscillations decay slower in the high field regions is intriguing because opposite behavior was observed for the field in-plane acoustic magnons seen in [60].

5.8.4 Fluence dependence of demagnetization times and amplitudes

As mentioned earlier, there are two slow demagetization times, one on the order of 300 ps which is attributed to Mn d-spin-lattice thermalization, and another on the order of 70 ps which comes J_{pd} coupling. The latter is only seen at higher fluence, in Fig. 5.9 the J_{pd} demagnetization can be seen causing an increasingly rapid demagnetization with increasing fluence for all three sampled fields. For more information on J_{pd} coupling and its implication towards topological properties in MBT refer to [134].

Fig. 5.10 shows the ultrafast demagnetization dynamics as a function of fluence. The left figure shows that when normalized to the value at 10 ps, the different

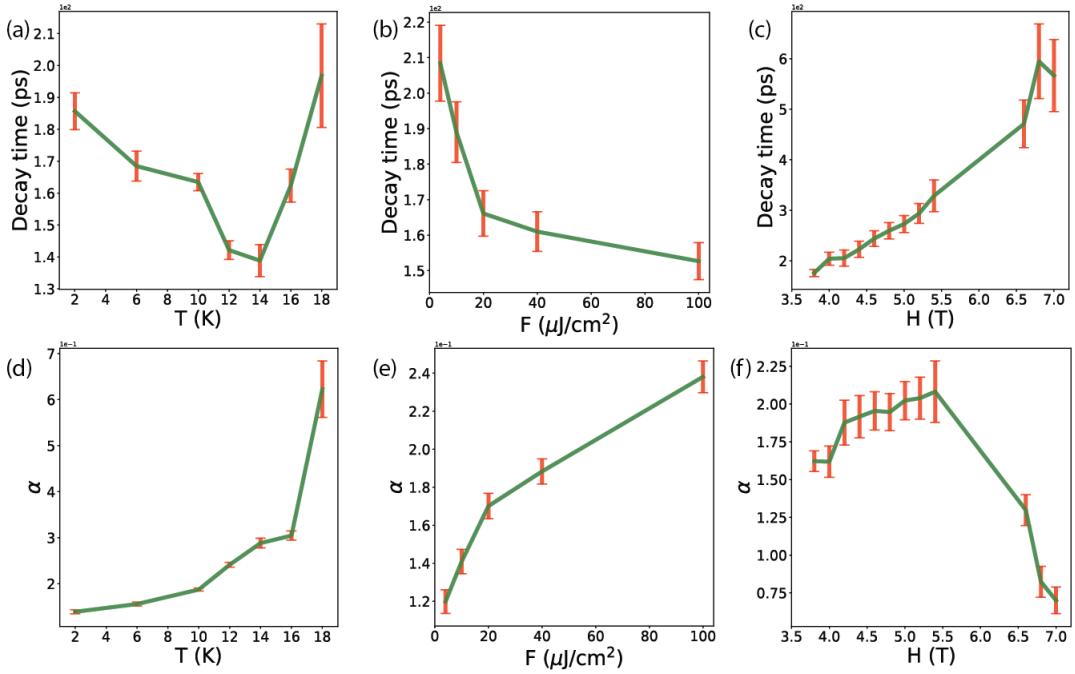

Figure 5.8: **a.-c.** Decay time as a function of temperature (**a.**), fluence (**b.**), and field (**c.**).**d.-f.** Gilbert damping calculated from the decay times in **a.-c.**.

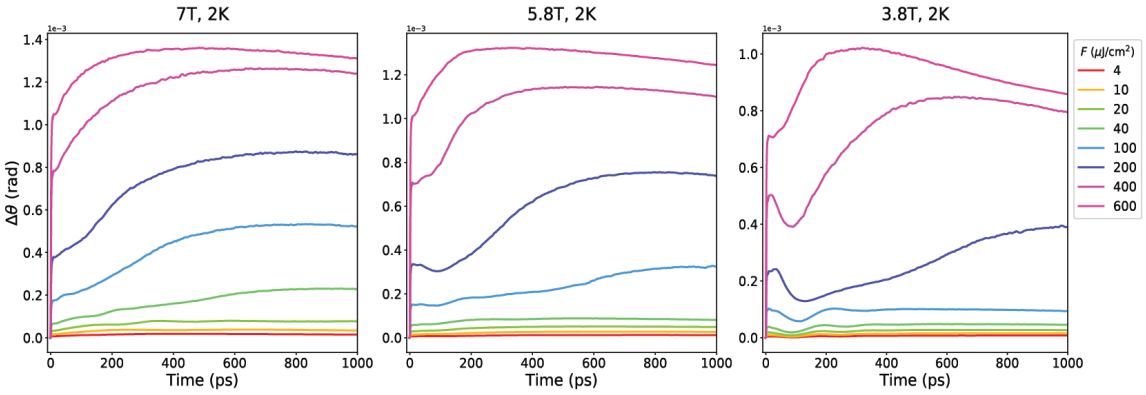

Figure 5.9: Fluence sweeps at 3.8 T, 5.8 T, and 7 T, with all data taken at 2 K.

fluence scans have similar dynamics. The figure on the right plots demagnetizaiton amplitude at 10 ps vs. fluence, and demonstrates a linear relationship between ultrafast demagnetization and pump fluence. The fact that ultrafast demagnetization,

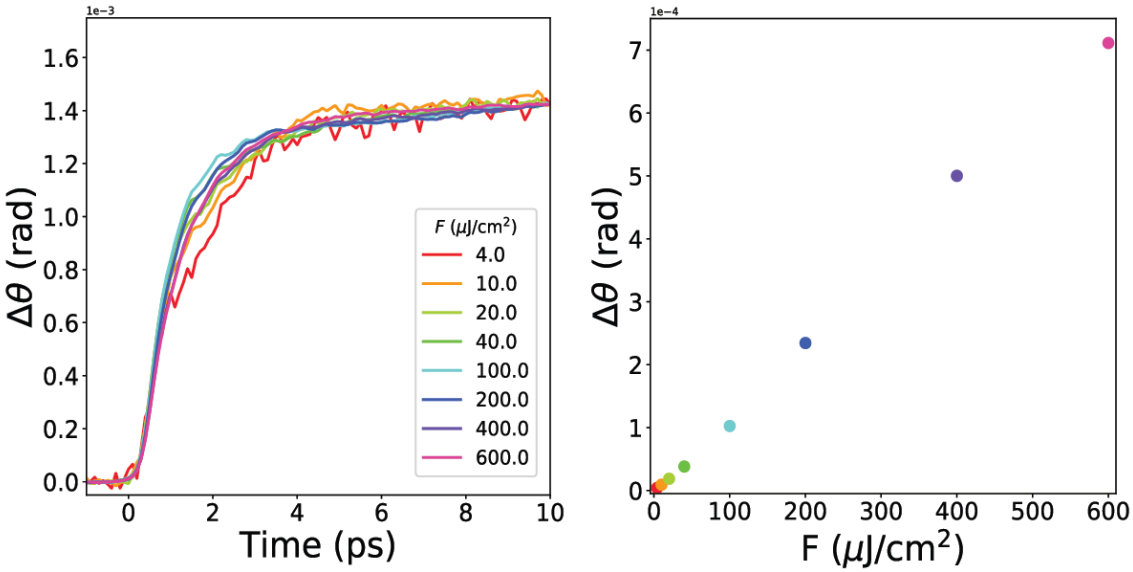

Figure 5.10: **Left figure:** Fluence sweep taken at 3.8 T, 2 K, with scans normalized at 10 ps. Since the dynamics are similar over this time we can take the signal at 10 ps as an accurate reporter on demagnetizaion amplitude. **Right figure:** TR-MOKE amplitude at 10 ps vs. fluence. From these plots we can see that the dynamics are relatively unchanged with fluence, and amplitude grows linearly with increasing fluence.

ultrahot carriers [130], phonon amplitude in TR-reflectivity [130], and spin precession amplitude all scale linearly with fluence is important and points to the crucial role the pump pulse plays in these phenomena.

5.8.5 Temperature dependence of the fast and slow demagnetization components at 3.8 T, 5.8 T, and 7 T

At 3.8 T in the fast time amplitudes, but also present in the slow time amplitudes and precessional amplitudes, is a noticeable decrease around 10 K. In Fig5.11a we see that there is an anomalous "dip" in the amplitude around 10 K that is not seen in susceptibility measurements, but that the surrounding temperatures also display this trend of decreasing toward 10 K on either side. The origin of the decreased ultrafast demagnetization amplitude and subsequent smaller long time demagneti-

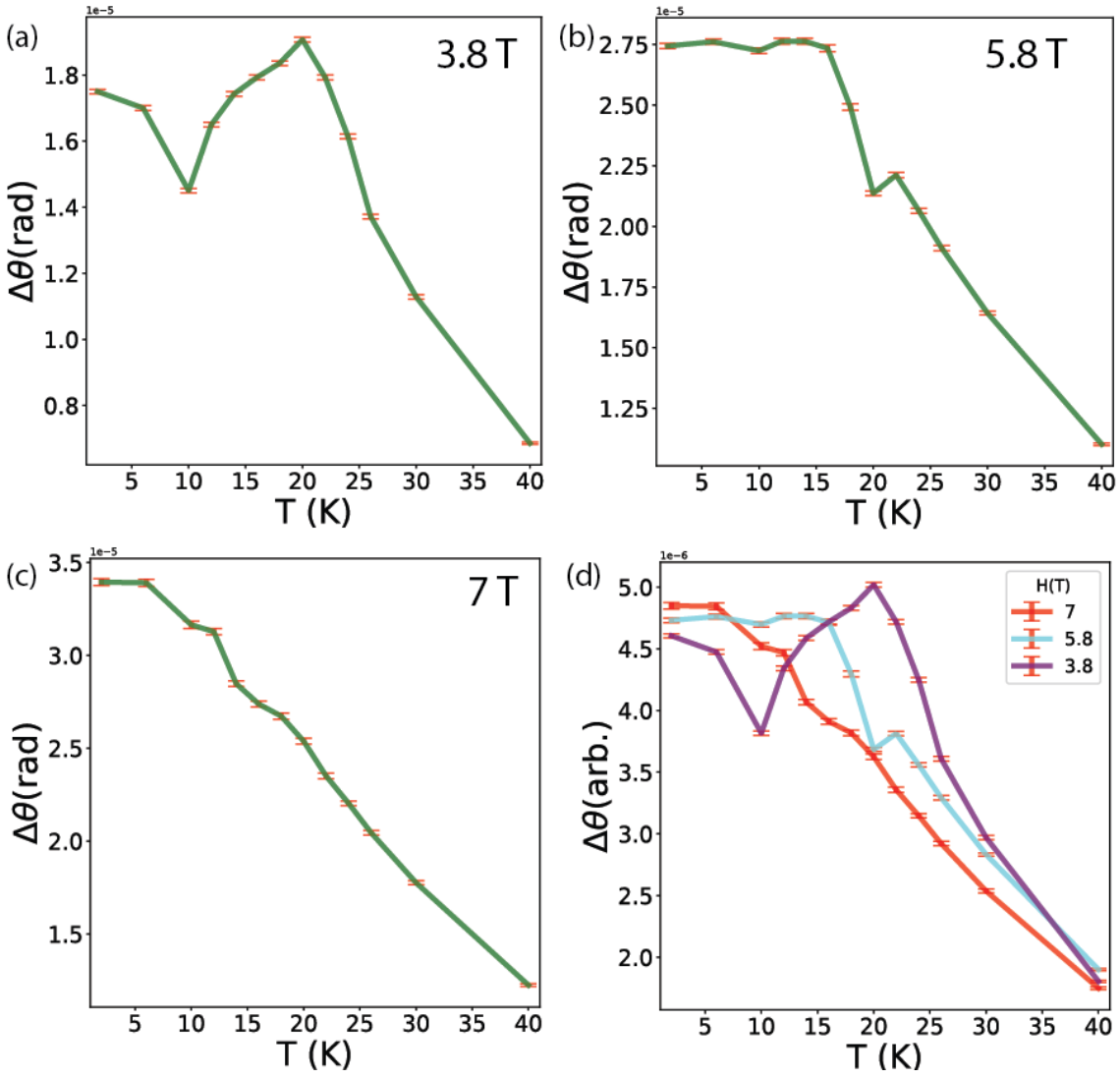

Figure 5.11: Ultrafast demagnetization amplitude vs. temperature at 3.8 T (**a.**), 5.8 T (**b.**), and 7 T (**c.**). In **d.** all three fields plots are normalized by dividing the amplitude by the field.

zation and spin precession amplitudes is not well understood at the moment, and warrants further investigation.

In Fig. 5.12 a comparison between the ultrafast demagnetization normalized by external field and χ vs. temperature at different fields is shown. The striking

agreement means that our ultrafast demagnetization signal is proportional to the local magnetization in both the c-AFM and PM phases. This makes sense since the demagnetization mechanism (Elliot-Yafet) is reliant on itinerant spins scattering off of optical phonons, and the electron-phonon coupling parameter is temperature independent for the temperatures considered in this experiment [134]. This paints a picture of our pump pulse being absorbed and causing a population of excited carriers (which are proportional to the pump fluence), these excited carriers scatter off of optical phonons which causes a demagnetization which is proportional to the fluence and therefore the absorbed photons. This means that the ultrafast demagnetization is a light induced effect and not tied to background heating, but rather to the excitation of p-like carriers from the valance to the conduction band.

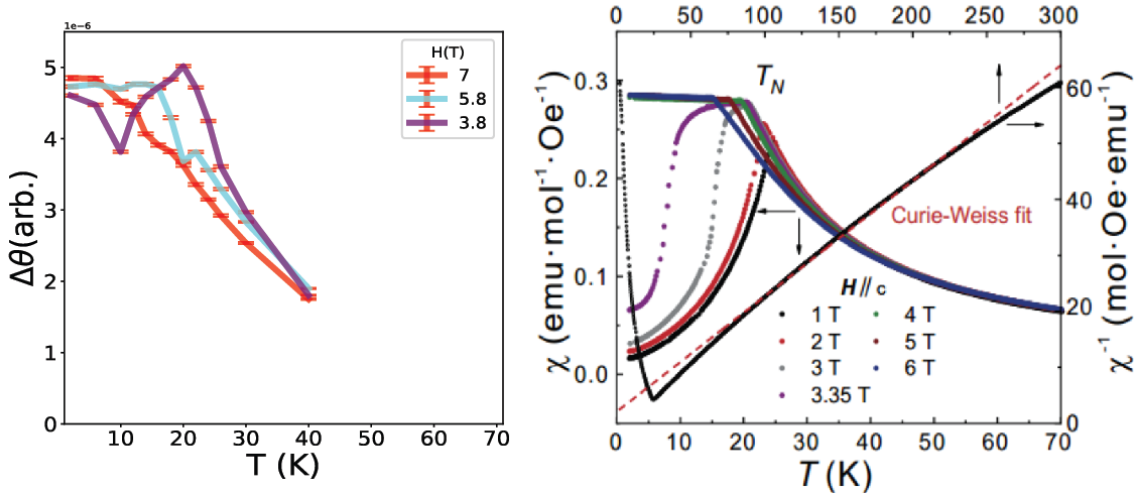

Figure 5.12: Comparison between the ultrafast demagnetization data that is normalized by the applied field and the χ vs. temperature data from [24]. Clearly the ultrafast demagnetization amplitude tracks the equilibrium magnetization quite well.

In previous works [60], [134], the long time demagnetization dynamics in MBT could be explained by a simple pump-induced heating framework, where the tr-MOKE signal would show an increase in magnetization at low magnetic fields up to Tn. By referencing the χ-temperature curve below, from [24], one can see

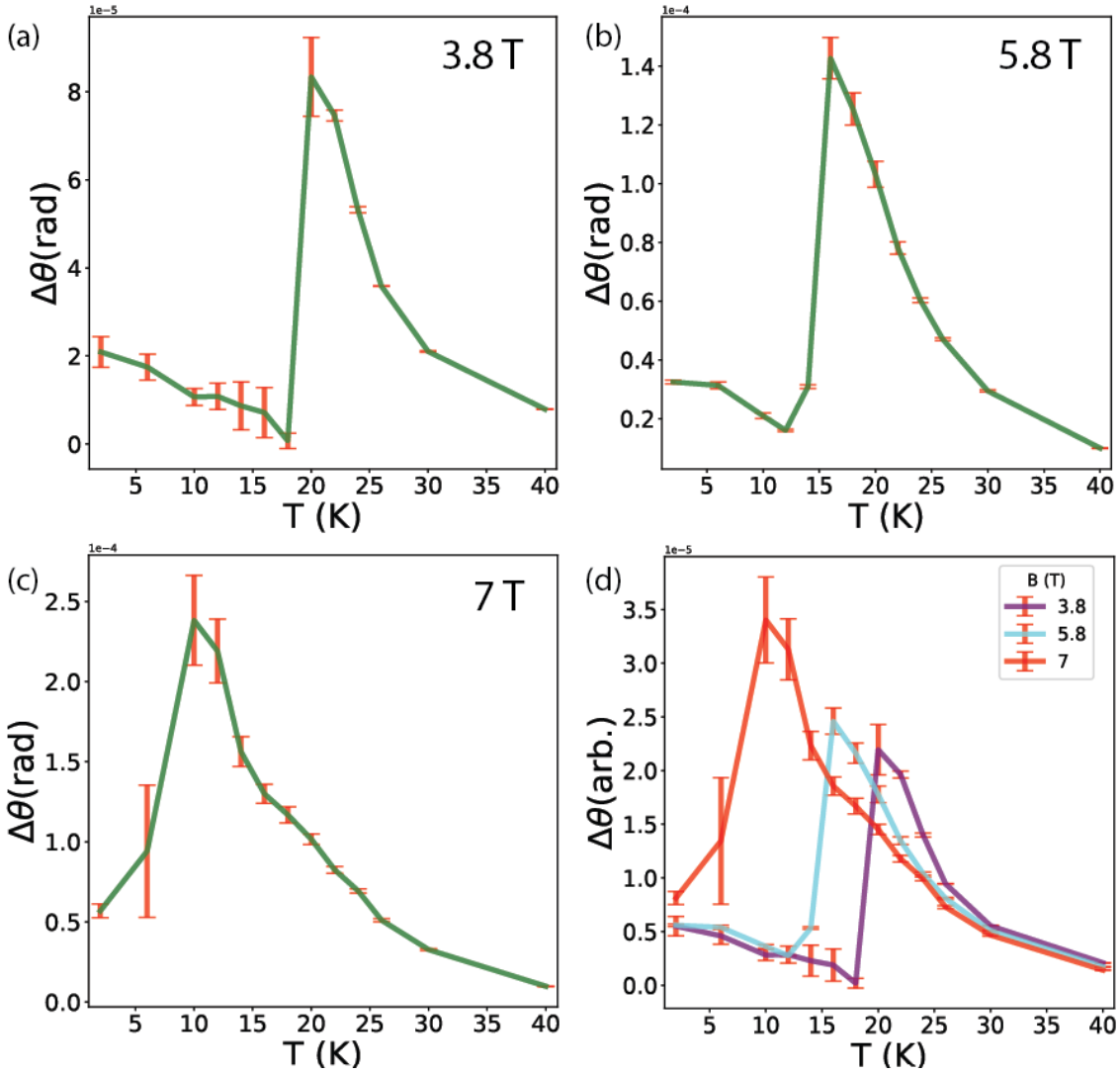

Figure 5.13: Slow demagnetization amplitude vs. temperature at 3.8 T (**a.**), 5.8 T (**b.**), and 7 T (**c.**). In **d.** all three fields plots are normalized by dividing the amplitude by the field.

how increasing the temperature in the sample causes the magnetization to decrease across the transition temperature and cause a large demagnetization signal. A similar model of calculating magnetization change due to a change in temperature was also used in figure 2. of [60] and explained their long time tr-MOKE data as well.

The peak in our long time dynamics can be understood in a similar framework. As MBT approaches Tn for these fields we see a stark drop off in magnetization as it enters the paramagnetic state, this explains the sudden increase in the demagnetization signal. Furthermore the χ-T curve shows as field is increased and T_N becomes smaller, the slope of decrease in magnetization also decreases, creating a more "broad" demagnetization with temperature. Our longtime demagnetization data mirrors this broadening of the demagnetization amplitude with temperature further demonstrating that tr-MOKE is a powerful and accurate reporter of spin dynamics and structure in MBT. To help visualize this all three fields were plotted together and you can quite clearly see both the decrease of Tn with increasing field as well as the broadening of the demagnetization amplitude with higher fields.

One thing that does stand out is the signal at the temperature just before the c-AFM-PM crossover, in both the 3.8 T and the 5.8 T longtime amplitudes seems to drop to almost 0. This can be understood in the heating framework; at higher temperatures the specific heat is higher as well, meaning that the sample will heat up much less at 18 K vs. 2 K for the same 20 $\mu J/cm^2$ pump pulse. The long demagnetization amplitude trending toward 0 as the transition temperature is approached is due to decreasing heating at higher temperatures.

5.9 Acknowledgments

Chapter 5, in part, is currently being prepared for submission for publication. Maxwell Poore, Swati Chaudhary, Peter K. Kim, Martin Rodriguez-Vega, Hari Padmanabhan, Seng Huat Lee, Zhiqiang Mao, Venkatraman Gopalan, Gregory A Fiete, and Richard D. Averitt. The dissertation author was the primary investigator and author of this material.

Appendix A

$A_{1g}^{(1)}$ phonon oscillations in tr-MOKE

To resolve the most minute details of the ultrafast response of the tr-MOKE scans we collected data at 3.8 T, 2 K, 100 $\mu J/cm^2$, from -0.5 ps to 3 ps in 25 fs steps, while averaging 100 scans. This extreme amount of precision in the time domain coupled with the large number of scans averaged gave us insight into the ultrafast magnetic response of MBT. Strikingly there are clear oscillations, notable in the time domain in Fig A.1.a,b. Fourier transforming the data in Fig A.1.b yields a spike at around 1.5 THz which can be seen in Fig A.1.c, corresponding to the $A_{1g}^{(1)}$ phonon mode mentioned previously. While studies have shown that A_{1g} phonons can strongly influence the interlayer exchange in MBT due to their eigendisplacements within the lattice [99], [130], it is remarkable to see the magnetism respond on the exact timescale of the phonon oscillation. To make sure we are observing purely magnetic dynamics and not a parasitic Fresnel coefficient we follow the test outlined in section 3.6. In Fig A.1.d we can see the excellent agreement between rotation and ellipticity, indicating that the data in Fig A.1.a was purely from the magnetization dynamics and the phonon oscillations observed correspond to magnetic oscillations at

that frequency. While this result was left out of the original work due to uncertainty over whether or not the oscillations were magnetic in origin or arise from our $\Delta R/R$ signal, the strong agreement between θ and η in time warrant further investigation.

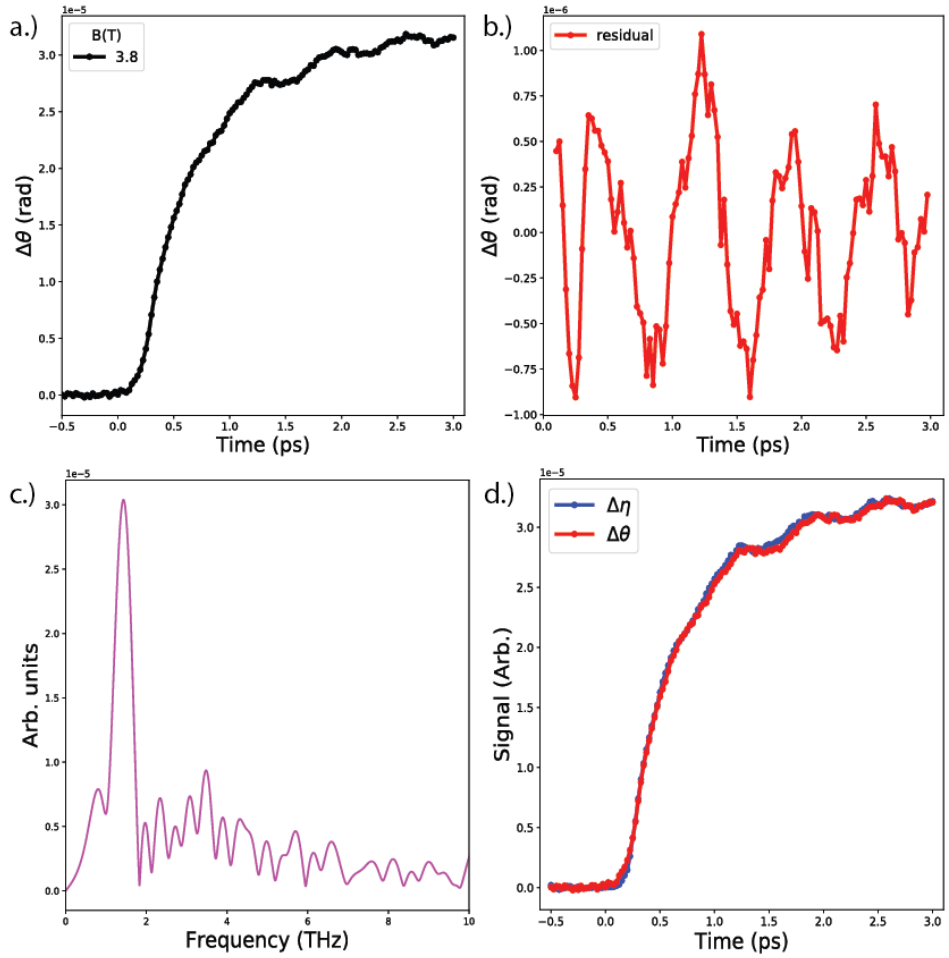

Figure A.1: **Oscillations at the $A_{1g}^{(1)}$ phonon frequency in tr-MOKE: a.** Tr-MOKE scan taken at 3.8 T, 2 K, and a pump fluence of 100 $\mu J/cm^2$, oscillations are clearly visible on top of the ultrafast demagnetization signal. **b.** The residual oscillations left after subtraction the data in **a.** with a model fitting the exponential decay. **c.** An FFT of the oscillations in **b.**, with a clear peak around 1.5 THz, corresponding to the $A_{1g}^{(1)}$ phonon mode seen in ΔR/R. **d.** θ vs. η measurements taken at the same expeimental condition (3.8 T, 2 K, 100 $\mu J/cm^2$) to ensure that there is sufficient overlap between rotation and ellipticity to demonstrate that the data in **a.** was purely magnetic in nature.

Bibliography

[1] M. Dressel and G. Grüner, *Electrodynamics of Solids: Optical Properties of Electrons in Matter*. Cambridge: Cambridge University Press, 1976.

[2] D. B. Tanner, *Optical Effects in Solids*. Cambridge: Cambridge University Press, 2019.

[3] P. Drude, "Zur elektronentheorie der metalle", *Annalen der physik*, vol. 306, no. 3, pp. 566–613, 1900.

[4] N. W. Ashcroft and N. D. Mermin, *Solid state physics*. Philadelphia: Saunders College Publishing, 1976.

[5] R. W. Boyd, A. L. Gaeta, and E. Giese, "Nonlinear optics", in *Springer Handbook of Atomic, Molecular, and Optical Physics*, Springer, 2008, pp. 1097–1110.

[6] C. Manzoni and G. Cerullo, "Design criteria for ultrafast optical parametric amplifiers", *Journal of Optics*, vol. 18, no. 10, p. 103 501, 2016.

[7] M. Knorr, J. Raab, M. Tauer, P. Merkl, D. Peller, E. Wittmann, E. Riedle, C. Lange, and R. Huber, "Phase-locked multi-terahertz electric fields exceeding 13 mv/cm at a 190 khz repetition rate", *Optics letters*, vol. 42, no. 21, pp. 4367–4370, 2017.

[8] J. Wang, "Time-resolved magneto-optical spectroscopy", in *Optical Techniques for Solid-State Materials Characterization*, A. J. Taylor and R. P. Prasankumar, Eds. CRC Press, 2012.

[9] P. N. Argyres, "Theory of the faraday and kerr effects in ferromagnetics", *Physical Review*, vol. 97, no. 2, p. 334, 1955.

[10] H. Le Gall and J. Jamet, "Theory of the elastic and inelastic scattering of light by magnetic crystals. i. first-order processes", *physica status solidi (b)*, vol. 46, no. 2, pp. 467–482, 1971.

[11] S. Visnovsky, *Optics in magnetic multilayers and nanostructures*. Crc Press, 2006.

[12] R. Yu, W. Zhang, H.-J. Zhang, S.-C. Zhang, X. Dai, and Z. Fang, "Quantized anomalous hall effect in magnetic topological insulators", *Science*, vol. 329, no. 5987, pp. 61–64, 2010.

[13] C.-Z. Chang, J. Zhang, X. Feng, J. Shen, Z. Zhang, M. Guo, K. Li, Y. Ou, P. Wei, L.-L. Wang, Z.-Q. Ji, Y. Feng, S. Ji, X. Chen, J. Jia, X. Dai, Z. Fang, S.-C. Zhang, K. He, Y. Wang, L. Lu, and X.-C. Ma, "Experimental observation of the quantum anomalous hall effect in a magnetic topological insulator", *Science*, vol. 340, no. 6129, pp. 167–170, 2013.

[14] J. Checkelsky, R. Yoshimi, A. Tsukazaki, K. Takahashi, Y. Kozuka, J. Falson, M. Kawasaki, and Y. Tokura, "Trajectory of the anomalous hall effect towards the quantized state in a ferromagnetic topological insulator", *Nature Physics*, vol. 10, no. 10, pp. 731–736, 2014.

[15] X. Kou, S.-T. Guo, Y. Fan, L. Pan, M. Lang, Y. Jiang, Q. Shao, T. Nie, K. Murata, J. Tang, Y. Wang, L. He, T.-K. Lee, W.-L. Lee, and K. L. Wang, "Scale-invariant quantum anomalous hall effect in magnetic topological insu-

lators beyond the two-dimensional limit", *Physical Review Letters*, vol. 113, no. 13, p. 137 201, 2014.

[16] A. Bestwick, E. Fox, X. Kou, L. Pan, K. L. Wang, and D. Goldhaber-Gordon, "Precise quantization of the anomalous hall effect near zero magnetic field", *Physical Review Letters*, vol. 114, no. 18, p. 187 201, 2015.

[17] A. Kandala, A. Richardella, S. Kempinger, C.-X. Liu, and N. Samarth, "Giant anisotropic magnetoresistance in a quantum anomalous hall insulator", *Nature Communications*, vol. 6, no. 1, p. 7434, 2015.

[18] C.-Z. Chang, W. Zhao, D. Y. Kim, H. Zhang, B. A. Assaf, D. Heiman, S.-C. Zhang, C. Liu, M. H. Chan, and J. S. Moodera, "High-precision realization of robust quantum anomalous hall state in a hard ferromagnetic topological insulator", *Nature Materials*, vol. 14, no. 5, pp. 473–477, 2015.

[19] M. M. Otrokov, T. V. Menshchikova, M. G. Vergniory, I. P. Rusinov, A. Y. Vyazovskaya, Y. M. Koroteev, G. Bihlmayer, A. Ernst, P. M. Echenique, A. Arnau, and E. V. Chulkov, "Highly-ordered wide bandgap materials for quantized anomalous hall and magnetoelectric effects", *2D Materials*, vol. 4, no. 2, p. 025 082, 2017.

[20] Y. Chen, J. G. Analytis, J.-H. Chu, Z. Liu, S.-K. Mo, X.-L. Qi, H. Zhang, D. Lu, X. Dai, Z. Fang, S. C. Zhang, I. R. Fisher, Z. Hussain, and Z.-X. Shen, "Experimental realization of a three-dimensional topological insulator, Bi_2Te_3", *Science*, vol. 325, no. 5937, pp. 178–181, 2009.

[21] M. M. Otrokov, I. I. Klimovskikh, H. Bentmann, D. Estyunin, A. Zeugner, Z. S. Aliev, S. Gaß, A. U. B. Wolter, A. V. Koroleva, A. M. Shikin, M. Blanco-Rey, M. Hoffman, I. P. Rusinov, A. Y. Vyazovskaya, S. V. Eremeev, Y. M. Koroteev, V. M. Kuznetsov, F. Freyse, J. Sánchez-Barriga, I. R. Amiraslanov, M. B. Babanly, N. T. Mamedov, N. A. Abdullayev, V. N. Zverev, A. Alfonsov, V. Kataev, B. Büchner, E. F. Schwier, S. Kumar, A. Kimura, L. Petaccia, G.

Di Santo, R. C. Vidal, S. Schatz, K. Kißner, M. Ünzelmann, C. H. Min, S. Moser, T. R. F. Peixoto, F. Reinert, A. Ernst, P. M. Echenique, A. Isaeva, and E. V. Chulkov, "Prediction and observation of an antiferromagnetic topological insulator", *Nature*, vol. 576, no. 7787, pp. 416–422, 2019.

[22] Y.-J. Hao, P. Liu, Y. Feng, X.-M. Ma, E. F. Schwier, M. Arita, S. Kumar, C. Hu, R. Lu, M. Zeng, Y. Wang, Z. Hao, H.-Y. Sun, K. Zhang, J. Mei, N. Ni, L. Wu, K. Shimada, C. Chen, Q. Liu, and C. Liu, "Gapless surface dirac cone in antiferromagnetic topological insulator $MnBi_2Te_4$", *Physical Review X*, vol. 9, no. 4, p. 041 038, 2019.

[23] J.-Q. Yan, Q. Zhang, T. Heitmann, Z. Huang, K. Chen, J.-G. Cheng, W. Wu, D. Vaknin, B. C. Sales, and R. J. McQueeney, "Crystal growth and magnetic structure of $MnBi_2Te_4$", *Physical Review Materials*, vol. 3, no. 6, p. 064 202, 2019.

[24] H. Li, S. Liu, C. Liu, J. Zhang, Y. Xu, R. Yu, Y. Wu, Y. Zhang, and S. Fan, "Antiferromagnetic topological insulator $MnBi_2Te_4$: Synthesis and magnetic properties", *Physical Chemistry Chemical Physics*, vol. 22, no. 2, pp. 556–563, 2020.

[25] A. Gao, Y.-F. Liu, C. Hu, J.-X. Qiu, C. Tzschaschel, B. Ghosh, S.-C. Ho, D. Bérubé, R. Chen, H. Sun, Z. Zhang, X.-Y. Zhang, Y.-X. Wang, N. Wang, Z. Huang, C. Felser, A. Agarwal, T. Ding, H.-J. Tien, A. Akey, J. Gardener, B. Singh, K. Watanabe, T. Taniguchi, K. S. Burch, D. C. Bell, B. B. Zhou, W. Gao, H.-Z. Lu, A. Bansil, H. Lin, T.-R. Chang, L. Fu, Q. Ma, N. Ni, and S.-Y. Xu, "Layer hall effect in a 2d topological axion antiferromagnet", *Nature*, vol. 595, no. 7868, pp. 521–525, 2021.

[26] J. Li, Y. Li, S. Du, Z. Wang, B.-L. Gu, S.-C. Zhang, K. He, W. Duan, and Y. Xu, "Intrinsic magnetic topological insulators in van der waals layered $MnBi_2Te_4$-family materials", *Science Advances*, vol. 5, no. 6, eaaw5685, 2019.

[27] C. Liu, Y. Wang, H. Li, Y. Wu, Y. Li, J. Li, K. He, Y. Xu, J. Zhang, and Y. Wang, "Robust axion insulator and chern insulator phases in a two-dimensional antiferromagnetic topological insulator", *Nature Materials*, vol. 19, no. 5, pp. 522–527, Jan. 2020. DOI: 10.1038/s41563-019-0573-3.

[28] R. S. Mong, A. M. Essin, and J. E. Moore, "Antiferromagnetic topological insulators", *Physical Review B*, vol. 81, no. 24, p. 245 209, 2010.

[29] Y. J. Chen, L. X. Xu, J. H. Li, Y. W. Li, H. Y. Wang, C. F. Zhang, H. Li, Y. Wu, A. J. Liang, C. Chen, S. W. Jung, C. Cacho, Y. H. Mao, S. Liu, M. X. Wang, Y. F. Guo, Y. Xu, Z. K. Liu, L. X. Yang, and Y. L. Chen, "Topological electronic structure and its temperature evolution in antiferromagnetic topological insulator $MnBi_2Te_4$", *Physical Review X*, vol. 9, no. 4, p. 041 040, 2019.

[30] H. Li, S.-Y. Gao, S.-F. Duan, Y.-F. Xu, K.-J. Zhu, S.-J. Tian, J.-C. Gao, W.-H. Fan, Z.-C. Rao, J.-R. Huang, J.-J. Li, D.-Y. Yan, Z.-T. Liu, W.-L. Liu, Y.-B. Huang, Y.-L. Li, Y. Liu, G.-B. Zhang, P. Zhang, T. Kondo, S. Shin, H.-C. Lei, Y.-G. Shi, W.-T. Zhang, H.-M. Weng, T. Qian, and H. Ding, "Dirac surface states in intrinsic magnetic topological insulators $EuSn_2As_2$ and $MnBi_{2n}Te_{3n+1}$", *Physical Review X*, vol. 9, no. 4, p. 041 039, 2019.

[31] C. Yan, S. Fernandez-Mulligan, R. Mei, S. H. Lee, N. Protic, R. Fukumori, B. Yan, C. Liu, Z. Mao, and S. Yang, "Origins of electronic bands in the antiferromagnetic topological insulator $MnBi_2Te_4$", *Physical Review B*, vol. 104, no. 4, p. L041102, 2021.

[32] P. Swatek, Y. Wu, L.-L. Wang, K. Lee, B. Schrunk, J. Yan, and A. Kaminski, "Gapless dirac surface states in the antiferromagnetic topological insulator $MnBi_2Te_4$", *Physical Review B*, vol. 101, no. 16, p. 161 109, 2020.

[33] B. Chen, F. Fei, D. Zhang, B. Zhang, W. Liu, S. Zhang, P. Wang, B. Wei, Y. Zhang, Z. Zuo, J. Guo, Q. Liu, Z. Wang, X. Wu, J. Zong, X. Xie, W. Chen, Z. Sun, S. Wang, Y. Zhang, M. Zhang, X. Wang, F. Song, H. Zhang, D. Shen, and B. Wang, "Intrinsic magnetic topological insulator phases in the sb doped $MnBi_2Te_4$ bulks and thin flakes", *Nature Communications*, vol. 10, no. 1, p. 4469, 2019.

[34] D. Nevola, H. X. Li, J.-Q. Yan, R. Moore, H.-N. Lee, H. Miao, and P. D. Johnson, "Coexistence of surface ferromagnetism and a gapless topological state in $MnBi_2Te_4$", *Physical Review Letters*, vol. 125, no. 11, p. 117 205, 2020.

[35] N. Bielinski, R. Chari, J. May-Mann, S. Kim, J. Zwettler, Y. Deng, A. Aishwarya, S. Roychowdhury, C. Shekhar, M. Hashimoto, D. Lu, J. Yan, C. Felser, V. Madhavan, Z.-X. Shen, T. L. Hughes, and F. Mahmood, "Revealing the hidden dirac gap in a topological antiferromagnet using floquet-bloch manipulation", *arXiv preprint arXiv:2405.16432*, 2024.

[36] S. H. Lee, Y. Zhu, Y. Wang, L. Miao, T. Pillsbury, H. Yi, S. Kempinger, J. Hu, C. A. Heikes, P. Quarterman, W. Ratcliff, J. A. Borchers, H. Zhang, X. Ke, D. Graf, N. Alem, C.-z. Chang, N. Samarth, and Z. Mao, "Spin scattering and noncollinear spin structure-induced intrinsic anomalous hall effect in antiferromagnetic topological insulator $MnBi_2Te_4$", *Physical Review Research*, vol. 1, no. 1, p. 012 011, 2019.

[37] E. D. Rienks, S. Wimmer, J. Sánchez-Barriga, O. Caha, P. S. Mandal, J. Ržička, A. Ney, H. Steiner, V. V. Volobuev, H. Groiss, M. Albu, G. Kothleitner, J. Michalička, S. A. Khan, J. Minár, H. Ebert, G. Bauer, F. Freyse, A. Varykhalov, O. Rader, and G. Springholz, "Large magnetic gap at the dirac point in $Bi_2Te_3/MnBi_2Te_4$ heterostructures", *Nature*, vol. 576, no. 7787, pp. 423–428, 2019.

[38] R. C. Vidal, H. Bentmann, T. R. F. Peixoto, A. Zeugner, S. Moser, C.-H. Min, S. Schatz, K. Kißner, M. Ünzelmann, C. I. Fornari, H. B. Vasili, M. Valvidares, K. Sakamoto, D. Mondal, J. Fujii, I. Vobornik, S. Jung, C. Cacho, T. K. Kim, R. J. Koch, C. Jozwiak, A. Bostwick, J. D. Denlinger, E. Rotenberg, J. Buck, M. Hoesch, F. Diekmann, S. Rohlf, M. Kalläne, K. Rossnagel, M. M. Otrokov, E. V. Chulkov, M. Ruck, A. Isaeva, and F. Reinert, "Surface states and rashba-type spin polarization in antiferromagnetic $MnBi_2Te_4(0001)$", *Physical Review B*, vol. 100, no. 12, p. 121 104, 2019.

[39] D. A. Estyunin, I. I. Klimovskikh, A. M. Shikin, E. F. Schwier, M. M. Otrokov, A. Kimura, S. Kumar, S. O. Filnov, Z. S. Aliev, M. B. Babanly, and E. V. Chulkov, "Signatures of temperature driven antiferromagnetic transition in the electronic structure of topological insulator $MnBi_2Te_4$", *APL Materials*, vol. 8, no. 2, 2020.

[40] A. Zeugner, F. Nietschke, A. U. Wolter, S. Gaß, R. C. Vidal, T. R. Peixoto, D. Pohl, C. Damm, A. Lubk, R. Hentrich, S. K. Moser, C. Fornari, C. H. Min, S. Schatz, K. Kißner, M. Ünzelmann, M. Kaiser, F. Scaravaggi, B. Rellinghaus, K. Nielsch, C. Hess, B. Büchner, F. Reinert, H. Bentmann, O. Oeckler, T. Doert, M. Ruck, and A. Isaeva, "Chemical aspects of the candidate antiferromagnetic topological insulator $MnBi_2Te_4$", *Chemistry of Materials*, vol. 31, no. 8, pp. 2795–2806, 2019.

[41] A. M. Shikin, D. A. Estyunin, N. L. Zaitsev, D. Glazkova, I. I. Klimovskikh, S. O. Filnov, A. G. Rybkin, E. F. Schwier, S. Kumar, A. Kimura, N. Mamedov, Z. Aliev, M. B. Babanly, K. Kokh, O. E. Tereshchenko, M. M. Otrokov, E. V. Chulkov, K. A. Zvezdin, and A. K. Zvezdin, "Sample-dependent dirac-point gap in $MnBi_2Te_4$ and its response to applied surface charge: A combined photoemission and ab initio study", *Physical Review B*, vol. 104, no. 11, p. 115 168, 2021.

[42] Y. Deng, Y. Yu, M. Z. Shi, Z. Guo, Z. Xu, J. Wang, X. H. Chen, and Y. Zhang, "Quantum anomalous hall effect in intrinsic magnetic topological insulator $MnBi_2Te_4$", *Science*, vol. 367, no. 6480, pp. 895–900, 2020.

[43] H. Deng, Z. Chen, A. Wołoś, M. Konczykowski, K. Sobczak, J. Sitnicka, I. V. Fedorchenko, J. Borysiuk, T. Heider, Ł. Pluciński, K. Park, A. Georgescu, J. Cano, and L. Krusin-Elbaum, "High-temperature quantum anomalous hall regime in a $MnBi_2Te_4/Bi_2Te_3$ superlattice", *Nature Physics*, vol. 17, no. 1, pp. 36–42, 2021.

[44] J. Cai, D. Ovchinnikov, Z. Fei, M. He, T. Song, Z. Lin, C. Wang, D. Cobden, J.-H. Chu, Y.-T. Cui, *et al.*, "Electric control of a canted-antiferromagnetic chern insulator", *Nature communications*, vol. 13, no. 1, p. 1668, 2022.

[45] H. Lu, Y. Huang, Q. Guo, K. Wang, M. He, Z. Yin, D. Wang, T. Liu, J. Wang, G. Yu, *et al.*, "Transport properties of crystallized antiferromagnetic $MnBi_2Te_4$ thin films grown by magnetron sputtering", *Journal of Physics D: Applied Physics*, vol. 56, no. 4, p. 045 302, 2022.

[46] D. Zhang, M. Shi, T. Zhu, D. Xing, H. Zhang, and J. Wang, "Topological axion states in the magnetic insulator $MnBi_2Te_4$ with the quantized magnetoelectric effect", *Physical Review Letters*, vol. 122, no. 20, p. 206 401, 2019.

[47] M. Z. Hasan and C. L. Kane, "Colloquium: Topological insulators", *Reviews of modern physics*, vol. 82, no. 4, p. 3045, 2010.

[48] M. V. Berry, "Quantal phase factors accompanying adiabatic changes", *Proceedings of the Royal Society of London. A. Mathematical and Physical Sciences*, vol. 392, no. 1802, pp. 45–57, 1984.

[49] D. J. Thouless, M. Kohmoto, M. P. Nightingale, and M. den Nijs, "Quantized hall conductance in a two-dimensional periodic potential", *Physical Review Letters*, vol. 49, no. 6, p. 405, 1982.

[50] L. Fu and C. L. Kane, "Time reversal polarization and a Z_2 adiabatic spin pump", *Physical Review B*, vol. 74, no. 19, p. 195 312, 2006.

[51] C. L. Kane and E. J. Mele, "Z_2 topological order and the quantum spin hall effect", *Physical Review Letters*, vol. 95, no. 14, p. 146 802, 2005.

[52] L. Fu and C. L. Kane, "Topological insulators with inversion symmetry", *Physical Review B*, vol. 76, no. 4, p. 045 302, 2007.

[53] S. M. Rezende, *Fundamentals of magnonics*. Springer, 2020, vol. 969.

[54] H.-F. Li, "Possible ground states and parallel magnetic-field-driven phase transitions of collinear antiferromagnets", *Npj Computational Materials*, vol. 2, no. 1, pp. 1–8, 2016.

[55] H.-F. Li and Z. Tang, "Ground and applied-field-driven magnetic states of antiferromagnets", *arXiv preprint arXiv:2109.03485*, 2021.

[56] M. Holtschneider and W. Selke, "Uniaxially anisotropic antiferromagnets in a field on a square lattice", *The European Physical Journal B*, vol. 62, pp. 147–154, 2008.

[57] S. Yang, X. Xu, Y. Zhu, R. Niu, C. Xu, Y. Peng, X. Cheng, X. Jia, Y. Huang, X. Xu, J. Lu, and Y. Ye, "Odd-even layer-number effect and layer-dependent magnetic phase diagrams in $MnBi_2Te_4$", *Physical Review X*, vol. 11, no. 1, p. 011 003, 2021.

[58] R. W. Wang, D. L. Mills, E. E. Fullerton, J. E. Mattson, and S. D. Bader, "Surface spin-flop transition in Fe/Cr(211) superlattices: Experiment and theory", *Physical Review Letters*, vol. 72, no. 6, p. 920, 1994.

[59] F. Keffer and H. Chow, "Dynamics of the antiferromagnetic spin-flop transition", *Physical Review Letters*, vol. 31, no. 17, p. 1061, 1973.

[60] F. M. Bartram, M. Li, L. Liu, Z. Xu, Y. Wang, M. Che, H. Li, Y. Wu, Y. Xu, J. Zhang, S. Yang, and L. Yang, "Real-time observation of magnetization and magnon dynamics in a two-dimensional topological antiferromagnet $MnBi_2Te_4$", *Science Bulletin*, vol. 68, no. 22, pp. 2734–2742, 2023.

[61] D. Ovchinnikov, X. Huang, Z. Lin, Z. Fei, J. Cai, T. Song, M. He, Q. Jiang, C. Wang, H. Li, Y. Wang, Y. Wu, D. Xiao, J.-H. Chu, J. Yan, C.-Z. Chang, Y.-T. Cui, and X. Xu, "Intertwined topological and magnetic orders in atomically thin chern insulator $MnBi_2Te_4$", *Nano letters*, vol. 21, no. 6, pp. 2544–2550, 2021.

[62] C. Rulliere *et al.*, *Femtosecond laser pulses*. New York: Springer, 2005.

[63] D. Strickland and G. Mourou, "Compression of amplified chirped optical pulses", *Optics communications*, vol. 55, no. 6, pp. 447–449, 1985.

[64] M. Bradler, P. Baum, and E. Riedle, "Femtosecond continuum generation in bulk laser host materials with sub-μj pump pulses", *Applied Physics B*, vol. 97, pp. 561–574, 2009.

[65] C.-K. Sun, F. Vallée, L. Acioli, E. Ippen, and J. Fujimoto, "Femtosecond-tunable measurement of electron thermalization in gold", *Physical Review B*, vol. 50, no. 20, p. 15 337, 1994.

[66] R. D. Averitt, S. L. Westcott, and N. J. Halas, "Ultrafast optical properties of gold nanoshells", *JOSA B*, vol. 16, no. 10, pp. 1814–1823, 1999.

[67] B. Koopmans, M. Van Kampen, J. Kohlhepp, and W. De Jonge, "Ultrafast magneto-optics in nickel: Magnetism or optics?", *Physical Review Letters*, vol. 85, no. 4, p. 844, 2000.

[68] L. Guidoni, E. Beaurepaire, and J.-Y. Bigot, "Magneto-optics in the ultrafast regime: Thermalization of spin populations in ferromagnetic films", *Physical Review Letters*, vol. 89, no. 1, p. 017 401, 2002.

[69] D. N. Basov, R. D. Averitt, D. Van Der Marel, M. Dressel, and K. Haule, "Electrodynamics of correlated electron materials", *Reviews of Modern Physics*, vol. 83, no. 2, p. 471, 2011.

[70] S.-W. Cheong and M. Mostovoy, "Multiferroics: A magnetic twist for ferroelectricity", *Nature Materials*, vol. 6, no. 1, pp. 13–20, 2007.

[71] Y. Tokura, K. Yasuda, and A. Tsukazaki, "Magnetic topological insulators", *Nature Reviews Physics*, vol. 1, no. 2, pp. 126–143, 2019.

[72] K. S. Burch, D. Mandrus, and J.-G. Park, "Magnetism in two-dimensional van der waals materials", *Nature*, vol. 563, no. 7729, pp. 47–52, 2018.

[73] S. Jiang, J. Shan, and K. F. Mak, "Electric-field switching of two-dimensional van der waals magnets", *Nature Materials*, vol. 17, no. 5, pp. 406–410, 2018.

[74] S. Jiang, L. Li, Z. Wang, K. F. Mak, and J. Shan, "Controlling magnetism in 2d CrI_3 by electrostatic doping", *Nature Nanotechnology*, vol. 13, no. 7, pp. 549–553, 2018.

[75] S. H. Lee, D. Graf, L. Min, Y. Zhu, H. Yi, S. Ciocys, Y. Wang, E. S. Choi, R. Basnet, A. Fereidouni, A. Wegner, Y.-F. Zhao, K. Verlinde, J. He, R. Redwing, V. Gopalan, H. O. H. Churchill, A. Lanzara, S. Nitin, C.-Z. Chang, J. Hu, and Z. Q. Mao, "Evidence for a magnetic-field-induced ideal type-II weyl state in antiferromagnetic topological insulator $Mn(Bi_{1-x}Sb_x)_2Te_4$", *Physical Review X*, vol. 11, no. 3, p. 031 032, 2021.

[76] J. Choe, D. Lujan, M. Rodriguez-Vega, Z. Ye, A. Leonardo, J. Quan, T. N. Nunley, L.-J. Chang, S.-F. Lee, J. Yan, G. A. Fiete, R. He, and X. Li, "Electron–phonon and spin–lattice coupling in atomically thin layers of $MnBi_2Te_4$", *Nano letters*, vol. 21, no. 14, pp. 6139–6145, 2021.

[77] J. F. Ryan and J. F. Scott, "Raman study of soft zone-boundary phonons and antiferrodistortive phase transition in BaMnF4", *Solid State Communications*, vol. 14, no. 1, pp. 5–9, 1974.

[78] D. A. Tenne and X. Xi, "Raman spectroscopy of ferroelectric thin films and superlattices", *Journal of the American Ceramic Society*, vol. 91, no. 6, pp. 1820–1834, 2008.

[79] D. Chapron, F. Cordero, and M. D. Fontana, "Characterization of oxygen vacancies in $SrTiO_3$ by means of anelastic and raman spectroscopy", *Journal of Applied Physics*, vol. 126, no. 15, 2019.

[80] N. Sivadas, S. Okamoto, X. Xu, C. J. Fennie, and D. Xiao, "Stacking-dependent magnetism in bilayer CrI_3", *Nano letters*, vol. 18, no. 12, pp. 7658–7664, 2018.

[81] J. Li, J. Ni, X. Li, H.-J. Koo, M.-H. Whangbo, J. Feng, and H. Xiang, "Intralayer ferromagnetism between S=$\frac{5}{2}$ ions in $MnBi_2Te_4$: Role of empty bi p states", *Physical Review B*, vol. 101, no. 20, p. 201 408, 2020.

[82] T. Stevens, J. Kuhl, and R. Merlin, "Coherent phonon generation and the two stimulated raman tensors", *Physical Review B*, vol. 65, no. 14, p. 144 304, 2002.

[83] G. A. Garrett, T. Albrecht, J. Whitaker, and R. Merlin, "Coherent thz phonons driven by light pulses and the sb problem: What is the mechanism?", *Physical Review Letters*, vol. 77, no. 17, p. 3661, 1996.

[84] H. Zeiger, J. Vidal, T. Cheng, E. Ippen, G. Dresselhaus, and M. Dresselhaus, "Theory for displacive excitation of coherent phonons", *Physical Review B*, vol. 45, no. 2, p. 768, 1992.

[85] G. Güntherodt, W. Bauhofer, and G. Benedek, "Zone-boundary-phonon raman scattering in VI_2 due to modulation of exchange interaction", *Physical Review Letters*, vol. 43, no. 19, p. 1427, 1979.

[86] T. Sekine, M. Jouanne, C. Julien, and M. Balkanski, "Light-scattering study of dynamical behavior of antiferromagnetic spins in the layered magnetic semiconductor $FePS_3$", *Physical Review B*, vol. 42, no. 13, p. 8382, 1990.

[87] A. McCreary, T. T. Mai, F. G. Utermohlen, J. R. Simpson, K. F. Garrity, X. Feng, D. Shcherbakov, Y. Zhu, J. Hu, D. Weber, K. Watanabe, T. Taniguchi, J. E. Goldberger, Z. Mao, C. N. Lau, Y. Lu, N. Trivedi, R. V. Aguilar, and A. R. H. Walker, "Distinct magneto-raman signatures of spin-flip phase transitions in CrI_3", *Nature Communications*, vol. 11, no. 1, p. 3879, 2020.

[88] X. Wang, K. Du, Y. Y. F. Liu, P. Hu, J. Zhang, Q. Zhang, M. H. S. Owen, X. Lu, C. K. Gan, P. Sengupta, C. Kloc, and Q. Xiong, "Raman spectroscopy of atomically thin two-dimensional magnetic iron phosphorus trisulfide ($FePS_3$) crystals", *2D Materials*, vol. 3, no. 3, p. 031 009, 2016.

[89] M. Först, C. Manzoni, S. Kaiser, Y. Tomioka, Y. Tokura, R. Merlin, and A. Cavalleri, "Nonlinear phononics as an ultrafast route to lattice control", *Nature Physics*, vol. 7, no. 11, pp. 854–856, 2011.

[90] D. M. Juraschek and S. F. Maehrlein, "Sum-frequency ionic raman scattering", *Physical Review B*, vol. 97, no. 17, p. 174 302, 2018.

[91] A. Stupakiewicz, C. Davies, K. Szerenos, D. Afanasiev, K. Rabinovich, A. Boris, A. Caviglia, A. Kimel, and A. Kirilyuk, "Ultrafast phononic switching of magnetization", *Nature Physics*, vol. 17, no. 4, pp. 489–492, 2021.

[92] D. Afanasiev, J. Hortensius, B. Ivanov, A. Sasani, E. Bousquet, Y. Blanter, R. Mikhaylovskiy, A. Kimel, and A. Caviglia, "Ultrafast control of magnetic in-

teractions via light-driven phonons", *Nature Materials*, vol. 20, no. 5, pp. 607–611, 2021.

[93] P. Padmanabhan, F. L. Buessen, R. Tutchton, K. W. C. Kwock, S. Gilinsky, M. C. Lee, M. A. McGuire, S. R. Singamaneni, D. A. Yarotski, A. Paramekanti, J.-X. Zhu, and P. Prasankumar, "Coherent helicity-dependent spin-phonon oscillations in the ferromagnetic van der waals crystal CrI_3", *Nature Communications*, vol. 13, no. 1, p. 4473, 2022.

[94] A. S. Disa, M. Fechner, T. F. Nova, B. Liu, M. Först, D. Prabhakaran, P. G. Radaelli, and A. Cavalleri, "Polarizing an antiferromagnet by optical engineering of the crystal field", *Nature Physics*, vol. 16, no. 9, pp. 937–941, 2020.

[95] F. Giorgianni, B. Wehinger, S. Allenspach, N. Colonna, C. Vicario, P. Puphal, E. Pomjakushina, B. Normand, and C. Rüegg, "Ultrafast frustration breaking and magnetophononic driving of singlet excitations in a quantum magnet", *Physical Review B*, vol. 107, no. 18, p. 184 440, 2023.

[96] C. A. Belvin, E. Baldini, I. O. Ozel, D. Mao, H. C. Po, C. J. Allington, S. Son, B. H. Kim, J. Kim, I. Hwang, J. H. Kim, J.-G. Park, T. Senthil, and N. Gedik, "Exciton-driven antiferromagnetic metal in a correlated van der waals insulator", *Nature Communications*, vol. 12, no. 1, p. 4837, 2021.

[97] D. Afanasiev, J. R. Hortensius, M. Matthiesen, S. Mañas-Valero, M. Šiškins, M. Lee, E. Lesne, H. S. J. van Der Zant, P. G. Steeneken, B. A. Ivanov, E. Coronado, and A. D. Caviglia, "Controlling the anisotropy of a van der waals antiferromagnet with light", *Science advances*, vol. 7, no. 23, eabf3096, 2021.

[98] A. A. Melnikov, K. N. Boldyrev, Y. G. Selivanov, V. P. Martovitskii, S. V. Chekalin, and E. A. Ryabov, "Coherent phonons in a Bi_2Se_3 film generated by an intense single-cycle thz pulse", *Physical Review B*, vol. 97, no. 21, p. 214 304, 2018.

[99] M. Rodriguez-Vega, Z.-X. Lin, A. Leonardo, A. Ernst, M. G. Vergniory, and G. A. Fiete, "Light-driven topological and magnetic phase transitions in thin layer antiferromagnets", *The Journal of Physical Chemistry Letters*, vol. 13, no. 18, pp. 4152–4158, 2022.

[100] S. P. Weathersby, G. Brown, M. Centurion, T. F. Chase, R. Coffee, J. Corbett, J. P. Eichner, J. C. Frisch, A. R. Fry, M. Gühr, N. Hartmann, C. Hast, R. Hettel, R. K. Jobe, E. N. Jongewaard, J. R. Lewandowski, R. K. Li, A. M. Lindenberg, I. Makasyuk, J. E. May, D. McCormick, M. N. Nguyen, A. H. Reid, X. Shen, K. Sokolowski-Tinten, T. Vecchione, S. L. Vetter, J. Wu, J. Yang, H. A. Dürr, and X. J. Wang, "Mega-electron-volt ultrafast electron diffraction at slac national accelerator laboratory", *Review of Scientific Instruments*, vol. 86, no. 7, 2015.

[101] G. Kresse and J. Hafner, "Ab initio molecular dynamics for liquid metals", *Physical review B*, vol. 47, no. 1, p. 558, 1993.

[102] G. Kresse and J. Hafner, "Ab initio molecular-dynamics simulation of the liquid-metal–amorphous-semiconductor transition in germanium", *Physical Review B*, vol. 49, no. 20, p. 14 251, 1994.

[103] G. Kresse and J. Furthmüller, "Efficiency of ab-initio total energy calculations for metals and semiconductors using a plane-wave basis set", *Computational materials science*, vol. 6, no. 1, pp. 15–50, 1996.

[104] G. Kresse and D. Joubert, "From ultrasoft pseudopotentials to the projector augmented-wave method", *Physical Review B*, vol. 59, no. 3, p. 1758, 1999.

[105] G. Kresse and J. Furthmüller, "Efficient iterative schemes for ab initio total-energy calculations using a plane-wave basis set", *Physical Review B*, vol. 54, no. 16, p. 11 169, 1996.

[106] J. P. Perdew, K. Burke, and M. Ernzerhof, "Generalized gradient approximation made simple", *Physical Review Letters*, vol. 77, no. 18, p. 3865, 1996.

[107] S. Grimme, J. Antony, S. Ehrlich, and H. Krieg, "A consistent and accurate ab initio parametrization of density functional dispersion correction (dft-d) for the 94 elements h-pu", *The Journal of chemical physics*, vol. 132, no. 15, 2010.

[108] S. Grimme, S. Ehrlich, and L. Goerigk, "Effect of the damping function in dispersion corrected density functional theory", *Journal of computational chemistry*, vol. 32, no. 7, pp. 1456–1465, 2011.

[109] S. L. Dudarev, G. A. Botton, S. Y. Savrasov, C. Humphreys, and A. P. Sutton, "Electron-energy-loss spectra and the structural stability of nickel oxide: An lsda+ u study", *Physical Review B*, vol. 57, no. 3, p. 1505, 1998.

[110] A. Togo and I. Tanaka, "First principles phonon calculations in materials science", *Scripta Materialia*, vol. 108, pp. 1–5, 2015.

[111] K. Momma and F. Izumi, "Vesta 3 for three-dimensional visualization of crystal, volumetric and morphology data", *Journal of applied crystallography*, vol. 44, no. 6, pp. 1272–1276, 2011.

[112] M. Köpf, J. Ebad-Allah, S. Lee, Z. Mao, and C. A. Kuntscher, "Influence of magnetic ordering on the optical response of the antiferromagnetic topological insulator $MnBi_2Te_4$", *Physical Review B*, vol. 102, no. 16, p. 165 139, 2020.

[113] W. Baltensperger and J. S. Helman, "Influence of magnetic order in insulators on optical phonon frequency", *Helvetica physica acta*, vol. 41, no. 6-7, pp. 668–+, 1968.

[114] B. Li, J.-Q. Yan, D. M. Pajerowski, E. Gordon, A.-M. Nedić, Y. Sizyuk, L. Ke, P. P. Orth, D. Vaknin, and R. J. McQueeney, "Competing magnetic in-

teractions in the antiferromagnetic topological insulator $MnBi_2Te_4$", *Physical Review Letters*, vol. 124, no. 16, p. 167 204, 2020.

[115] R. P. Prasankumar and A. J. Taylor, *Optical techniques for solid-state materials characterization*. CRC press, 2016.

[116] T. Konstantinova, J. D. Rameau, A. H. Reid, O. Abdurazakov, L. Wu, R. Li, X. Shen, G. Gu, Y. Huang, L. Rettig, I. Avigo, M. Ligges, J. K. Freericks, A. F. Kemper, H. A. Dürr, U. Bovensiepen, P. D. Johnson, X. Wang, and Y. Zhu, "Nonequilibrium electron and lattice dynamics of strongly correlated $Bi_2Sr_2CaCu_2O_{8+\delta}$ single crystals", *Science Advances*, vol. 4, no. 4, eaap7427, 2018.

[117] M. Gibertini, M. Koperski, A. F. Morpurgo, and K. S. Novoselov, "Magnetic 2d materials and heterostructures", *Nature nanotechnology*, vol. 14, no. 5, pp. 408–419, 2019.

[118] O. Breunig and Y. Ando, "Opportunities in topological insulator devices", *Nature Reviews Physics*, vol. 4, no. 3, pp. 184–193, 2022.

[119] H. Li, C.-Z. Chen, H. Jiang, and X. Xie, "Coexistence of quantum hall and quantum anomalous hall phases in disordered $MnBi_2Te_4$", *Physical Review Letters*, vol. 127, no. 23, p. 236 402, 2021.

[120] X. Jiang, Q. Liu, J. Xing, N. Liu, Y. Guo, Z. Liu, and J. Zhao, "Recent progress on 2d magnets: Fundamental mechanism, structural design and modification", *Applied Physics Reviews*, vol. 8, no. 3, 2021.

[121] Z. Wang, I. Gutiérrez-Lezama, N. Ubrig, M. Kroner, M. Gibertini, T. Taniguchi, K. Watanabe, A. Imamoğlu, E. Giannini, and A. F. Morpurgo, "Very large tunneling magnetoresistance in layered magnetic semiconductor cri3", *Nature communications*, vol. 9, no. 1, p. 2516, 2018.

[122] S. M. Winter, A. A. Tsirlin, M. Daghofer, J. van den Brink, Y. Singh, P. Gegenwart, and R. Valentí, "Models and materials for generalized kitaev magnetism", *Journal of Physics: Condensed Matter*, vol. 29, no. 49, p. 493 002, 2017.

[123] K. S. Novoselov, A. Mishchenko, A. Carvalho, and A. Castro Neto, "2d materials and van der waals heterostructures", *Science*, vol. 353, no. 6298, aac9439, 2016.

[124] Y. Wang, H. Steinberg, P. Jarillo-Herrero, and N. Gedik, "Observation of floquet-bloch states on the surface of a topological insulator", *Science*, vol. 342, no. 6157, pp. 453–457, 2013.

[125] F. Mahmood, C.-K. Chan, Z. Alpichshev, D. Gardner, Y. Lee, P. A. Lee, and N. Gedik, "Selective scattering between floquet–bloch and volkov states in a topological insulator", *Nature Physics*, vol. 12, no. 4, pp. 306–310, 2016.

[126] A. De La Torre, D. M. Kennes, M. Claassen, S. Gerber, J. W. McIver, and M. A. Sentef, "Colloquium: Nonthermal pathways to ultrafast control in quantum materials", *Reviews of Modern Physics*, vol. 93, no. 4, p. 041 002, 2021.

[127] C. Bao, P. Tang, D. Sun, and S. Zhou, "Light-induced emergent phenomena in 2d materials and topological materials", *Nature Reviews Physics*, vol. 4, no. 1, pp. 33–48, 2022.

[128] B. Peng, H. Zhang, W. Chen, B. Hou, Z.-J. Qiu, H. Shao, H. Zhu, B. Monserrat, D. Fu, H. Weng, *et al.*, "Sub-picosecond photo-induced displacive phase transition in two-dimensional mote2", *npj 2D Materials and Applications*, vol. 4, no. 1, p. 14, 2020.

[129] Y. Chen, J.-H. Chu, J. Analytis, Z. Liu, K. Igarashi, H.-H. Kuo, X. Qi, S.-K. Mo, R. Moore, D. Lu, *et al.*, "Massive dirac fermion on the surface of a mag-

netically doped topological insulator", *Science*, vol. 329, no. 5992, pp. 659–662, 2010.

[130] H. Padmanabhan, M. Poore, P. K. Kim, N. Z. Koocher, V. A. Stoica, D. Puggioni, H. Wang, X. Shen, A. H. Reid, M. Gu, M. Wetherington, S. H. Lee, R. D. Schaller, Z. Mao, A. M. Lindenberg, X. Wang, J. M. Rondinelli, R. D. Averitt, and V. Gopalan, "Interlayer magnetophononic coupling in $MnBi_2Te_4$", *Nature Communications*, vol. 13, no. 1, p. 1929, 2022.

[131] T. Zhu, H. Wang, and H. Zhang, "Floquet engineering of magnetic topological insulator $MnBi_2Te_4$ films", *Physical Review B*, vol. 107, no. 8, p. 085 151, 2023.

[132] C. Zhou and J. Zhou, "Light-induced topological phase transition with tunable layer hall effect in axion antiferromagnets", *Nano Letters*, 2024.

[133] D. Lujan, J. Choe, M. Rodriguez-Vega, Z. Ye, A. Leonardo, T. N. Nunley, L.-J. Chang, S.-F. Lee, J. Yan, G. A. Fiete, R. He, and X. Li, "Magnons and magnetic fluctuations in atomically thin $MnBi_2Te_4$", *Nature Communications*, vol. 13, no. 1, p. 2527, 2022.

[134] H. Padmanabhan, V. A. Stoica, P. K. Kim, M. Poore, T. Yang, X. Shen, A. H. Reid, M.-F. Lin, S. Park, J. Yang, H. Wang, N. Z. Koocher, D. Puggioni, A. B. Gerogescu, L. Min, S. H. Lee, Z. Mao, J. M. Rondinelli, A. M. Lindenberg, L.-Q. Chen, X. Wang, R. D. Averitt, J. W. Freeland, and V. Gopalan, "Large exchange coupling between localized spins and topological bands in $MnBi_2Te_4$", *Advanced Materials*, vol. 34, no. 49, p. 2 202 841, 2022.

[135] F. M. Bartram, Y.-C. Leng, Y. Wang, L. Liu, X. Chen, H. Peng, H. Li, P. Yu, Y. Wu, M.-L. Lin, J. Zhang, P.-H. Tan, and L. Yang, "Ultrafast coherent interlayer phonon dynamics in atomically thin layers of $MnBi_2Te_4$", *npj Quantum Materials*, vol. 7, no. 1, p. 84, 2022.

[136] S. Mukherjee, A. K. NM, S. Manna, S. G. Nath, R. K. Gopal, C. Mitra, and N. Kamaraju, "Investigation of magnetic order influenced phonon and electron dynamics in $MnBi_2Te_4$ and Sb doped $MnBi_2Te_4$ through terahertz time-domain spectroscopy", *arXiv preprint arXiv:2403.11580*, 2024.

[137] A. Alfonsov, K. Mehlawat, A. Zeugner, A. Isaeva, B. Büchner, and V. Kataev, "Magnetic-field tuning of the spin dynamics in the magnetic topological insulators $(MnBi_2Te_4)(Bi_2Te_3)_n$", *Phys. Rev. B*, vol. 104, p. 195 139, 19 Nov. 2021.

[138] Y. J. Bae, J. Wang, A. Scheie, J. Xu, D. G. Chica, G. M. Diederich, J. Cenker, M. E. Ziebel, Y. Bai, H. Ren, and et al., "Exciton-coupled coherent magnons in a 2d semiconductor", *Nature*, vol. 609, no. 7926, pp. 282–286, Sep. 2022.

[139] X.-X. Zhang, L. Li, D. Weber, J. Goldberger, K. F. Mak, and J. Shan, "Gate-tunable spin waves in antiferromagnetic atomic bilayers", *Nature Materials*, vol. 19, no. 8, pp. 838–842, Jun. 2020.

[140] X. Xu, S. Yang, H. Wang, R. Guzman, Y. Gao, Y. Zhu, Y. Peng, Z. Zang, M. Xi, S. Tian, and et al., "Ferromagnetic-antiferromagnetic coexisting ground state and exchange bias effects in $MnBi_4Te_7$ and $MnBi_6Te_{10}$", *Nature Communications*, vol. 13, no. 1, Dec. 2022.

[141] M. Garnica, M. M. Otrokov, P. C. Aguilar, I. I. Klimovskikh, D. Estyunin, Z. S. Aliev, I. R. Amiraslanov, N. A. Abdullayev, V. N. Zverev, M. B. Babanly, and et al., "Native point defects and their implications for the dirac point gap at $MnBi_2Te_4(0001)$", *npj Quantum Materials*, vol. 7, no. 1, Jan. 2022.

[142] Y. Li, Z. Jiang, J. Li, S. Xu, and W. Duan, "Magnetic anisotropy of the two-dimensional ferromagnetic insulator $MnBi_2Te_4$", *Physical Review B*, vol. 100, no. 13, p. 134 438, 2019.